ISSN 0915-6364

NATIONAL INSTITUTE FOR FUSION SCIENCE

Population Alignment Collisional Radiative Model for Helium-like Carbon: Polarization of Emission Lines and Anisotropy of the Electron Velocity Distribution Function in Plasmas

A. Iwamae, T. Fujimoto, H. Zhang, D. P. Kilcrease,
G. Csanak and K.A. Berrington

(Received - Aug. 11, 2003)

NIFS-DATA-78 Aug. 2003

TOKI, JAPAN

Population Alignment Collisional Radiative Model for Helium-like Carbon: Polarization of Emission Lines and Anisotropy of the Electron Velocity Distribution Function in Plasmas

Atsushi Iwamae* and Takashi Fujimoto

Department of Engineering Physics and Mechanics,

Graduate School of Engineering, Kyoto University, Kyoto 606-8501, Japan

Honglin Zhang, David P. Kilcrease, and George Csanak

Los Alamos National Laboratory, Los Alamos, NM 87545

Keith A. Berrington

School of Science and Mathematics,

Sheffield Hallam University, Sheffield S1 1WB, UK

Dedicated to the memory of Professor Douglas H. Sampson.

(Dated: August 12, 2003)

Abstract

The polarization of emission lines from a plasma carries information about the anisotropic velocity distribution of electrons in the plasma, and thus polarization spectroscopy can give information that is inaccessible by other methods. We have developed a comprehensive population-alignment collisional-radiative (PACR) model code for helium-like carbon CV ions. This code is intended to correlate quantitatively the observed polarization of emission lines from the ions in a plasma with the anisotropy of the electron velocity distribution function. Specifically, the longitudinal alignment of CV triplet emission lines for the ($1s2s\,^3S_1 - 1s2p\,^3P_{1,2}$) transitions are studied by this PACR model. The predominant process which produces alignment in the $1s2p\,^3P_{1,2}$ levels is the alignment production from the ground state, $1s^2\,^1S_1$ and from the metastable level, $1s2s\,^3S_1$. The alignment-production fluxes from these levels are in the opposite directions in the temperature range of practical interest, depending on the electron density n_e. When $n_e > 10^{16}\,m^{-3}$, the alignment-production flux from the metastable level is larger than that from the ground state. An anisotropic electron velocity distribution function that has higher values in the axial (toroidal) direction than in the radial (poloidal) direction produces negative longitudinal alignment of the emission lines, i.e., higher intensity of the linear polarized component in the radial direction than that in the axial direction.

PACS numbers: 52.25.Tx, 52.70.Kz, 32.70.-n

Keywords: CV ion, line emission, polarization, longitudinal alignment, anisotropic electron velocity distribution, population alignment collisional radiative model

*Electronic address: iwamae@kues.kyoto-u.ac.jp

I. INTRODUCTION

In plasma spectroscopy a thermal or Maxwellian distribution is implicitly assumed for electron velocities, and we use the concept of electron temperature T_e to quantify the physical state of the electrons. In actual plasmas, however, the electron distribution function may deviate from the Maxwell distribution. It can even be anisotropic.

Collisional excitations by electrons having an anisotropic velocity distribution produce alignments in ions (by "ions" we include atoms, too) in excited levels. The emission lines from such aligned levels are polarized. For example, the observed polarization of the emission line in the sheath region of a high-frequency rf discharge is due to the fast electrons accelerated by the electric field[1]. Thus, the polarization of emission lines has a possibility of providing information about the anisotropic characteristics of a plasma, which are inaccessible by any other method. It has been reported that emission lines can be polarized in laboratory plasmas such as the positive column of dc discharges[2], high-frequency rf discharges[1], laser produced plasmas[3–6] and magnetically confined plasmas [7]. This is the reason why the polarization of emission lines from ions in plasmas has created much attention recently.

For magnetically confined plasmas like those of tokamaks, the electrons are confined by a magnetic field, and the various wave-heatings, such as the electron cyclotron resonance heating (ECRH) and the lower-hybrid current drive (LHCD), act upon a part of the electron velocity distribution function (EVDF). In these circumstances, the EVDF can be perturbed strongly and can be anisotropic. Actually, in the Alcator device, the non-thermal spectrum of Thomson scattering is interpreted as due to a velocity distribution which has an electron beam component superimposed upon the thermal bulk-electron component [8, 9]. In the WT-3 plasma the anisotropic distribution function of fast electrons is estimated from hard X-ray spectrum measurements [10]. The electron energy distribution function (EEDF) is measured in low pressure rf discharges and in transformer coupled discharges by means of Langmuir probes [11–14]. It is shown that the EEDFs can be divided into two parts, into a cold "bulk" part and into a much hotter and less dense "tail" part. This feature of the EEDF is understood to result from stochastic electron heating on the oscillating plasma-sheath boundary. The emission from such an rf plasma may be polarized.

The anisotropic EVDF and the polarization of emission lines from ions in plasma can be

correlated quantitatively. We consider an ensemble of ions. We assume that level p, excited or the ground state, has the total angular momentum J. Let the magnetic sublevel of this level be specified by M, the magnetic quantum number. The ensemble of ions in level p is characterized by a density matrix ρ with the matrix elements $< JM'|\rho|JM >$. The density operator in the $|JM >$ representation is written in the form,

$$\rho(p) = \sum_{M'M} < JM'|\rho|JM > |JM' >< JM|. \tag{1}$$

An alternative equivalent description is in terms of state multipoles. The density operator is expanded in terms of the irreducible tensor operators:

$$\rho(p) = \sum_{JKQ} < T(J)^{\dagger}_{KQ} > T(J)_{KQ}, \tag{2}$$

where $< T(J)^{\dagger}_{KQ} >$ is the state multipole or the statistical tensor [15, 16] and is defined as,

$$< T(J)^{\dagger}_{KQ} > = \sum_{M'M} (-1)^{J-M'} (2K+1)^{1/2} \begin{Bmatrix} J & J & K \\ M' & -M & -Q \end{Bmatrix} < JM'|\rho|JM >, \tag{3}$$

where $\{\}$ is the 6-j symbol. If an axially symmetric system is assumed, all components with $Q \neq 0$ vanish. Equation (2) then reduces to,

$$\rho(p) = \sum_{JK} < T(J)^{\dagger}_{K0} > T(J)_{K0}. \tag{4}$$

This is the case for magnetically confined plasmas, since the electron cyclotron motion around the magnetic fields smoothes out any non-axial asymmetry created in the ensemble of ions. We write

$$a(p) =< T(J)^{\dagger}_{20} > \tag{5}$$

to denote alignment and we adopt

$$n(p) = \sqrt{2J_p + 1} < T(J)^{\dagger}_{00} > \tag{6}$$

for population in accordance with the conventional definition.

An electric-dipole transition without a change in the magnetic quantum numbers $\Delta m_J = m_{J_{\text{upper}}} - m_{J_{\text{lower}}} = 0$ gives rise to emission of the light polarized parallel to the quantization axis, or the z-axis; this is called the π light; transitions with $\Delta m_J = +1$ and -1, produce σ^+ and σ^- light, respectively. The angular distribution of the intensity of the polarized

component is proportional to $\sin^2\theta$ for the π light and to $\left(1-\frac{1}{2}\sin^2\theta\right)$ for the σ^+ and σ^- light, where θ is the polar angle between the field direction and the viewing direction. When the magnetic field B points towards the observer (longitudinal) , one observes only the two σ components, and the π component is not observed. In such a case σ^+ is the "violet" σ-component and left-circularly polarized ,and σ^- is the "red" σ-component and right circularly polarized[17, 18]. If we observe the radiation from the direction perpendicular to the z-axis, i.e. $\theta = 90°$, I_π is the intensity of the π light and $I_\sigma = \frac{1}{2}I_{\sigma+} + \frac{1}{2}I_{\sigma-}$ is the intensity of the σ light, which is polarized perpendicularly to the z-axis. The "true" intensity or the photon number of the emission line $I_0 = (2/3)(I_\pi + 2I_\sigma)$ from an upper level p to lower level s is proportional to the upper level population $n(p)$,

$$I_0 = \frac{1}{4\pi l^2} n(p) A(p,s), \tag{7}$$

where l is the distance from the emitting ions to the detector and $A(p,s)$ is the Einstein A coefficient. Instead of the polarization degree $P = (I_\pi - I_\sigma)/(I_\pi + I_\sigma)$, we employ the longitudinal alignment

$$A_{\mathrm{L}} = \frac{I_\pi - I_\sigma}{I_\pi + 2I_\sigma} = \frac{2P}{3-P}. \tag{8}$$

This quantity is directly proportional to the ratio of the alignment $a(p)$ to the population $n(p)$, as given by

$$A_{\mathrm{L}}(p,s) = (-1)^{J_p+J_s}\sqrt{\frac{3}{2}}(2J_p+1)\begin{Bmatrix} J_p & J_p & 2 \\ 1 & 1 & J_s \end{Bmatrix}\frac{a(p)}{n(p)}. \tag{9}$$

The spatially anisotropic collisional excitation by electrons having an anisotropic velocity distribution can create alignment. This fact means that, in addition to the intensity of a line, we can use its polarization as another source of information for the purpose of interpreting the characteristics of the plasma. The theoretical framework of the kinetic model, which relates the observed polarization to the anisotropic velocity distribution is called the population-alignment collisional-radiative (PACR) model and is described in ref. [19]. The implementation of the PACR model for beryllium-like oxygen (OV) is reported in ref. [20]. Within this framework, in the present study, we have constructed a code based on the PACR model for helium-like carbon (CV) for the purpose of interpreting the experimental observations [7] in terms of the anisotropic electron velocity distribution in the plasma.

For helium-like carbon ions the triplet lines (C V: 1s2s $^3S_1$–1s2p $^3P_{0,1,2}$) are often employed in plasma diagnostics since these lines have relatively high intensities and are situated

in the ultraviolet-visible region, convenient for observation. It was reported that the intensity ratio between the π and σ components of $J = 1 - 2$ transition changed during the discharge time [7]. This means that the ensemble in the upper levels of the exited ions was aligned and the anisotropy of the electron velocity distribution changed with time.

II. CROSS SECTIONS AND RATE COEFFICIENTS

The seventeen levels belonging to the $1s^2$,1s2s,1s2p,1s3s,1s3p and 1s3d configurations of CV are included in the present PACR model. Figure 1 shows the relevant part of the energy level diagram. The numbers from *1* to *17* are used to specify these levels. The level-assignments are tabulated in Table I.

For excitation and de-excitation between the levels $\alpha J \leftarrow \alpha' J'$ or $r \rightarrow p$, where α stands for the relevant quantum numbers for the level, the basic cross section data are the cross sections $Q_{\alpha JM,\alpha' J'M'}$ from a magnetic sublevel $\alpha' J'M'$ to a magnetic sublevel αJM. The cross sections $Q_{\alpha JM,\alpha' J'M'}$ are calculated in the relativistic distorted wave (RDW) approximation [21–24]. The cross section data were calculated from threshold to 3000 eV collision energy.

The R-matrix method [25–29] has also been used to produce cross section data from the ground state *1*, $1s^2\,{}^1S_0$, to levels *4*, *5*, *6*, $1s2p\,{}^3P_{0,1,2}$ states, and from level *2*, 1s2s $^3S_1$, to levels *4*, *5*, *6*, $1s2p\,{}^3P_{0,1,2}$ states. The R-matrix calculation included the lowest 17 levels of the He-like ion, corresponding to the eleven $n \leq 3$ terms, exactly the same levels treated in this PACR model. The orbitals of the He-like ion target were represented by Slater-type radial orbitals: the 1s from Clementi and Roetti [30] and the 2s,2p,3s,3p,3d orbitals by minimizing the respective target state energies using the CIV3 program [31]. The Breit-Pauli R-matrix program [27] was used with thirty continuum terms per channel, to obtain fine-structure collision strengths and T-matrices, the latter being used as input to obtain scattering amplitudes for the magnetic quantum numbers [28]. Since the R-matrix target ion basis included only physical orbitals, the resonances as calculated represent real structure in the scattering cross section.

The cross sections employed in the PACR model are those involving the population and the alignment, denoted by $Q_q^{kk'}(r,p)$[19]. For excitation or deexcitation of $\alpha J \leftarrow \alpha' J' (\alpha J \neq$

$\alpha' J'$) or $r \to p (r \neq p)$ these cross sections are defined by the formulas[19],

$$Q_0^{00}(r,p) = (2J'+1)^{-1} \sum_{MM'} Q_{\alpha JM,\alpha' J'M'} \tag{10}$$

$$Q_0^{20}(r,p) = (2J'+1)^{-1} \sum_{MM'} (-1)^{J-M} < JJM - M|20 > Q_{\alpha JM,\alpha' J'M'} \tag{11}$$

$$Q_0^{02}(r,p) = \sum_{M'} (-1)^{J'-M'} < J'J'M' - M'|20 > \sum_{M} Q_{\alpha JM,\alpha' J'M'} \tag{12}$$

$$Q_0^{22}(r,p) = \sum_{MM'} (-1)^{J+J'+M+M'} < JJM - M|20 >< J'J'M' - M'|20 > Q_{\alpha JM,\alpha' J'M} \tag{13}$$

where $< JJM - M|kq >$ is the Clebsch-Gordan coefficient. For the cross sections where both k and k' are equal to 2, q can be 0, 1 and 2. For $q = 1$ and $q = 2$ we have,

$$Q_q^{22}(r,p) = \sum_{MM'} (-1)^{J+J'+M+M'} < JJM(q-M)|2q >< J'J'M'(q-M')|2q > \times 2\pi \int < \alpha JM|S_c|\alpha' J'M' >< \alpha J(M-q)|S_c|\alpha' J'(M'-q) >^* b\,\mathrm{d}b. \tag{14}$$

Here S_c is the collision matrix referred to the collision axis, and b is the collision parameter. The coherence transfer cross sections, Q_1^{22} and Q_2^{22}, cannot be expressed in terms of the magnetic-sublevel-to-magnetic-sublevel cross sections, $Q_{\alpha JM,\alpha' J'M'}$. In the present model we neglected these coherence transfer cross sections.

The cross section $Q_0^{00}(r,p)$ in Eq. (10) is the cross section from level r to level p; this is nothing but the conventional excitation or deexcitation cross section. $Q_0^{20}(r,p)$ is the alignment production cross section of level p from the population of level r, and $Q_0^{22}(r,p)$ is the alignment transfer cross section.

The cross sections used in the model are plotted in Figs. 2−52. The cross sections represented in Figs. 2−45 are calculated by means of the RDW method. The cross sections related to alignment Q_0^{20}, Q_0^{02} and Q_0^{22} may take negative values. The excitation and de-excitation cross sections Q_0^{00} are related by the principle of detailed balance given by the Klein-Rosseland relationship. The cross section for de-excitation $p \to r$ is given as

$$Q_0^{00}(p,r;E'') = \frac{(2J_r+1)}{(2J_p+1)} \frac{E'}{E''} Q_0^{00}(r,p;E') \tag{15}$$

where the incoming electron energy E'' in de-excitation is equal to $E' - \Delta E$, i.e. to the incoming electron energy for excitation minus the threshold energy. If we assume a rectilinear path for the perturbers (i.e. for the scattering electrons), the principle of detailed balance

holds for each pair of the magnetic-sublevel-to-magnetic-sublevel cross sections $Q_{\alpha JM,\alpha' J'M'}$ and $Q_{\alpha' J'M',\alpha JM}$, and $Q_0^{20}(r,p)$ is related to $Q_0^{02}(r,p)$. However since we use RDW and R matrix cross sections, it is not the case for electron collisions. The de-excitation cross sections $Q_{\alpha' J'M',\alpha JM}$ are also independently obtained and shown in Figs. 24−45 .

In Figs. 46−51 the excitation cross sections Q_0^{00} and the alignment production cross sections Q_0^{20} calculated by the R-matrix method are plotted. The resonance structures can be clearly seen. The cross sections obtained by the RDW method are reproduced for comparison. In Figs. 49−51, the alignment production cross sections Q_0^{20} calculated by the R-matrix method change sign at 16 eV, while the Q_0^{20} cross sections calculated by the RDW method change sign at around 70 eV.

In order to include the cross section data into the PACR model, both the RDW and R-matrix cross sections were interpolated with cubic spline curves. Many resonances which are prominent in the R-matrix cross sections were included as they are. R-matrix cross section data were smoothly extrapolated with the shifted RDW cross sections over the electron collision energy above 400 eV for level *1* to levels *4*, *5*, *6*, $1^1S_0 - 2^3P_{0,1,2}$ transitions, and above 100 eV for level *2* to levels *4*, *5*, *6*, $2^3S_1 - 2^3P_{0,1,2}$ transitions. Figure 52 shows an example of comparisons of the extrapolated R-matrix cross sections with the RDW cross sections, Q_0^{00} and Q_0^{20}, for *1-6* and *2-6* transitions.

The EVDF is expressed as $f(v,\theta)$, which satisfies the normalization condition, $\iint f(v,\theta)v^2 \sin\theta \, dv \, d\theta = 1$. Note that axial symmetry is assumed around the z-axis, the quantization axis. We take the quantization axis in the magnetic field direction.

The EVDF is expanded in terms of Legendre polynomials,

$$f(v,\theta) = \sum_K f_K(v) P_K(\cos\theta) \tag{16}$$

with

$$f_K(v) = \frac{(2K+1)}{2} \int f(v,\theta) P_K(\cos\theta) \sin\theta \, d\theta. \tag{17}$$

Only K= (even) terms are considered, since we cannot distinguish between $\cos\theta$ and $\cos(-\theta)$ components in the actual observation.

Three anisotropic EVDF models are considered in the present PACR model. In the first model a part of the electrons is described by the isotropic Maxwell velocity distribution, and another part has a shifted Maxwell distribution centered at a high velocity V_z along the quantization z axis. We call this model the thermal-bulk-with-beam type. This is an

example of the anisotropic EVDF in which a beam component is superimposed on the bulk electrons having an isotropic distribution [8, 9]. These two parts are called the thermal, $f_{\rm th}(v,\theta)$, and beam, $f_{\rm b}T(v,\theta)$, components, respectively,

$$f(v,\theta) = f_{\rm th}(v,\theta) + f_{\rm b}(v,\theta) \tag{18a}$$

$$f_{\rm th}(v,\theta) = 2\pi\frac{1}{1+\delta}\left(\frac{m}{2\pi k_{\rm B}T_{\rm eth}}\right)^{3/2}\exp\left(-\frac{m}{2k_{\rm B}T_{\rm eth}}v^2\right) \tag{18b}$$

$$f_{\rm b}(v,\theta) = 2\pi\frac{\delta}{1+\delta}\left(\frac{m}{2\pi k_{\rm B}T_{\rm eb}}\right)^{3/2}\exp\left\{-\frac{m}{2k_{\rm B}T_{\rm eb}}\left(v^2 - 2vV_z\cos\theta + V_z^2\right)\right\}, \tag{18c}$$

where m is the electron mass, $k_{\rm B}$ is the Boltzmann constant, δ is the ratio of the electron number densities between the beam and thermal-bulk components. This EVDF corresponds to a model with some run-away electrons in the plasma [9]. The Legendre expansion coefficients of the bulk-with-beam type EVDF, f_0v^3 and f_2v^3, are plotted in Fig. 52 for various δ values with the parameters $T_{\rm eth} = T_{\rm eb}$= 250 eV and $V_z = 1.87\times10^7$ m/s.

The second model-distribution is similar to the first one in that it has high velocity component, but in this case, the direction of displacement is perpendicular to the quantization axis. The total electron distribution $f(v,\theta)$ is described as the sum of a thermal-bulk component having an ordinary Maxwell distribution, $f_{\rm th}(v,\theta)$, and a ring shaped high velocity component; this distribution is called the "Saturn type". The ring distribution $f_{\rm r}(v,\theta)$ is displaced by $V_{\rm r}$;

$$f_{\rm r}(v,\theta) = 2\pi\frac{\delta}{1+\delta}A_{\rm r}\exp\left\{-\frac{m}{2k_{\rm B}T_{\rm er}}\left(v^2 - 2vV_{\rm r}\sin\theta + V_{\rm r}^2\right)\right\}, \tag{19}$$

where $A_{\rm r}$ is the normalization factor;

$$\frac{1}{A_{\rm r}} = \left(\frac{2\pi k_{\rm B}T_{\rm er}}{m}\right)^{3/2}\exp\left(-\frac{mV_{\rm r}^2}{2k_{\rm B}T_{\rm er}}\right) + \left(\frac{2\pi k_{\rm B}T_{\rm er}}{m}\right)\pi V_{\rm r}\left\{1+{\rm Erf}\left(\sqrt{\frac{m}{2k_{\rm B}T_{\rm er}}}V_{\rm r}\right)\right\} \tag{20}$$

obtained by the integration; $\iint f_r(v,\theta)v^2\sin\theta{\rm d}v\,{\rm d}\theta = \delta/(1+\delta)$.

The third model-function is described by two temperatures which are different in the axial and radial directions as in a tokamak plasma, for example. We call these temperatures the toroidal and poloidal temperatures, $T_{\rm t}$ and $T_{\rm p}$, respectively.

$$f(v,\theta) = 2\pi\left(\frac{m}{2\pi k_{\rm B}}\right)^{3/2}\left(\frac{1}{T_{\rm p}^2T_{\rm t}}\right)^{1/2}\exp\left(-\frac{mV_z}{2k_BT_{\rm t}}\right)\times \tag{21}$$
$$\exp\left\{-\frac{m}{2k_{\rm B}}v^2\left(\frac{\sin^2\theta}{T_{\rm p}}+\frac{\cos^2\theta}{T_{\rm t}}\right)-\frac{2vV_z\cos\theta}{T_{\rm t}}\right\}.$$

When a plasma is produced by ECRH in a magnetic field, the electron temperature and the electron density may reach several keV to hundred keV and 10^{16} and $10^{17}\,\mathrm{m}^{-3}$, respectively. In such a hot electron plasma, the anisotropy of EVDFs ($T_\mathrm{p} > T_\mathrm{t}$) may induce not only electrostatic instability, the Harris instability [32], but also the electromagnetic instability, and whistler instability[33–35].

The excitation rate coefficients for a transition $\alpha J \leftarrow \alpha' J'$, or $r \rightarrow p$ are defined in the PACR model [19] as,

$$C^{00}(r,p) = \int Q_0^{00}(r,p) 2 f_0(v) v^3 \,\mathrm{d}v, \tag{22a}$$

$$C^{20}(r,p) = \int Q_0^{20}(r,p) \frac{2}{5} f_2(v) v^3 \,\mathrm{d}v, \tag{22b}$$

$$C^{02}(r,p) = \int Q_0^{02}(r,p) \frac{2}{5} f_2(v) v^3 \,\mathrm{d}v, \tag{22c}$$

$$\begin{aligned} C^{22}(r,p) = & \int [Q_0^{22}(r,p) + Q_1^{22}(r,p) + Q_2^{22}(r,p)] \frac{2}{5} f_0(v) v^3 \,\mathrm{d}v \\ & + \int [2Q_0^{22}(r,p) + Q_1^{22}(r,p) - 2Q_2^{22}(r,p)] \frac{2}{35} f_2(v) v^3 \,\mathrm{d}v \\ & + \int [6Q_0^{22}(r,p) - 4Q_1^{22}(r,p) + Q_2^{22}(r,p)] \frac{2}{105} f_4(v) v^3 \,\mathrm{d}v. \end{aligned} \tag{22d}$$

We calculated these rate coefficients from the cross sections given, in Figs. 2– 52, and from the express for $f_0(v)$, $f_2(v)$ and $f_4(v)$ for the various EVDFs. As mentioned already, we ignored the coherence transfer cross section $Q_q^{22}(q = 1 \text{ and } 2)$. The ionization rate coefficients $S(p)$ were calculated from the cross sections obtained by Professor Sampson's group [36–39].

III. PACR MODEL

We assume an ionizing plasma. The temporal development of the population $n(p)$ and the alignment $a(p)$ of level p is described by the PACR model rate equations [19]. We have two sets of rate equations for the ensemble of ions. For the population we have a rate equation,

$$\begin{aligned} \frac{\mathrm{d}n(p)}{\mathrm{d}t} = & \sum_{r \neq p} \left[C^{00}(r,p) n_\mathrm{e} + A^{00}(r,p) \right] n(r) \\ & - \left[\left\{ \sum_{r \neq p} C^{00}(r,p) + S(p) \right\} n_\mathrm{e} + \sum_{r \neq p} A^{00}(p,r) \right] n(p) \\ & + \sum_{r \neq p} C^{02}(r,p) n_\mathrm{e} a(r) \\ & - C^{02}(p,p) n_\mathrm{e} a(p), \end{aligned} \tag{23}$$

and for the alignment we have,

$$\begin{aligned}\frac{\mathrm{d}a(p)}{\mathrm{d}t} &= \sum_{r\neq p} C^{20}(r,p)n_{\mathrm{e}}n(r) \\ &\quad -C^{20}(p,p)n_{\mathrm{e}}n(p) \\ &\quad +\sum_{r\neq p}\left[C^{02}(r,p)n_{\mathrm{e}}+A^{22}(r,p)\right]a(r) \\ &\quad -\left[C^{22}(p,p)n_{\mathrm{e}}+\sum_{r\neq p}A^{00}(p,r)\right]a(p),\end{aligned} \tag{24}$$

where n_{e} is the electron density. Spontaneous radiative transition processes are isotropic, and the two corresponding rates are given for $r \to p$ $(p \neq r)$ by,

$$A^{00}(r,p) = A(r,p) \tag{25}$$

$$A^{22}(r,p) = (-1)^{J_p+J_r+1}(2J_r+1)\begin{Bmatrix} J_r & J_r & 2 \\ J_p & J_p & 1 \end{Bmatrix} A(r,p), \tag{26}$$

where $A(r,p)$ is the usual Einstein A coefficient. $C^{kk}(r,p)$ and $S(p)$ are the rate coefficients for electron impact transitions (excitation and deexcitation) and for ionization, respectively. $C^{20}(p,p)$ is the alignment production rate coefficient described by the sum of the rate coefficients for the unequal depopulation from different magnetic sublevels and alignment production by elastic collisions. $C^{02}(p,p)$ is the rate coefficient for disappearance of alignment by depopulation from magnetic sublevels. $C^{22}(p,p)$ is the rate coefficient for alignment destruction. The alignment destruction process has two components: inelastic and elastic collisions, the former is by depopulation, the latter process may be called disalignment[19]. It is reported that the alignment production cross section by elastic scattering for beryllium-like oxygen, OV, $2s2p^3P_1$ level of a 29.81 eV incident electron is two orders of magnitude larger than the largest cross section values obtained for the same ion for inelastic processes[40]. The alignment creation by elastic scattering may therefore be of significant importance. At the moment, we set $C^{20}(p,p) = 0$, $C^{02}(p,p) = 0$ and $C^{22}(p,p) = \sum_{r\neq p} C^{00}(p,r) + S(p)$. This corresponds to the assumption that the cross sections for the depopulation rate from the magnetic sublevels αJM are all equal.

IV. RESULTS AND DISCUSSIONS

We have assumed that the plasma is an *ionizing plasma*, and that the steady state approximation is valid so that $\mathrm{d}/\mathrm{d}t = 0$ in Eqs.(23) and (24). The population $n(p)$ and the alignment $a(p)$ for seventeen levels of CV are determined by solving simultaneously Eqs. (23) and (24). An optically thin plasma is assumed.

First we compare results from our PACR code by assuming an isotropic EVDF with results from the CR model for helium-like ions [41]. In Fig. 53 some of the excitation rate coefficients C^{00} are plotted against electron temperature for the RDW cross sections and for the R-matrix method and extrapolated cross sections. Figure 54 shows the n_e dependencies of the population of several excited levels under the condition $T_\mathrm{e} = 250$ eV and $n(1^1\mathrm{S}) = 1\ \mathrm{m}^{-3}$ using the RDW cross sections. The population of the metastable state *2*, $2^3\mathrm{S}_1$, $n(2)$, increases with the increase in electron density below $n_e \simeq 10^{16}\ \mathrm{m}^{-3}$, then $n(2)$ reaches a plateau for $n_e \geq 10^{16}\ \mathrm{m}^{-3}$. This $n(2)$ dependence on the electron densities affects the alignment, $a(4), a(5)$ and $a(6)$ and also longitudinal alignment A_L of the emissions from these levels as we will see below. When the RDW cross sections are replaced with the R-matrix cross sections for the transitions *1-4,5,6* and *2-4,5,6* and RDW cross sections are used for the rest of the transition, the populations $n(4)$, $n(5)$, $n(6)$ follow a similar electron density dependence with 10-12% reductions from the RDW results. Figure 55 shows the intensity ratio $R/(R+I)$ for CV, where R stands for the resonance-line (*1-7*; $1^1\mathrm{S} - 2^1\mathrm{P}$) intensity and I is the intercombination-line (*1-4,5,6*; $1^1\mathrm{S} - 2^3\mathrm{P}$) intensity. The solid lines show the results for electron temperatures of $T_\mathrm{e} = 100$, 200 and 300 eV. Figure 56 shows the population ratio of the fine structure components of the levels $2^3\mathrm{P}_{1,2}$. The $J = 1$ level has an appreciable transition probability $A = 2.89 \times 10^7\ \mathrm{s}^{-1}$ to $1^1\mathrm{S}_0$ [42], and, at low densities, its population per unit statistical weight is lower than for the other two levels. An increase in the collisional depopulation process, predominantly de-excitation to $2^3\mathrm{S}_1$, makes this population imbalance decrease. With the increase of the electron density from $10^{20}\ \mathrm{m}^{-3}$, the population ratio of $2^3\mathrm{P}_1/2^3\mathrm{P}_2$ gradually increases from around 0.4 to 0.6 (= 3/5), which is the ratio of the statistical weights. These results from the present PACR code with an isotropic thermal distribution is found to agree with those from the conventional CR-model code[41].

When the EVDF is anisotropic, the model functions given by Eq.(18), Eq.(19) or Eq.(21)

are assumed to represent the anisotropic EVDF. The first example of the velocity distribution shown in Fig. 57 is the thermal-bulk-with-beam Maxwellian represented by Eq.(18) with the parameters $\delta = 0.3$, $T_{\rm eth} = T_{\rm eb}$= 250 eV and $V_z = 1.87 \times 10^7$ m/s (1000 eV). This velocity distribution over the polar angle is expanded in terms of Legendre polynomials according to Eq.(17). In our rate equations we use the expansion coefficient multiplied by v^3 as seen in Eq.(22). Figure 58 shows the even moments of the expansion coefficients multiplied by v^3, $f_K(v)v^3$.

The electron energy distribution function (EEDF), $F(\mathcal{E})$ and the electron energy probability function (EEPF) $F_{\rm P}(\mathcal{E})$ are derived from our EVDF, $f(v,\theta)$, by integrating over the polar angle. If we define the function $g(v) = v^2 \int_0^\pi f(v,\theta)\sin\theta\,{\rm d}\theta$ then we have,

$$F(\mathcal{E}){\rm d}\mathcal{E} = \mathcal{E}^{1/2}F_{\rm P}(\mathcal{E}){\rm d}\mathcal{E} = g(v;\mathcal{E})/\sqrt{2m\mathcal{E}}{\rm d}\mathcal{E} \tag{27}$$

where $\mathcal{E}$ is the electron energy. Note that $\int_0^\infty \mathcal{E}^{1/2}F_{\rm P}(\mathcal{E}){\rm d}\mathcal{E} = 1$. The $F_{\rm P}(\mathcal{E})$ corresponds to the second derivative $({\rm d}^2I_{\rm p}/{\rm d}V^2)$ of the probe current $I_{\rm p}$ vs. voltage V characteristic of the Druyvestein formula. When the distribution is Maxwellian, the semilog plot of the second derivative of the probe current vs voltage shows a liner dependence on the electron energy $\mathcal{E}$. It was reported that when a single side plane probe was used for the inductive, or transformer coupled plasma and the plasma was sustained by the E-field generated by a coil placed above the discharge region, then there were significant currents flowing in the plasma and the single faced probe displayed the anisotropic nature of the EVDF [14].

In Fig. 59, the EEPFs derived from the Eq.(18) are plotted with $\delta = 0.001$, 0.01. 0.1, 0.3, 1 and 10 and $T_{\rm eth} = T_{\rm eb} = 250$ eV, $V_z = 1.87 \times 10^7$ m/s. It is seen that the beam component produces the apparent suprathermal electron tail in the EEPF, and with the increase in δ, the relative magnitude of this tail increases.

The degree of anisotropy, α_K may be defined as

$$\alpha_K = \frac{2}{2K+1}\int v^2 f_K(v)\,{\rm d}v. \tag{28}$$

Note that α_0 is constant, (as a function of δ) $\alpha_0 = 1$, and that $-1/2 \le \alpha_2 \le 1$. The positive α_2 corresponds to an EVDF in which the velocity component parallel to the quantization axis, the toroidal component, is dominant, as shown in Fig. 60

Another example of the EVDF, the Saturn-type, represented by Eq.(19), is shown in Fig. 61 and its expansion coefficients in Fig.62. The parameters used for the plots are $\delta = 2$,

$T_{\rm eth} = T_{\rm er} = 250$ eV and $V_r = 1.87 \times 10^7$ m/s. The Saturn type EEDF's shown in Fig. 63 are similar to that of the bulk-with-beam type; Fig. 59. The degree of anisotropy for the Saturn-type EVDF is shown in Fig. 64. The negative α_2 corresponds to an EVDF in which the velocity component is perpendicular to the quantization axis and the poloidal component is predominant.

The two temperature-distribution represented by Eq.(21) is displayed in Fig. 65 where T_t and T_p are 200 and 350 eV, respectively. Its Legendre expansion terms, $f_K(v)v^3$, are plotted in Fig. 66. $f_2(v)$ is negative in this example where the perpendicular-component is predominant, i.e., $T_{\rm t} < T_{\rm p}$. $f_2(v)$ would be positive when the velocity component parallel to the z-axis is predominant, i.e., $T_{\rm t} > T_{\rm p}$. The EEPF curves, $F_{\rm P}(\mathcal{E})$, are plotted in Fig. 67 for various pairs of $T_{\rm t}$ and $T_{\rm p}$. These values are so chosen that the squared mean velocity is constant, i.e., $< v^2 >= 250$ eV. The solid curves represent the cigar-shaped EVDF; $T_{\rm t} > T_{\rm p}$, and the dashed curves for pancake-shaped EVDF; $T_{\rm t} < T_{\rm p}$. The degree of anisotropy, α_K is shown in Fig. 68. In the limit of the thin pancake-like EVDF; i.e., when the poloidal component is predominant, we have $\alpha_2 = -\frac{1}{2}$. When the EVDF is in the limit of the cigar-shape; i.e., toroidal component is predominant, we have $\alpha_2 = 1$.

Firstly we focus on the population and alignment of the $2^3{\rm P}_{0,1,2}$ state, since the emission lines from $2^3{\rm P}_{0,1,2}$ to $2^3{\rm S}_1$ at around 227 nm in the UV region are observed in many plasma diagnostics experiments. By integrating the cross sections $Q_q^{kk'}$ multiplied by the Legendre expansion coefficient v cubed, $f_K(v)v^3$, shown in Fig. 58, in velocity space, we obtain the rate coefficients $C^{kk'}$ for the thermal-bulk-with-beam Maxwellian represented by Eq.(18) with the parameters $T_{\rm eth} = T_{\rm eb} = 250$ eV and $V_z = 1.87 \times 10^7$ m/s with the parameter δ. Figure 69 shows the dominant rate coefficients for population C^{00} and for alignment production from population C^{20}, from the ground state *1*, $1^1{\rm S}_0$, to *6*, $2^3{\rm P}_2$, and from the metastable state *2*, $2^3{\rm S}_1$, to *6*, $2^3{\rm P}_2$, as functions of δ.

The rate coefficients C^{00} for both transitions are little affected by the change of δ below 0.1. With the increase in δ from $\delta = 0.1$, they decrease gradually to about 40% of the isotropic distribution (i.e. $\delta = 0$). The absolute values of the alignment production rate coefficients, C^{20}, increase with the increase in δ. Larger anisotropy in the electron velocity distribution creates larger alignments. The alignment-production rate coefficients C^{20} from level *2* to *6* take positive values and are of the order of 10^{-15} m^{3}s^{-1}, while the C^{20} from *1* to *6* are negative and are of the order of 10^{-18} m^{3}s^{-1}. The alignment production in level *6*

2^3P_2 from the ground state *1* tends to cancel the alignment production from the metastable state *2*.

Figure 70 shows the alignment-production flux to level *6* from populations of other levels, $\sum_{r \neq p} C^{20}(r,p) n_e n(r)$, for two electron densities $n_e = 10^{14}$ and 10^{19} m^{-3}. The alignment production fluxes $C^{20}(r,6) n_e n(r)$ from the ground state $r = 1$ population and from the metastable $r = 2$ populations are the two dominant processes. When the electron density is low, $n_e = 10^{14}$ m^{-3}, the alignment production from the ground state *1*; $C^{20}(1,6) n_e n(1)$, is predominant, which produces negative alignment. On the other hand, when n_e becomes higher, the population of level *2* becomes larger, as is seen in Fig 54, and the alignment production from level *2* becomes high enough to exceed the contribution from the ground state. At $n_e = 10^{19}$ m^{-3} the alignment produced is positive. The next dominant process is alignment-production from level *3*, $1s2s\,^1S_0$, however, the contribution is an order of magnitude smaller than the dominant fluxes. It can be concluded that other fluxes producing alignment in level *6* are negligibly small as well as the alignment-transfer process represented by $C^{22}(r,6) a(r) n_e$.

Figure 71 shows the population $n(6)$ and the alignment $a(6)$ of level *6* as functions of δ for various electron densities. The alignment $a(6)$ produced is positive for the region of $n_e \geq 10^{16}$ m^{-3}. While, below $n_e = 10^{15}$ m^{-3}, the alignment $a(6)$ is negative. Around $n_e = 1.35 \times 10^{15}$ m^{-3}, $a(6)$ changes its sign depending on δ. The electron density dependence of $a(6)$ is explained by the fact that the alignment production flux $C^{20}(2,6) n_e n(2)$ from the metastable level is larger than the alignment production flux $C^{20}(1,6) n_e n(1)$ for $n_e > 1.4 \times 10^{-15}$ m^{-3}.

Figure 72 shows the population $n(p)$, alignment $a(p)$ and their ratio $a(p)/n(p)$ for all 17 levels with the velocity distribution with the parameters $\delta = 0.3$, $T_{eth} = T_{eb} = 250$ eV and $V_z = 1.87 \times 10^7$ m/s for $n_e = 10^{19}$ m^{-3} and $n(1) = 1$ m^{-3}. For the $J = 0$ levels, i.e, for *1,3,5,9* and *11* alignment is absent. The ^1P levels, *7* and *17*, have relatively large alignment-to-population ratios.

As shown in Fig. 73, the longitudinal alignments A_L defined by Eq.(9) of the emission lines of $J = 1 \leftarrow 2$ and $J = 1 \leftarrow 1$ are positive at low electron densities and gradually decrease with increasing n_e. The sign of A_L changes at $n_e = 1.4 \times 10^{15}$m^{-3} and at $= 7 \times 10^{15}$m^{-3} for RDW and *R*-matrix, respectively. The $A_L(J = 1 \leftarrow 2)$ depends little on the electron density in the region between 10^{15} and 10^{20} m^{-3} , and then gradually decreases with the increase of

electron density over 10^{21} m^{-3}.

Figure 74 shows the dependence of $A_{\rm L}$ on the shifted velocity V_z at the electron density of 10^{19} m^{-3}, $\delta = 0.3$, $T_{\rm eth} = T_{\rm eb}$= 250 eV. The absolute value of $A_{\rm L}$ is maximum at $V_z = 2.5 \times 10^7$ m/s. In the V_z range of this figure, with the the increase in V_z, the populations decrease by 50%, while the population ratios of $n(4)/n(6)$ and $n(5)/n(6)$ remain almost constant. The polarization of the triplet lines CV $2^3{\rm S}_1 - 2^3{\rm P}_{0,1,2}$ depends significantly on the anisotropy of the electron velocity distribution, while the intensity ratios between the triplet lines are little affected by the change in the degree of anisotropy. High energy electron beam component above 3 keV is found to little effect $A_{\rm L}$ of the emission lines. The cross section data used in the present PACR model for CV are provided below the electron collision energy of 3 keV, which corresponds to electron collision velocity of $v = 3.2 \times 10^7$ m/s. The model calculations are reliable under the condition that the contributions from the component of velocities lower than this values are significant.

Figure 75 shows the dependence of $A_{\rm L}$ of the $J = 1 \leftarrow 2$ on δ, the ratio of the beam component to the thermal bulk. $A_{\rm L}(J = 1 \leftarrow 2)$ linearly increases with increasing δ below $\delta < 1$. At $\delta = 1$, when the thermal and beam components of the EVDF are equal, $A_{\rm L}(J = 1 \leftarrow 2) = +0.0078$ and -0.0094 for $n_{\rm e} = 10^{14}$ and 10^{19} m^{-3}, respectively. For the Saturn type EVDFs, the dependence of $A_{\rm L}$ of the $J = 1 \leftarrow 2$ transition on the ratio δ is shown in Fig. 76. At $\delta = 1$, when the thermal and ring components of the EVDF are equal, $A_{\rm L}(J = 1 \leftarrow 2) = -0.013$ and $+0.012$ for $n_{\rm e} = 10^{14}$ and 10^{19} m^{-3},respectively. For the two temperature EVDFs shown in Fig. 77, above the electron density $n_{\rm e} = 10^{16}$m^{-3} $A_{\rm L}(J = 1 \leftarrow 2)$ take values between -0.019 and 0.014 for the pairs of parameters, $(T_{\rm t}, T_{\rm p})$, where $T_{\rm t}$ and $T_{\rm p}$, are selected so that the mean squared value of v is constant; $\frac{1}{2}m<v^2>$= 250 eV.

For the EVDF with modest anisotropy, e.g., $\delta < 0.1$, $A_{\rm L}(J = 1 \leftarrow 2)$ takes values of the order of 0.01 or less. In order to experimentally determine $A_{\rm L}$ of these magnitudes the experimental uncertainty should be $\Delta A_{\rm L}(J = 1 \leftarrow 2) \sim 0.001$. As the absolute values of the $A_{\rm L}$ become small, it is more difficult to measure the polarization accurately. The limit of the observed $A_{\rm L}$ depends on the various experimental conditions, the detected photon numbers, the stability of the plasma observed and so on. When the plasma is steady and quiet, the polarization of the order of 10^{-4} can be observed in high precision plasma polarimetry, and qualitative evaluation is possible for the anisotropy of the EVDF for $\delta \sim 0.01$ from the polarization of the CV $2^3{\rm S}_1 - 2^3{\rm P}_{0,1,2}$ emission lines.

In contrast to the triplet lines treated above, as Fig. 72 suggests, the situation is much more favorable with the resonance line. Polarization observations in the X-ray regions from plasmas is a new tool for investigating the anisotropy of high-temperature plasmas[43, 44]. In Fig. 78 and 79, the longitudinal alignment, $A_{\rm L}(1 \leftarrow 7)$, of the 4.027 nm emission line of the $1s^2\,{}^1S \leftarrow 1s2p\,{}^1P$ transition, is plotted for various EVDFs. The alignment creation from the ground state population, Q_0^{20} is the dominant processes. The calculated $A_{\rm L}(1 \leftarrow 7)$ is positive for the toroidal dominant EVDF: bulk with beam type and two temperature EVDFs with $T_{\rm t} > T_{\rm p}$, and negative for the poloidal dominant: the Saturn type and the two temperature EVDFs with $T_{\rm t} < T_{\rm p}$. The calculated $A_{\rm L}(1 \leftarrow 7)$ is less dependent on the electron densities under the assumed conditions. The magnitude of the $A_{\rm L}(1 \leftarrow 7)$ is one-order larger than that of $A_{\rm L}(2 \leftarrow 6)$ or $A_{\rm L}(2 \leftarrow 4)$ for the same EVDFs.

Acknowledgments

This work was partially supported by the collaboration program of National Institute for Fusion Science and by the Ministry of Education, Science and Culture, Grant-in-Aid for Young Scientist (B), no. 13780386. Work at Los Alamos National Laboratory has been performed under the auspices of the U.S. Department of Energy.

[1] S. A. Kazantsev and A. V. Subbotenko, J. Phys. D: Appl. Phys. **20**, 741 (1987).

[2] A. I. Drachev, S. A. Kazantsev, A. G. Rys, and A. V. Subbotenko, Opt. Spectosc. **70**, 159 (1991).

[3] H. Yoneda, N. Hasegawa, S. Kawana, and K. Ueda, Phys. Rev. E **56**, 988 (1997).

[4] J. C. Kieffer, J. P. Matte, H. Pépin, M. Chaker, Y. Beaudoin, T. W. Johnston, C. Y. Chien, S. Coe, G. Mourou, and J. Dubau, Phys. Rev. Lett. **68**, 480 (1992).

[5] J. C. Kieffer, J. P. Matte, M. Chaker, Y. Beaudoin, C. Y. Chien, S. Coe, G. Mourou, J. Dubau, and M. K. Inal, Phys. Rev. E **48**, 4648 (1993).

[6] J. Kim and D. Kim, Phys. Rev. E **66** (2002).

[7] T. Fujimoto, H. Sahara, T. Kawachi, T. Kallstenius, M. Goto, H. Kawase, T. Furukubo, T. Maekawa, and Y. Terumichi, Phys. Rev. E **54**, R2240 (1996).

[8] L. Pieroni and S. E. Segre, Phys. Rev. Lett. **14**, 928 (1974).

[9] B. Coppi, F. Pegoraro, R. Pozzoli, and G. Rewoldt, Nucl. Fusion **16**, 309 (1976).

[10] K. Ogura, H. Tanaka, S. Ide, M. Iida, K. Hanada, M. Yoshida, T. Minami, T. Cho, M. Nakamura, T. Maekawa, et al., Nucl. Fusion **31**, 1015 (1991).

[11] M. M. Turner and M. B. Hopkins, Phys. Rev. Lett. **69**, 3511 (1992).

[12] J. V. Scanlan and M. B. Hopkins, J. Vac. Sci. Technol. **A 10**, 1207 (1992).

[13] V. A. Godyak and R. B. Piejak, Phys. Rev. Lett. **65**, 996 (1990).

[14] M. B. Hopkins, J. Res. Natl. Inst. Stand. Technol. **100**, 415 (1995).

[15] A. Omont, Prog. Quantum Electron. **5**, 69 (1977).

[16] K. Blum, *Density Matrix Theory and Applications -2nd ed.-* (Plenum Press, 1996).

[17] B. W. Shore and D. H. Menzel, *Principles of Atomic spectra* (John Wiley and Sons, Inc., New York, 1968).

[18] P. H. Heckmann and E. Träbert, *Introduction to the Spectrosopy of Atoms* (North-Holland Physics (Elsevier Science Publishers B.V.), 1989).

[19] T. Fujimoto and S. A. Kazantsev, Plasma Phys. Control. Fusion **39**, 1267 (1997).

[20] A. Iwamae, A. Tanaka, T. Inoue, T. Fujimoto, H. L. Zhang, D. P. Kilcrease, and G. Csanak, Proceedings of the 3rd US-Japan Plasma Polarization Spectroscopy Workshop p. 165 (2001).

[21] D. H. Sampson, H. L. Zhang, A. K. Mohanty, and R. E. Clark, Phys. Rev. A **40**, 604 (1989).

[22] H. L. Zhang, D. H. Sampson, and A. K. Mohanty, Phys. Rev. A **40**, 616 (1989).

[23] H. L. Zhang, D. H. Sampson, and R. E. Clark, Phys. Rev. A **41**, 198 (1990).

[24] H. L. Zhang and D. H. Sampson, Phys. Rev. A **52**, 3827 (1995).

[25] K. A. Berrington, P. G. Burke, M. Le Dourneuf, W. D. Robb, K. T. Taylor, and V. K. Lan, Comput. Phys. Commun. **14**, 367 (1978).

[26] N. S. Scott and K. T. Taylor, Comput. Phys. Commun. **25**, 347 (1982).

[27] K. A. Berrington, W. Eissner, and P. N. Norrington, Comput. Phys. Commun. **92**, 290 (1995).

[28] K. Bartschat and N. S. Scott, Comp. Phys. Commun. **30**, 369 (1983).

[29] P. G. Burke and K. A. Berrington, eds., *Atomic and Molecular Processes: An R-matirx Approach* (Bristol: Institute of Physics Publishing, 1993).

[30] E. Clementi and C. Roetti, Atom. Data Nucl. Data Tables **14**, 17 (1974).

[31] A. Hibbert, Comput. Phys. Commun. **9**, 141 (1975).

[32] E. G. Harris, Phys. Rev. Lett. **2**, 34 (1959).

[33] R. Z. Sagdeev and V. D. Shafranoc, Sov. Phys. JETP **12**, 130 (1961).

[34] J. Sharer and A. Trivelpiece, Phys. Fluids **10**, 591 (1967).

[35] H. Ikegami, H. Ikeze, T. Kawamura, H. Momota, K. Takayama, and Y. Terashima, Plasma Physics and Controlled Nuclear Fusion Research **2**, 423 (1969).

[36] L. B. Golden and D. H. Sampson, J. Phys. B:Atom. Molec. Phys. **10**, 2229 (1977).

[37] D. H. Sampson and L. B. Golden, J. Phys. B:Atom. Molec. Phys. **11**, 541 (1978).

[38] L. B. Golden, D. H. Sampson, and K. Omidvar, J. Phys. B:Atom. Molec. Phys. **11**, 3235 (1978).

[39] D. L. Moores, L. B. Golden, and D. H. Sampson, J. Phys. B:Atom. Molec. Phys. **13**, 385 (1980).

[40] G. Csanak, D. P. Kilcrease, H. L. Zhang, D. V. Fursa, I. Bray, T. Fujimoto, and A. Iwamae, Proceedings of the 3rd US-Japan Plasma Polarization Spectroscopy Workshop p. 153 (2001).

[41] T. Fujimoto and T. Kato, Phys. Rev. A **30**, 379 (1984).

[42] C. D. Lin, W. R. Johnson, and A. Dalgarno, Phys. Rev. A **15**, 154 (1976).

[43] G. Bertschinger, W. Biel, the TEXTOR-94 Team, O. Herzog, J. Weinheimer, H. J. Kunze, and M. Bitter, Phys. Scripta **T83**, 132 (1999).

[44] A. S. Shlyaptseva, S. B. Hansen, V. L. Kantsyrev, B. S. Bauer, D. A. Fedin, N. Ouart, S. A. Kazantsev, A. G. Petrashen, and U. I. Safranova, Rev. Sci. Instrum. **72**, 1241 (2001).

TABLE I: Configuration and Energy levels (eV) for Hellium-like carbon. K is an index label assigned to each level.

configuration	K	E (eV)
$1s^2\,{}^1S_0$	1	0.0000
$1s2s\,{}^3S_1$	2	298.9596
$1s2s\,{}^1S_0$	3	304.3843
$1s2p\,{}^3P_1$	4	304.4008
$1s2p\,{}^3P_0$	5	304.4003
$1s2p\,{}^3P_2$	6	304.4176
$1s2p\,{}^1P_1$	7	307.8989
$1s3s\,{}^3S_1$	8	352.0624
$1s3s\,{}^1S_0$	9	353.5010
$1s3p\,{}^3P_1$	10	353.5294
$1s3p\,{}^3P_0$	11	353.5296
$1s3s\,{}^3P_2$	12	354.2344
$1s3d\,{}^3D_1$	13	354.2608
$1s3d\,{}^3D_2$	14	354.2609
$1s3d\,{}^3D_3$	15	354.2624
$1s3d\,{}^1D_2$	16	354.2886
$1s3p\,{}^1P_1$	17	354.5174

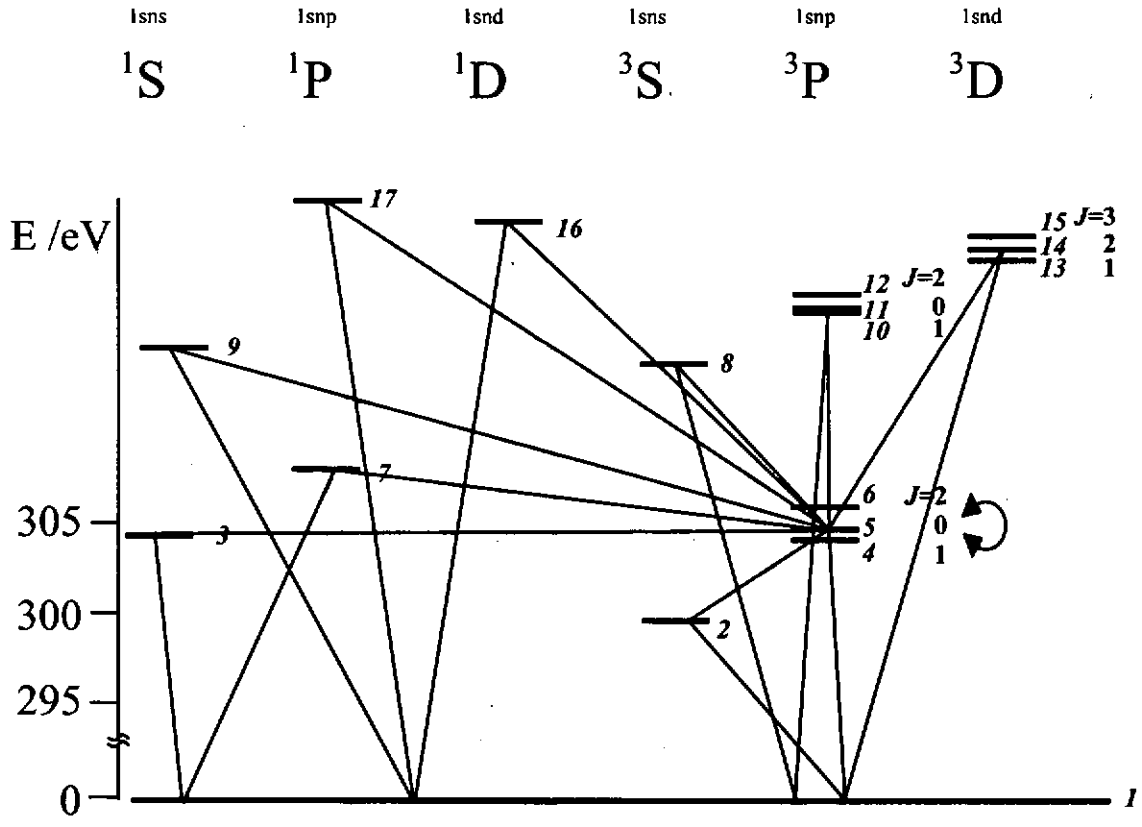

FIG. 1: Level diagram of hellium-like carbon. Seventeen levels are included in the PACR model.

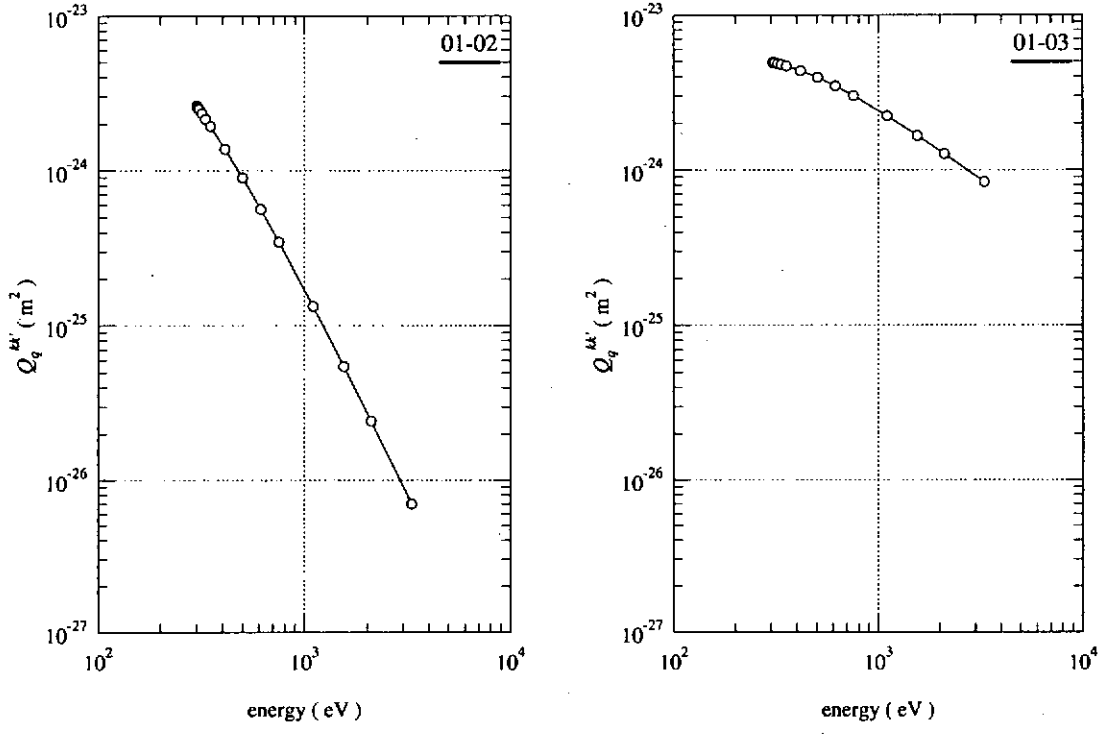

FIG. 2: Excitation cross sections from *1* to *2* and from *1* to *3*. Q_0^{00}: open circle. The Q_0^{20} from *1* to *2* is negligiblly small.

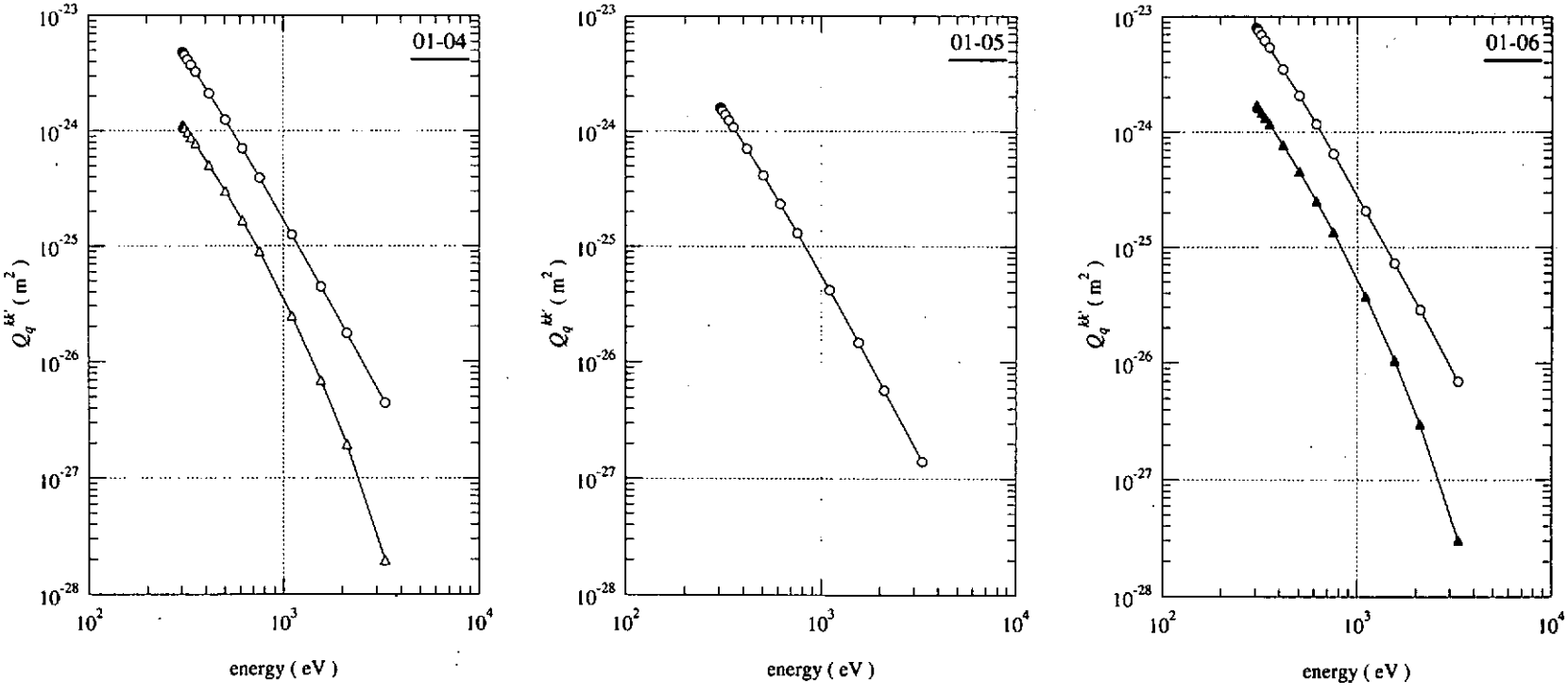

FIG. 3: Excitation cross sections from *1* to *4*, from *1* to *5* and from *1* to *6*. Q_0^{00}: open circle and Q_0^{20}: triangle. The filled triangles show that the Q_0^{20} take negative values.

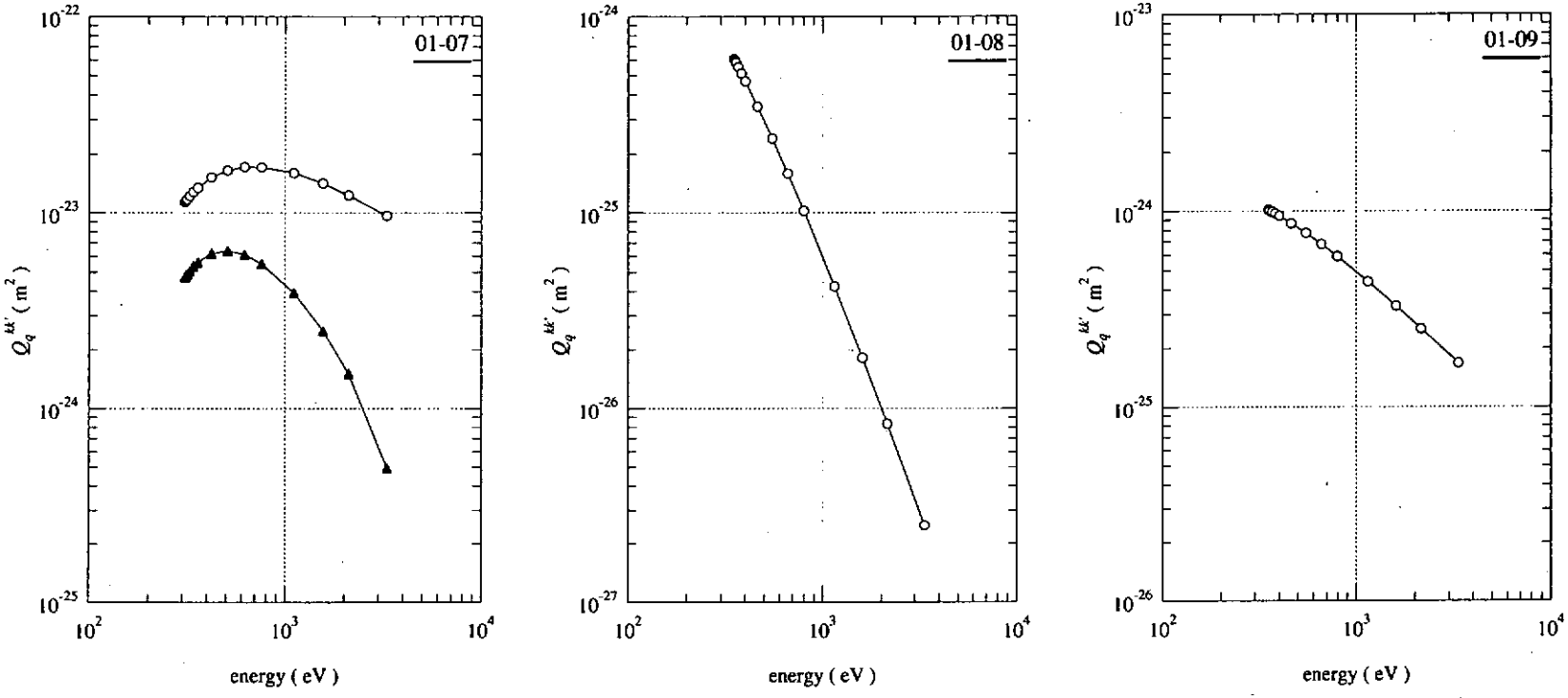

FIG. 4: Excitation cross sections from *1* to *7*, from *1* to *8* and from *1* to *9*. Q_0^{00}: open circle and Q_0^{20}: triangle. The Q_0^{20} from *1* to *8* is negligiblly small. The filled triangles show that the Q_0^{20} take negative values.

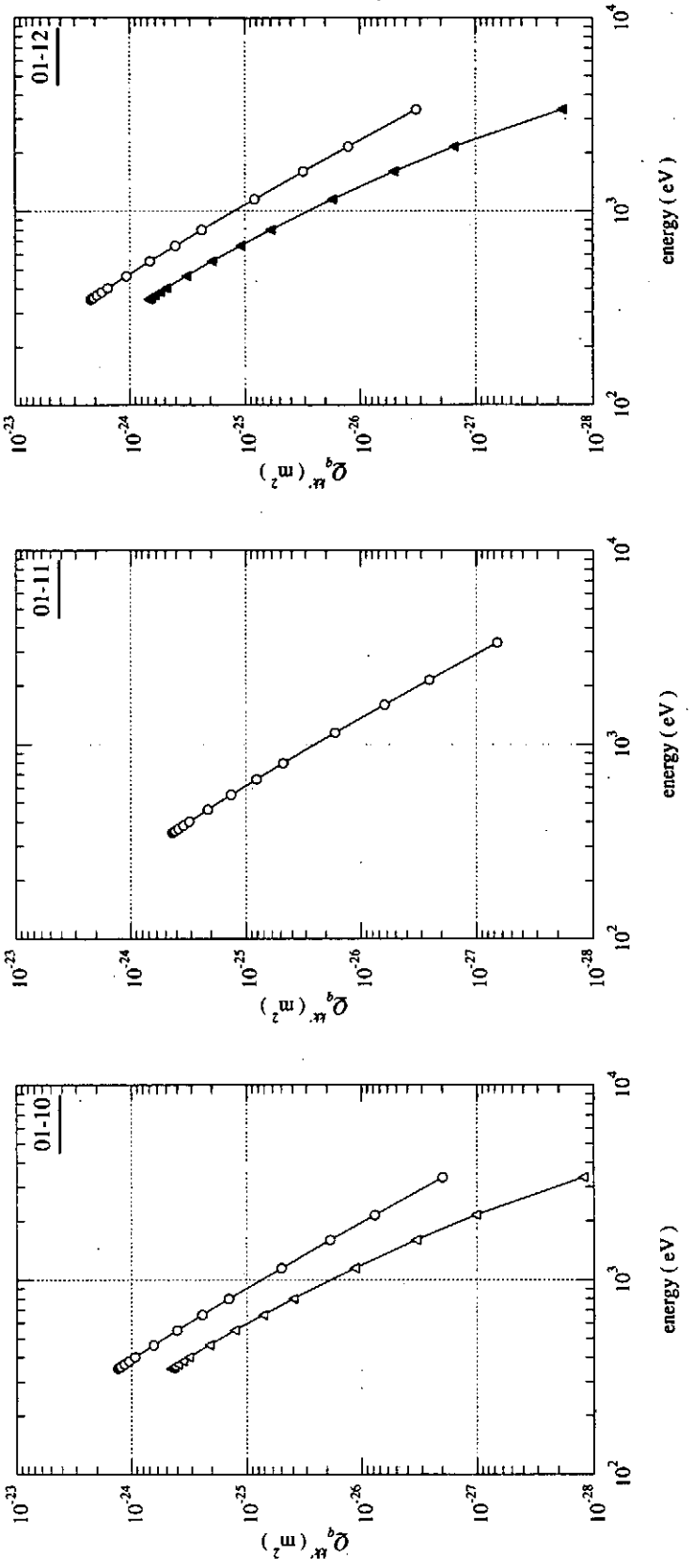

FIG. 5: Excitation cross sections from *1* to *10*, from *1* to *11* and from *1* to *12*. Q_0^{00}: open circle and Q_0^{20}: triangle. The filled triangles show that the Q_0^{20} take negative values.

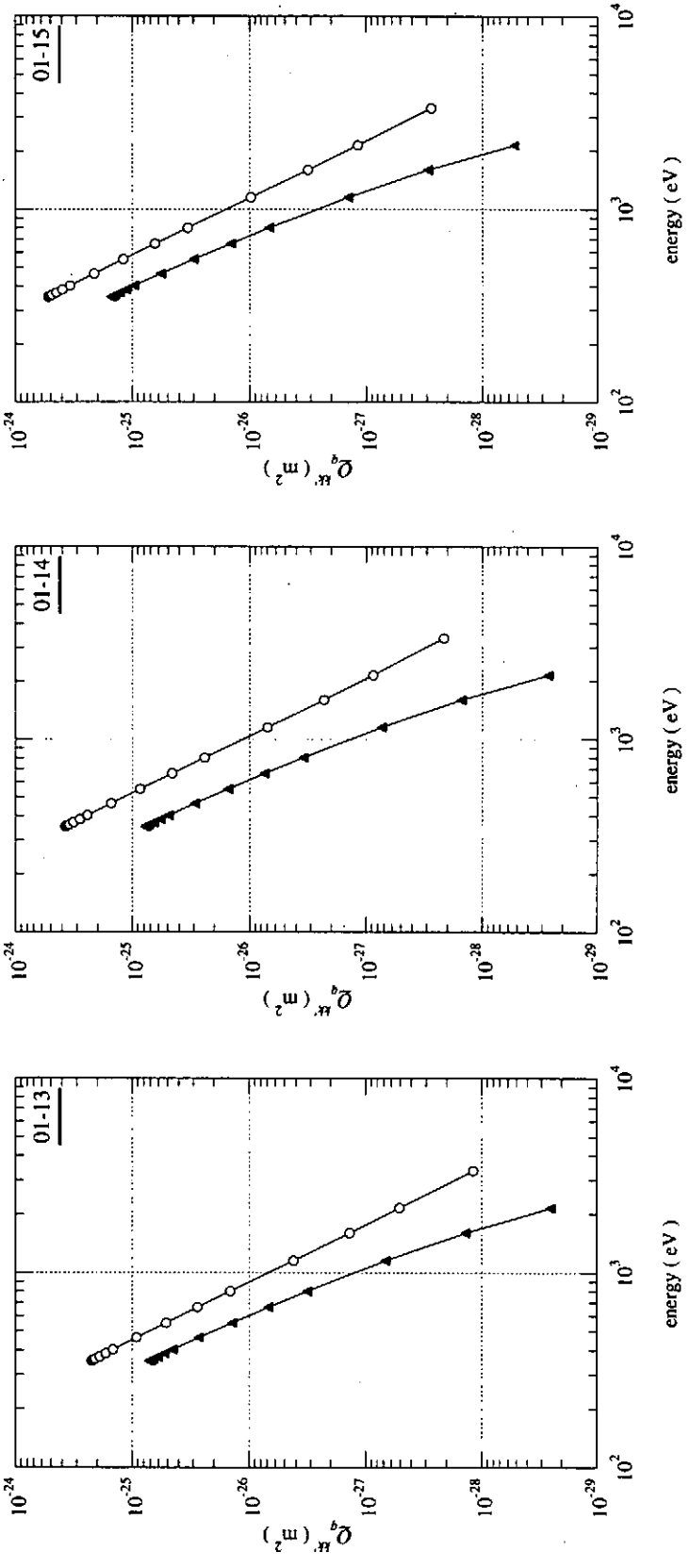

FIG. 6: Excitation cross sections from *1* to *13*, from *1* to *14* and from *1* to *15*. Q_0^{00}: open circle and Q_0^{20}: triangle. The filled triangles show that the Q_0^{20} take negative values.

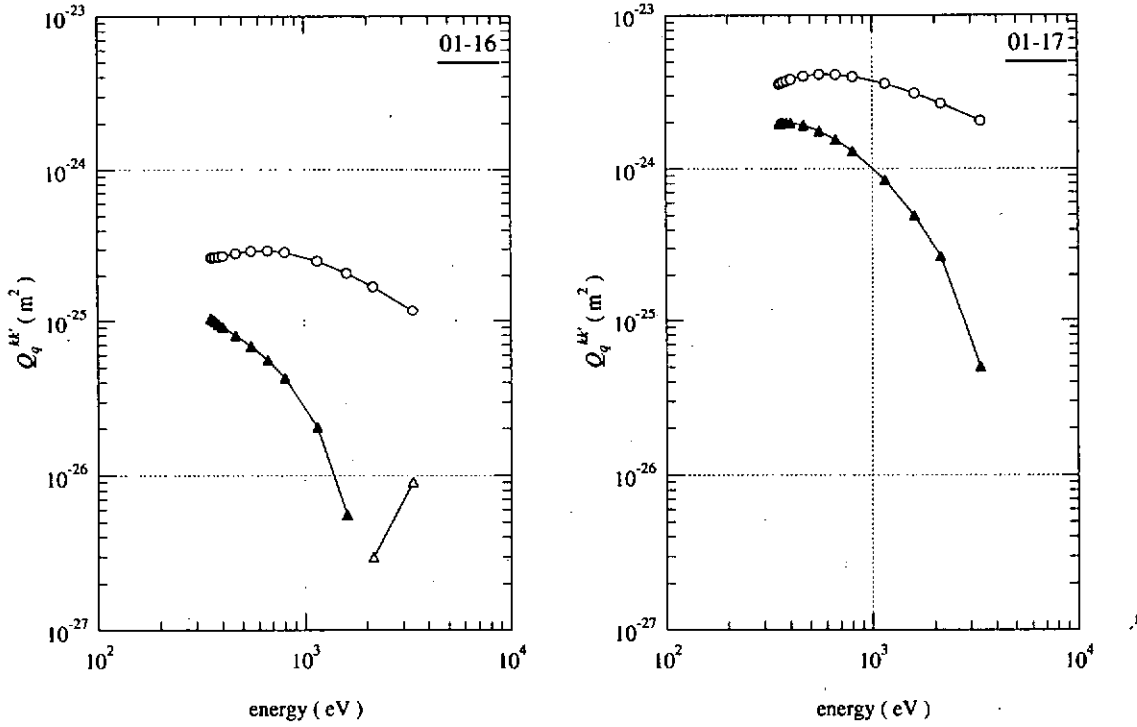

FIG. 7: Excitation cross sections from *1* to *16* and from *1* to *17*. Q_0^{00}: open circle and Q_0^{20}: triangle. The filled triangles show that the Q_0^{20} take negative values.

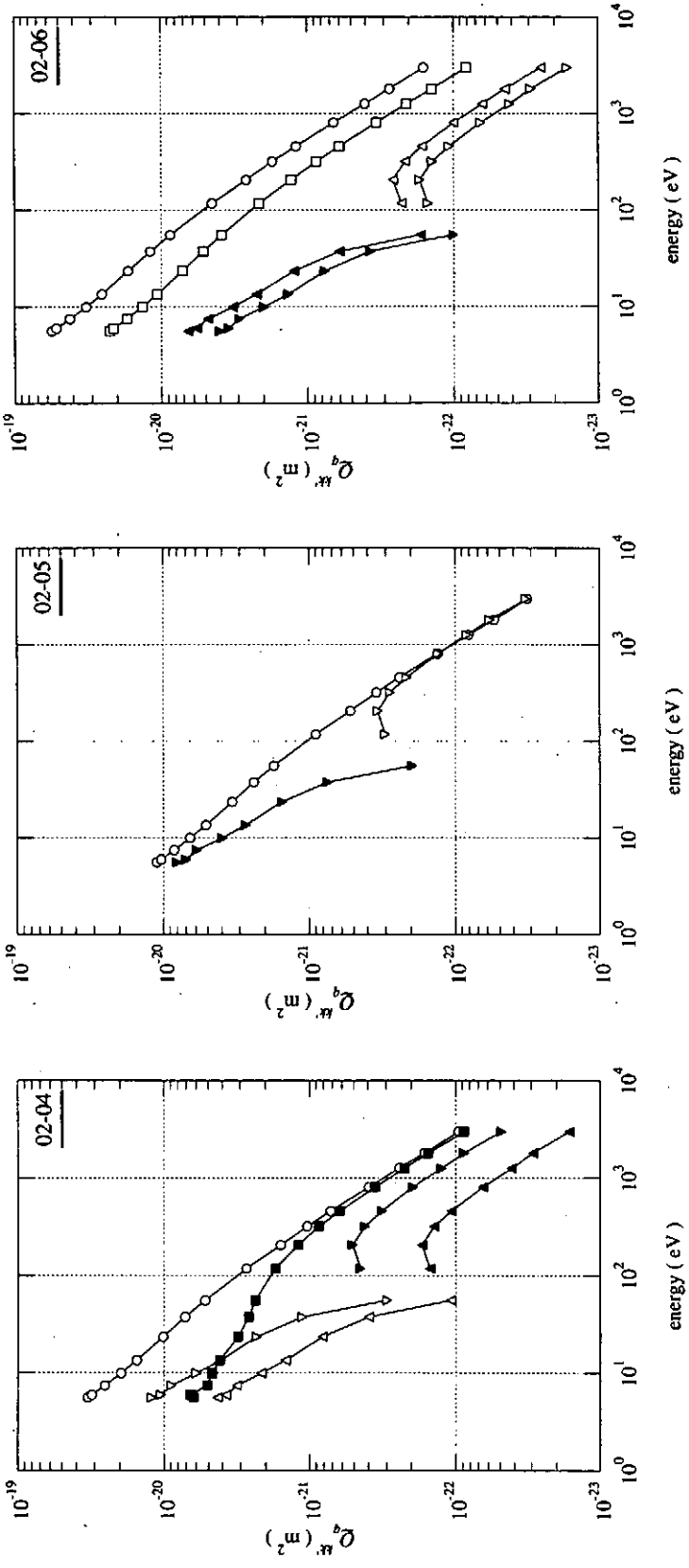

FIG. 8: Excitation cross sections from 2 to 4, from 2 to 5 and from 2 to 6. Q_0^{00}: open circle, Q_0^{20}: triangle, Q_0^{02}: inverted triangle and Q_0^{22}: square. The filled marks show that cross sections take negative values.

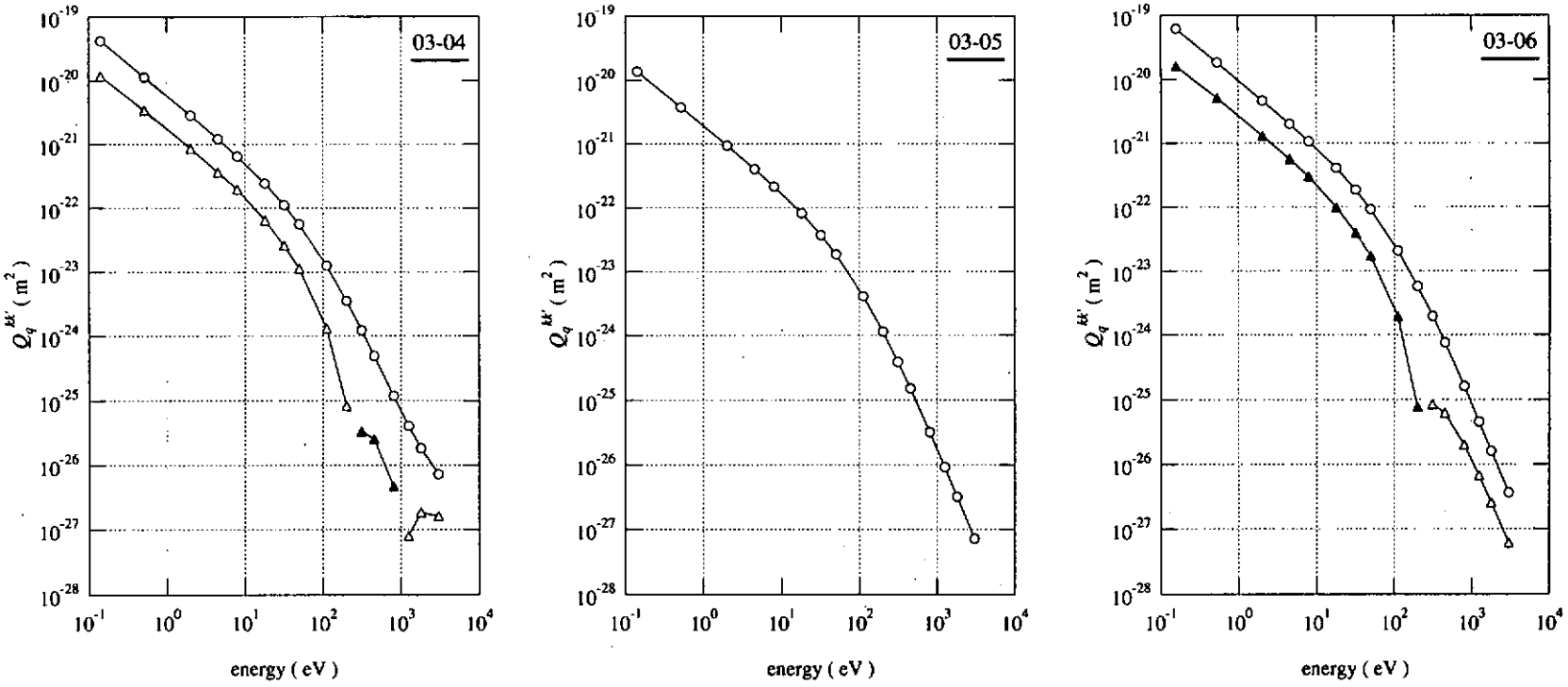

FIG. 9: Excitation cross sections from *3* to *4*, from *3* to *5* and from *3* to *6*. Q_0^{00}: open circle and Q_0^{20}: triangle. The filled triangles show that the Q_0^{20} take negative values.

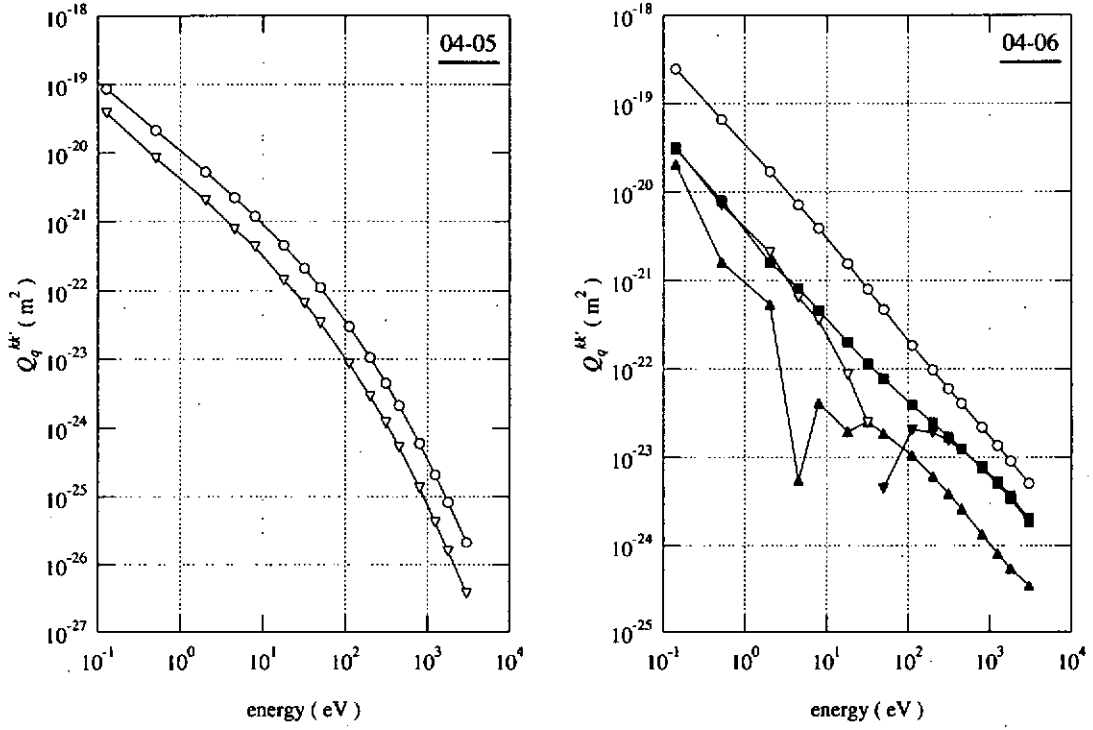

FIG. 10: Excitation cross sections from *4* to *5*, from *4* to *6* and from *5* to *6*. Q_0^{00}: open circle, Q_0^{20}: triangle, Q_0^{02}: inverted triangle and Q_0^{22}: square. The filled marks show that cross sections take negative values.

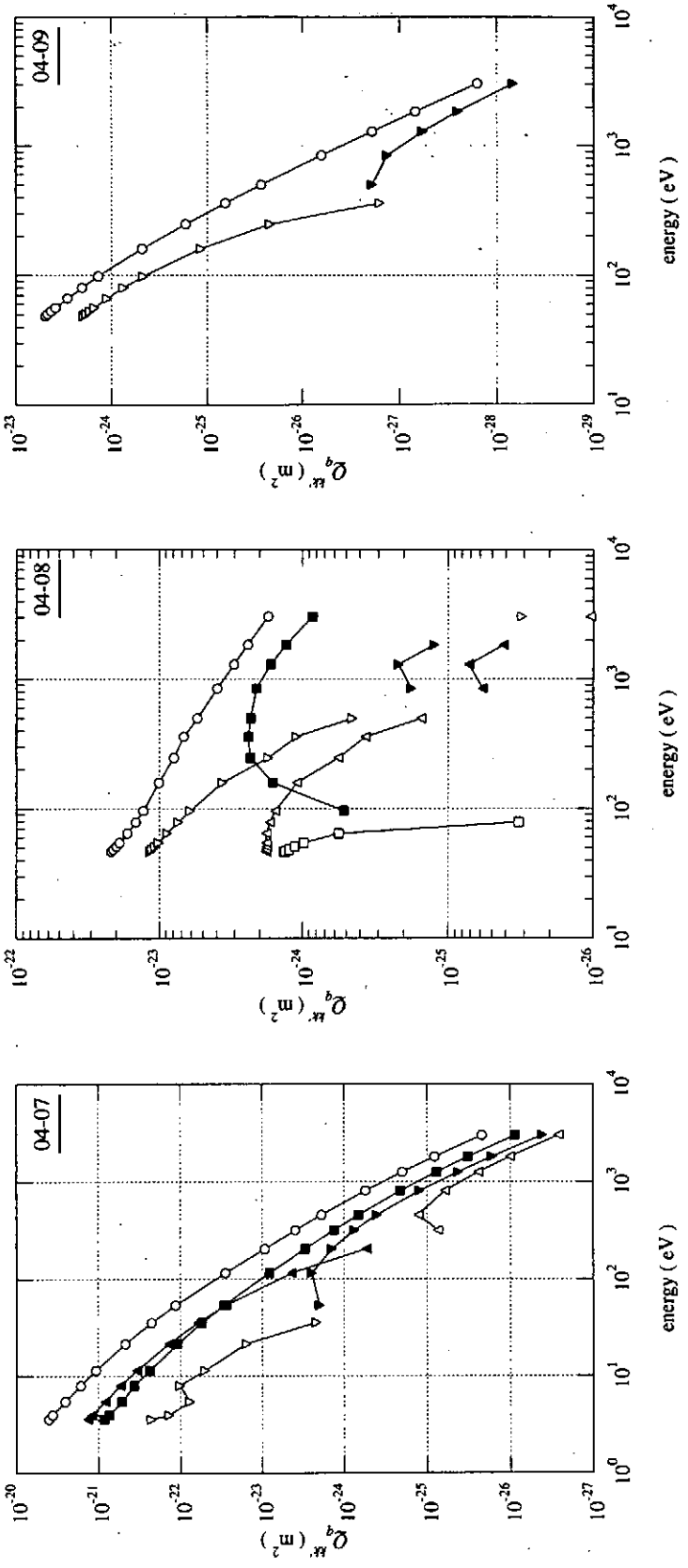

FIG. 11: Excitation cross sections from 4 to 7, from 4 to 8 and from 4 to 9. Q_0^{00}: open circle, Q_0^{20}: triangle, Q_0^{02}: inverted triangle and Q_0^{22}: square. The filled marks show that cross sections take negative values.

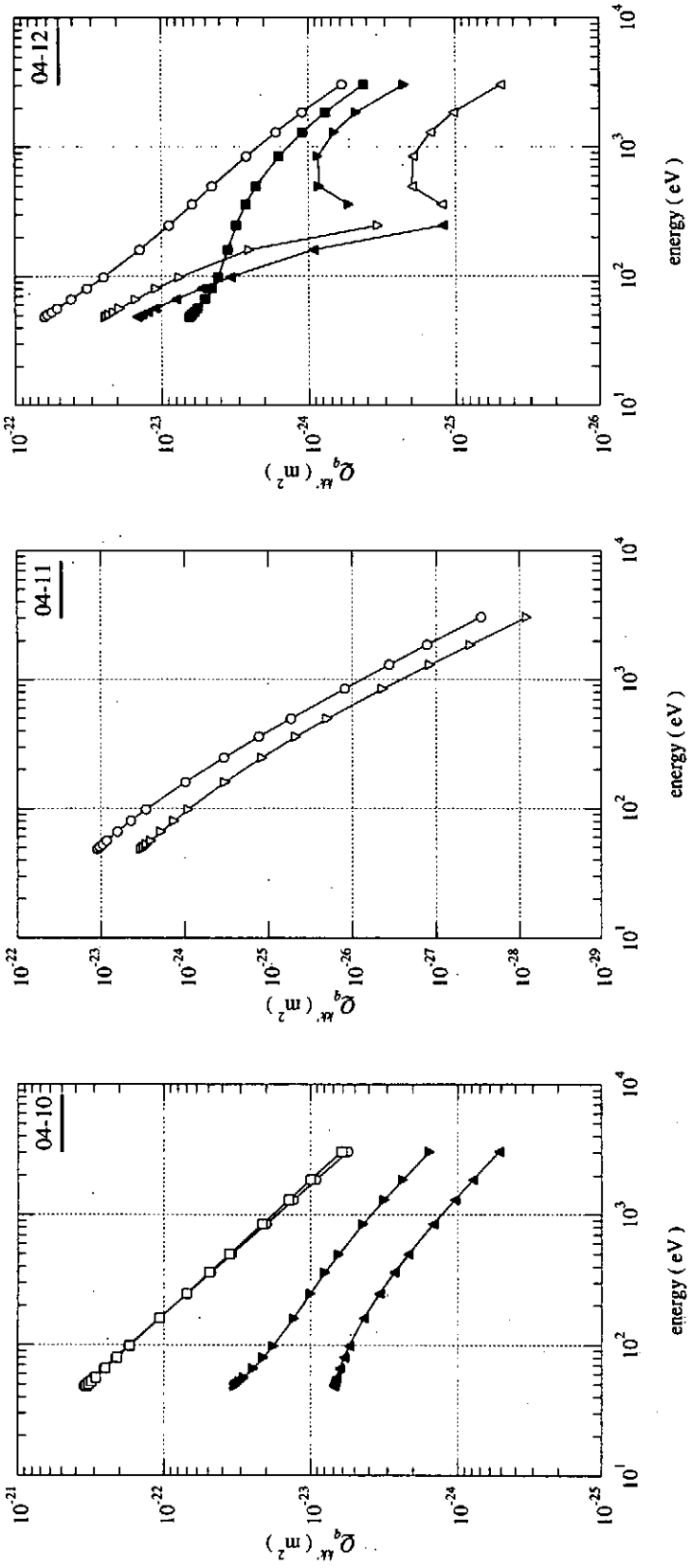

FIG. 12: Excitation cross sections from *4* to *10*, from *4* to *11* and from *4* to *12*. Q_0^{00}: open circle, Q_0^{20}: triangle, Q_0^{02}: inverted triangle and Q_0^{22}: square. The filled marks show that cross sections take negative values.

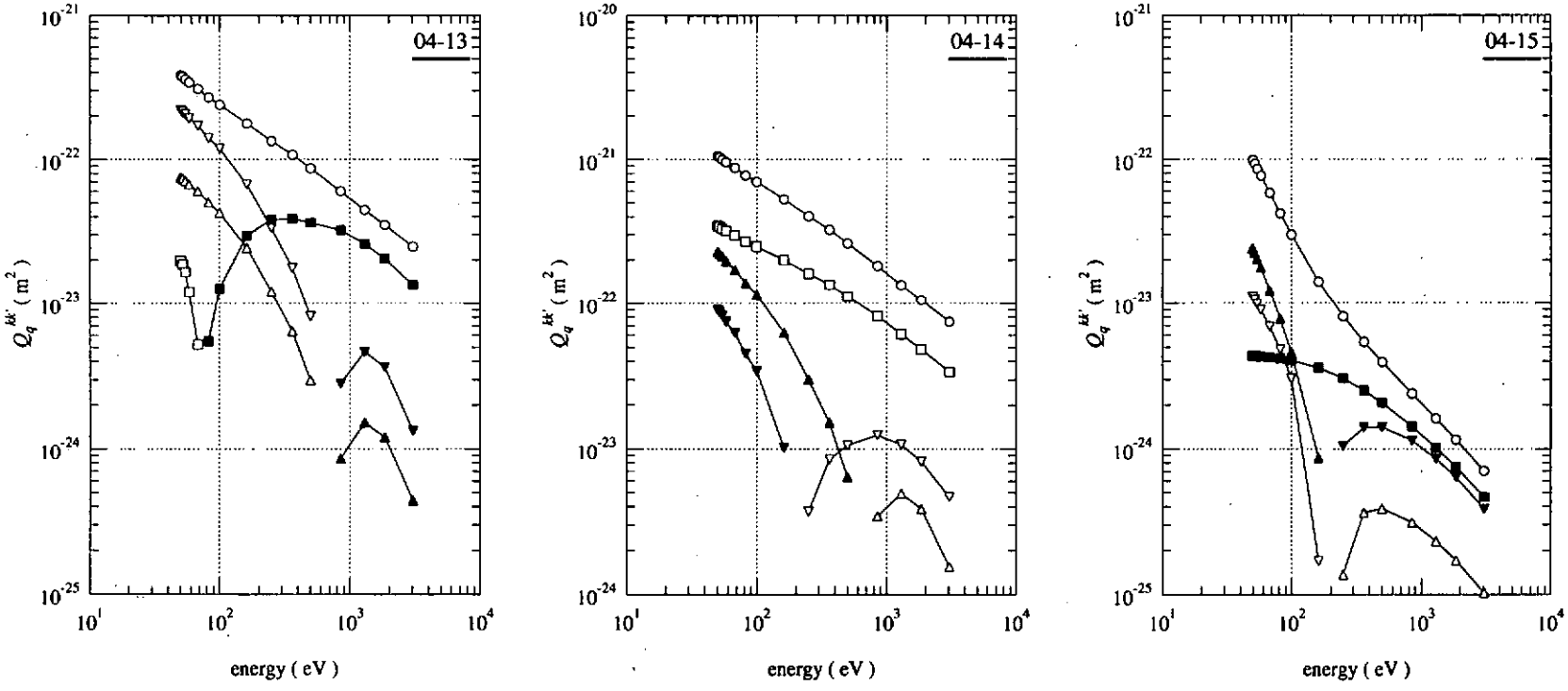

FIG. 13: Excitation cross sections from *4* to *13*, from *4* to *14* and from *4* to *15*. Q_0^{00}: open circle, Q_0^{20}: triangle, Q_0^{02}: inverted triangle and Q_0^{22}: square. The filled marks show that cross sections take negative values.

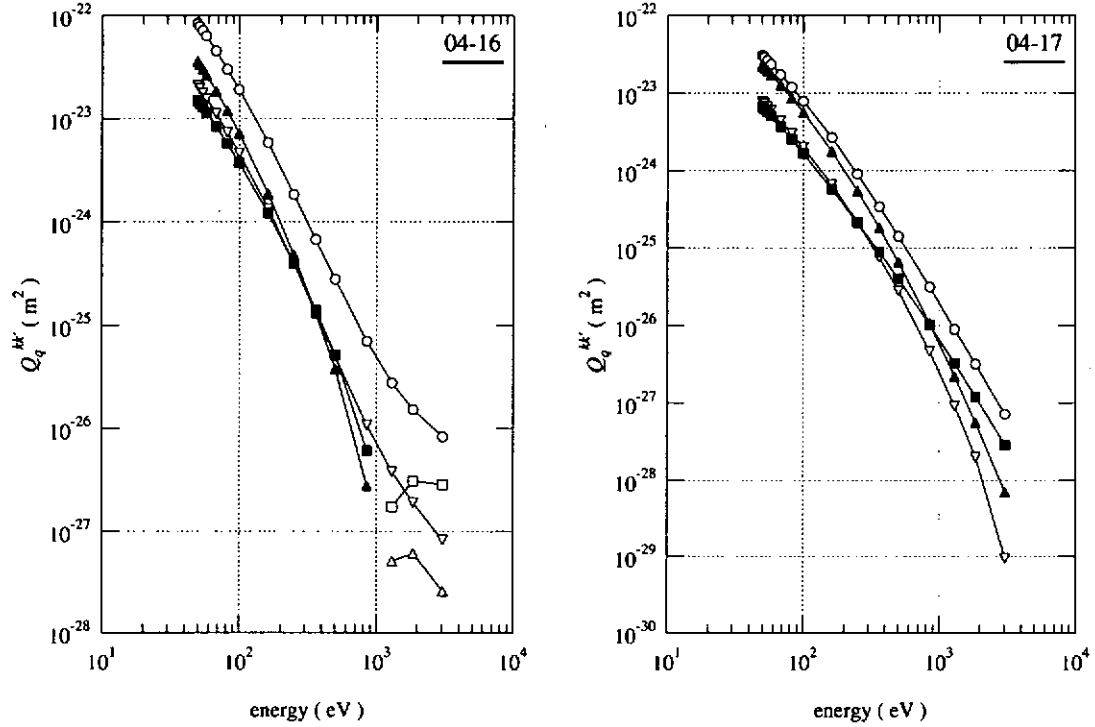

FIG. 14: Excitation cross sections from *4* to *16* and from *4* to *17*. Q_0^{00}: open circle, Q_0^{20}: triangle, Q_0^{02}: inverted triangle and Q_0^{22}: square. The filled marks show that cross sections take negative values.

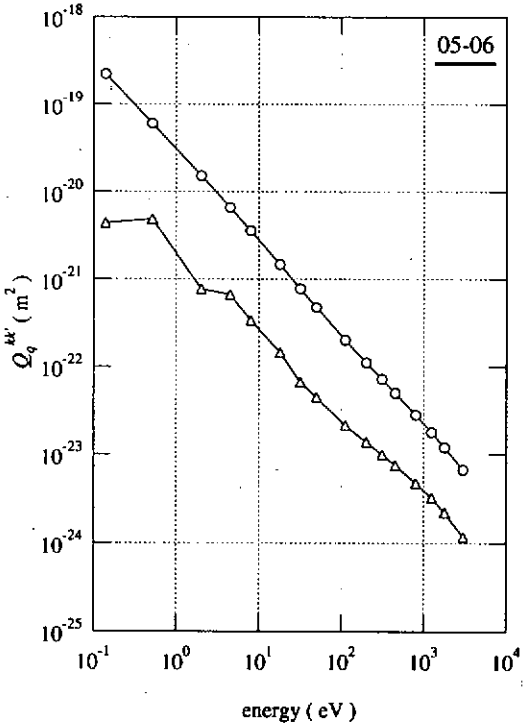

FIG. 15: Excitation cross sections from *5* to *6*. Q_0^{00}: open circle and Q_0^{20}: triangle. The filled triangles show that the Q_0^{20} take negative values.

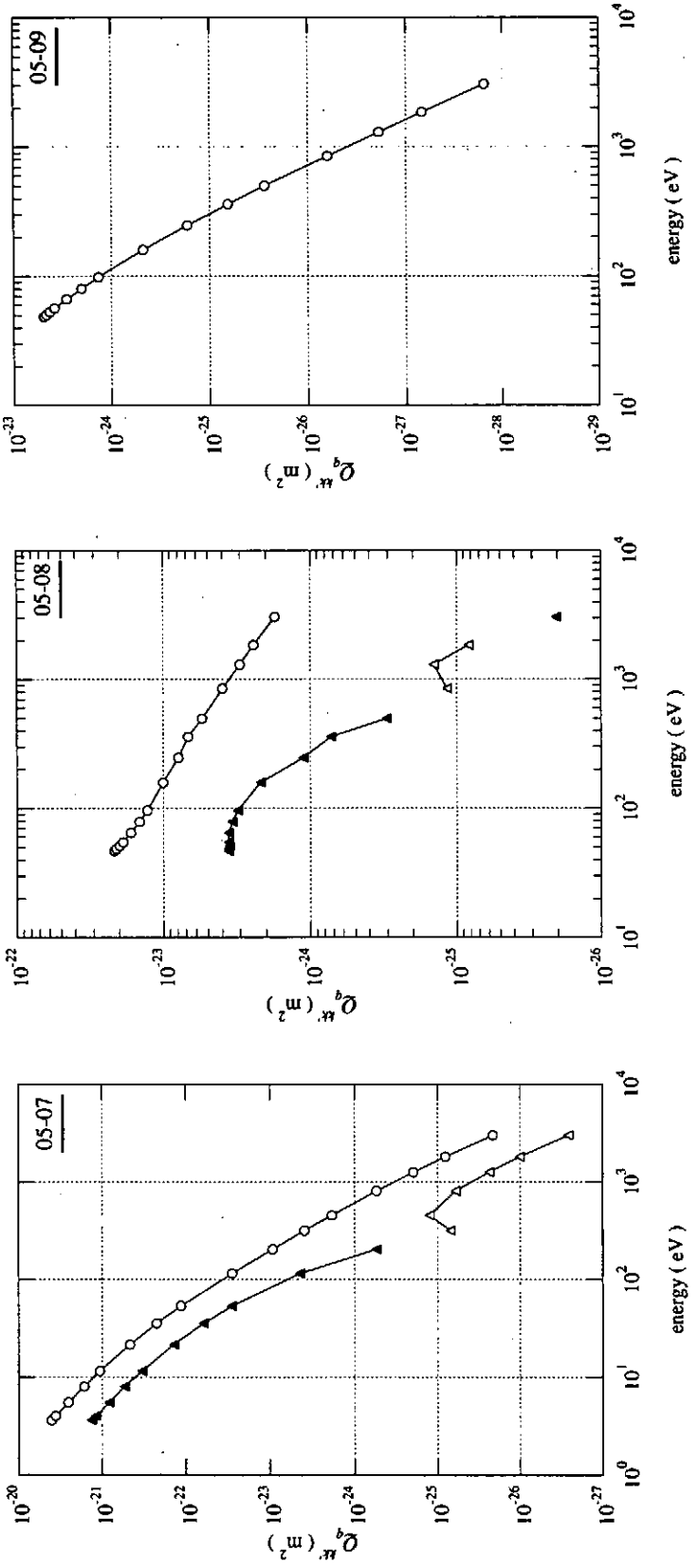

FIG. 16: Excitation cross sections from *5* to *7*, from *5* to *8* and from *5* to *9*.

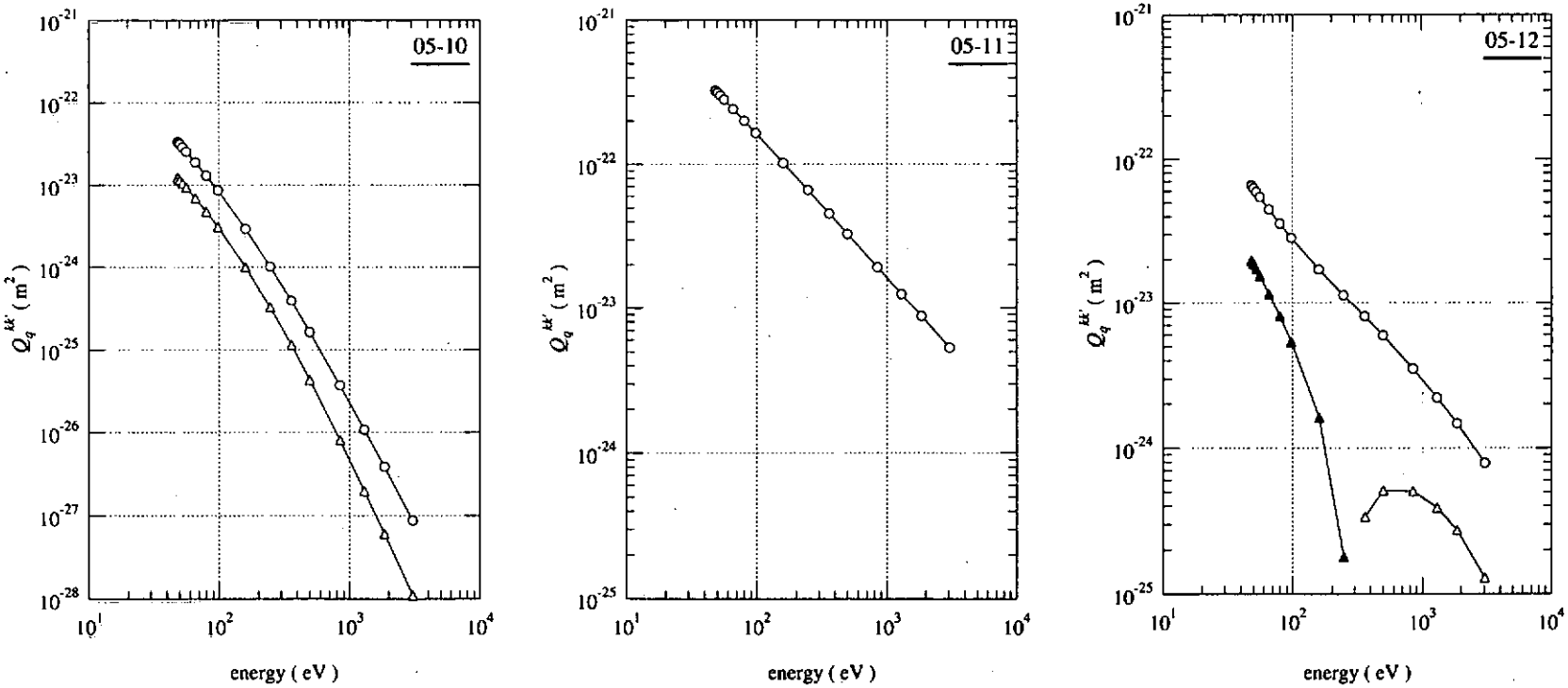

FIG. 17: Excitation cross sections from *5* to *10*, from *5* to *11* and from *5* to *12*. Q_0^{00}: open circle and Q_0^{20}: triangle. The filled triangles show that the Q_0^{20} take negative values.

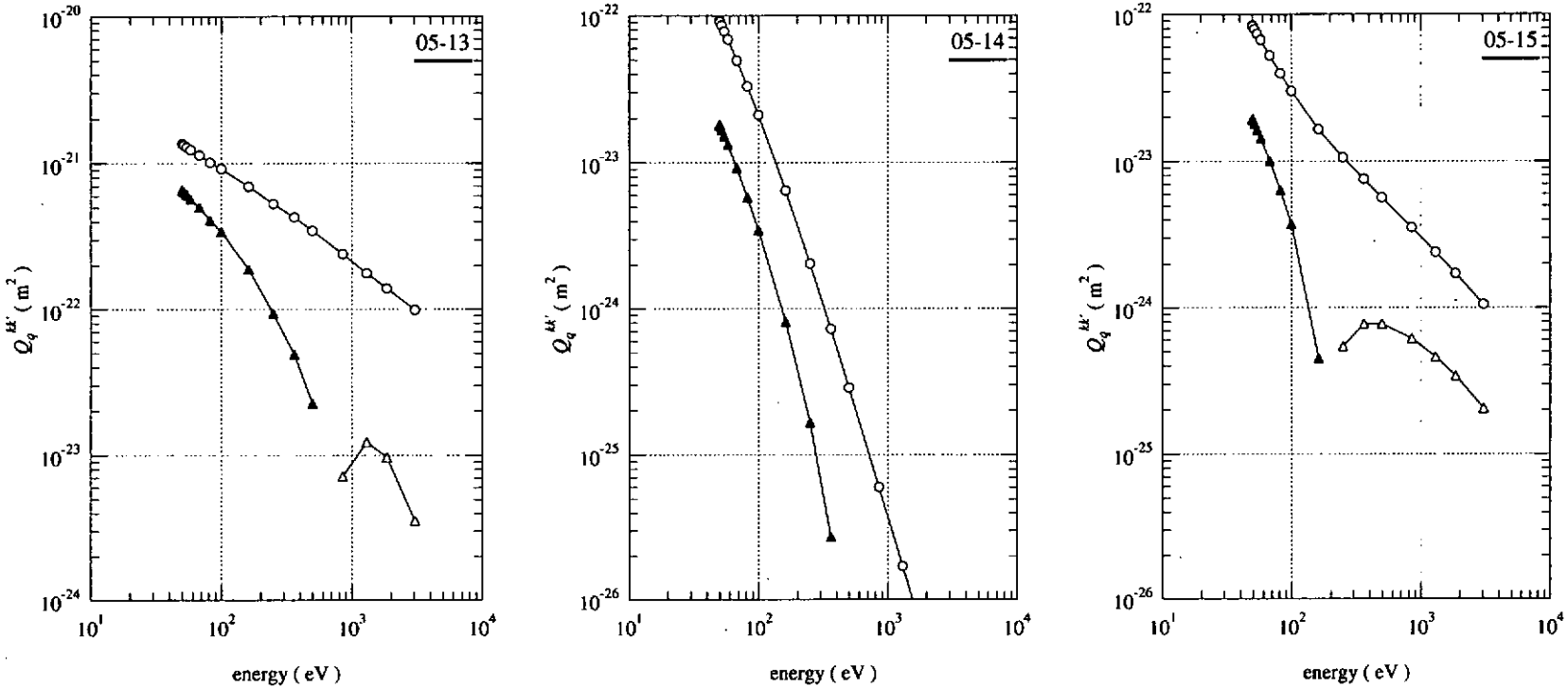

FIG. 18: Excitation cross sections from *5* to *13*, from *5* to *14* and from *5* to *15*. Q_0^{00}: open circle and Q_0^{20}: triangle. The filled triangles show that the Q_0^{20} take negative values.

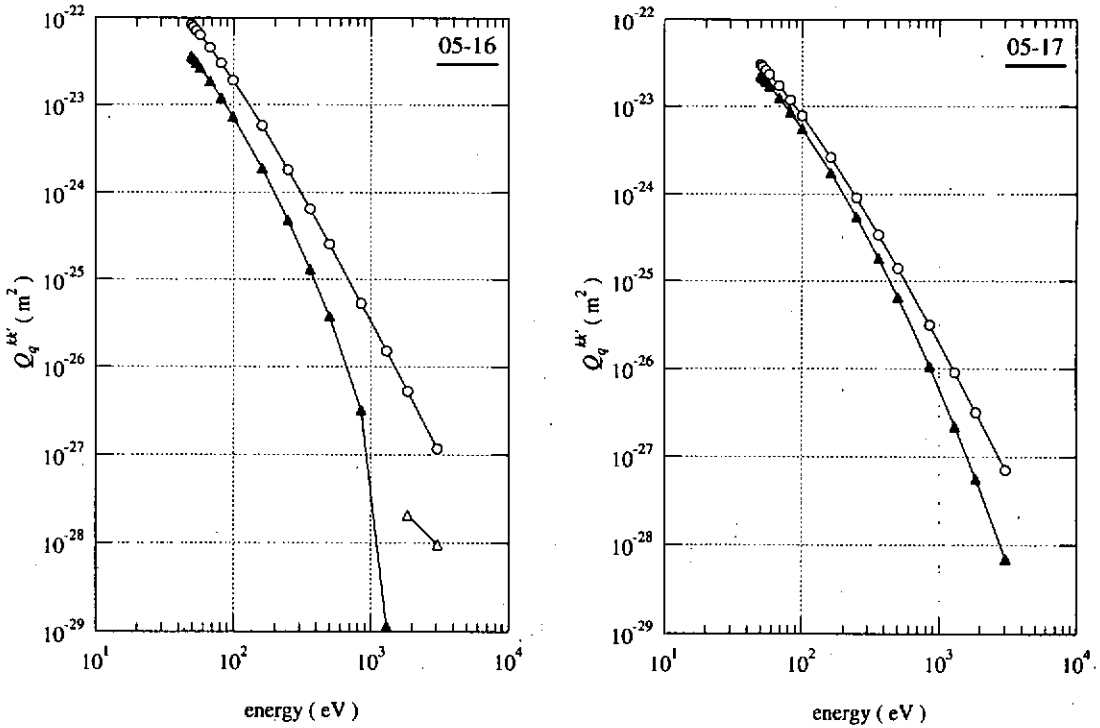

FIG. 19: Excitation cross sections from *5* to *16* and from *5* to *17*. Q_0^{00}: open circle and Q_0^{20}: triangle. The filled triangles show that the Q_0^{20} take negative values.

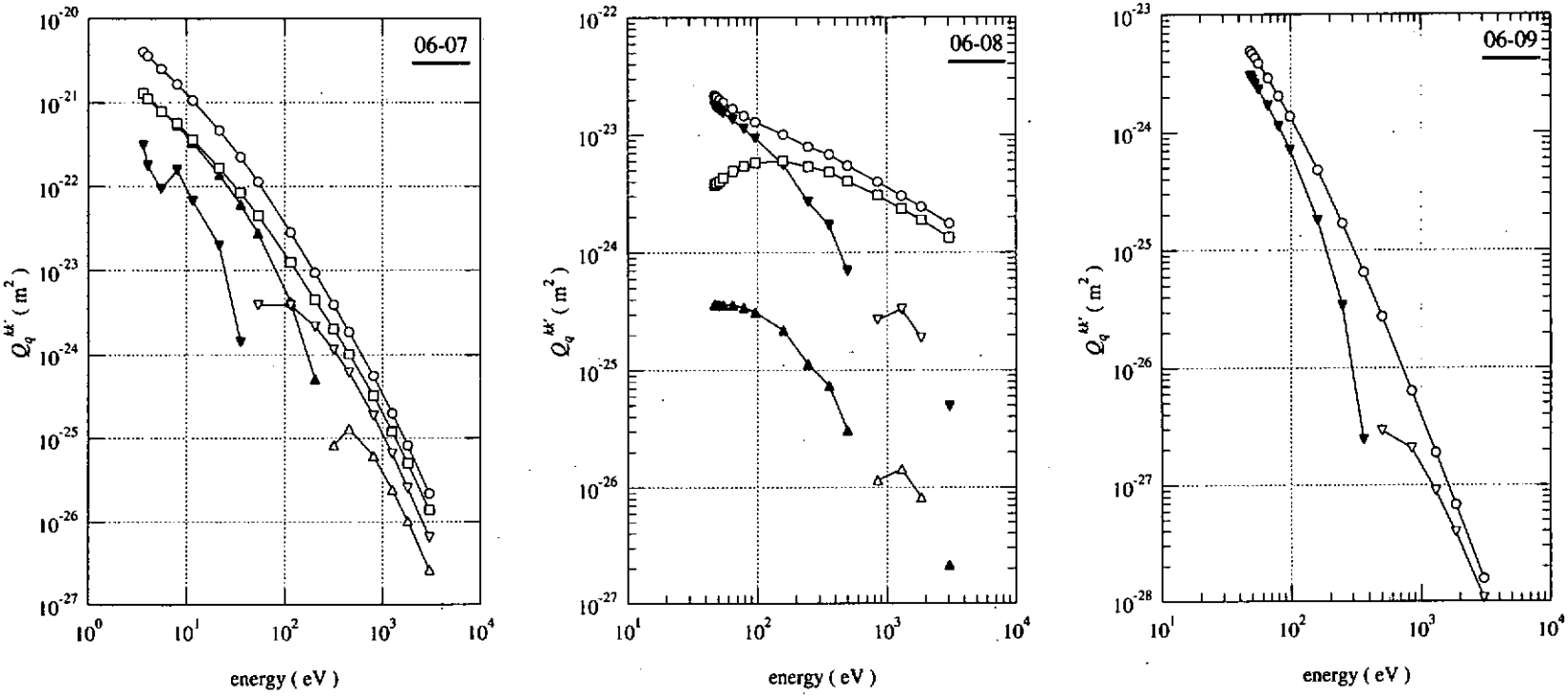

FIG. 20: Excitation cross sections from *6* to *7*, from *6* to *8* and from *6* to *9*. Q_0^{00}: open circle, Q_0^{20}: triangle, Q_0^{02}: inverted triangle and Q_0^{22}: square. The filled marks show that cross sections take negative values.

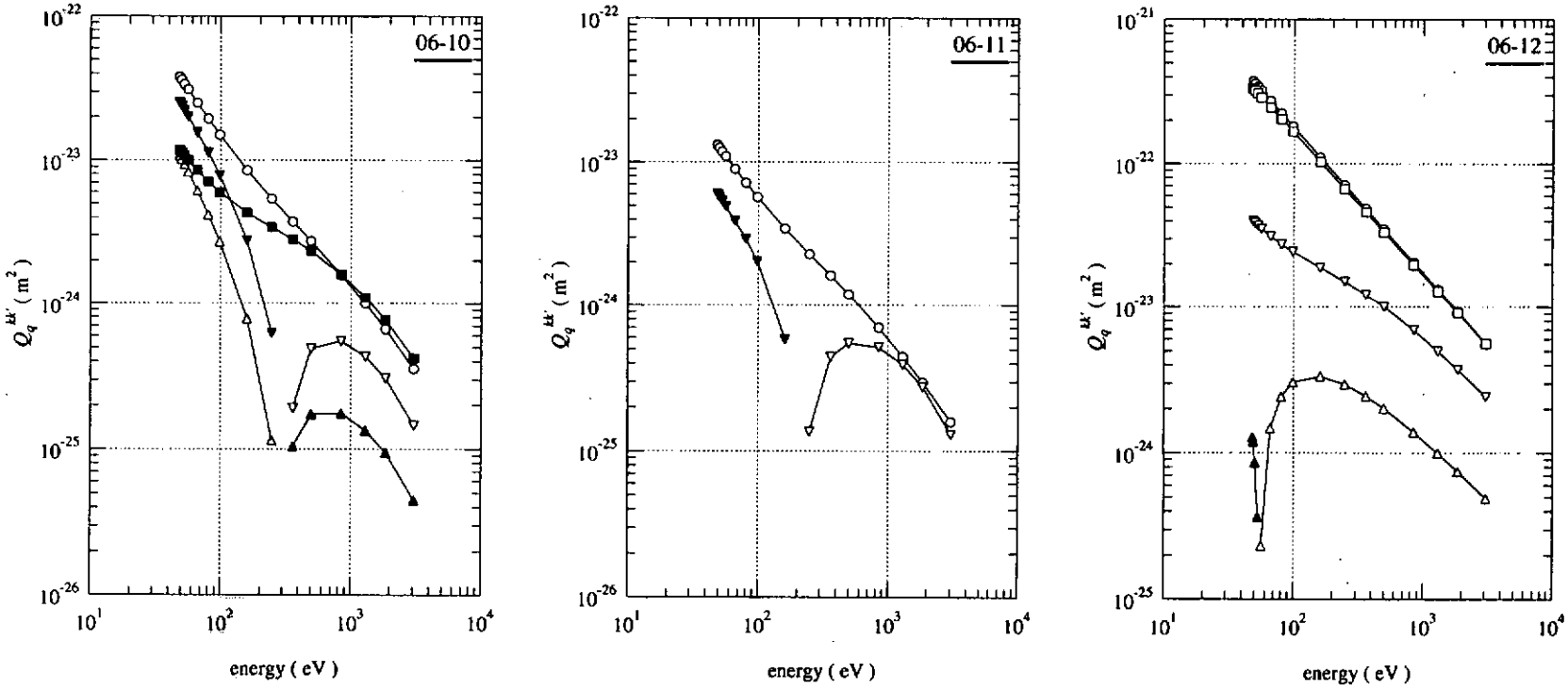

FIG. 21: Excitation cross sections from *6* to *10*, from *6* to *11* and from *6* to *12*. Q_0^{00}: open circle, Q_0^{20}: triangle, Q_0^{02}: inverted triangle and Q_0^{22}: square. The filled marks show that cross sections take negative values.

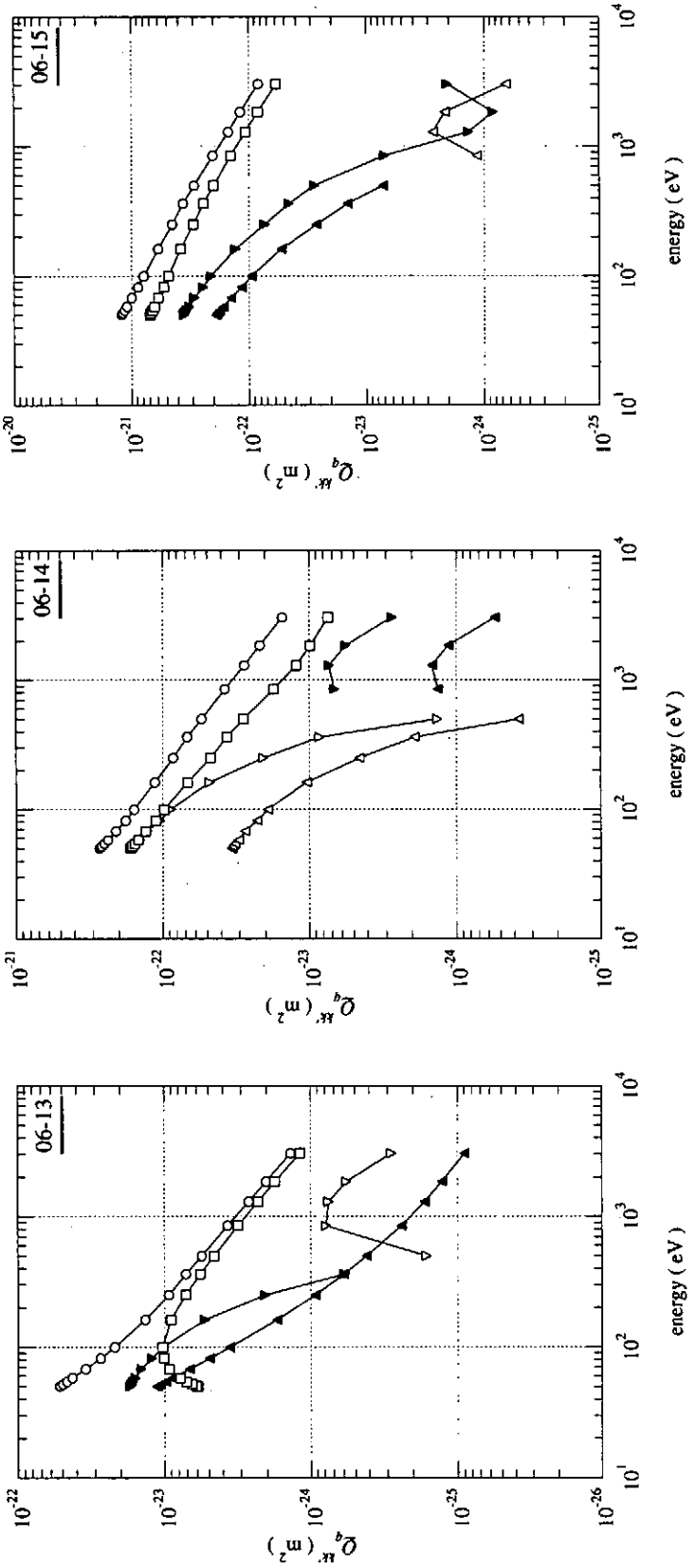

FIG. 22: Excitation cross sections from *6* to *13*, from *6* to *14* and from *6* to *14*. Q_0^{00}: open circle, Q_0^{20}: triangle, Q_0^{02}: inverted triangle and Q_0^{22}: square. The filled marks show that cross sections take negative values.

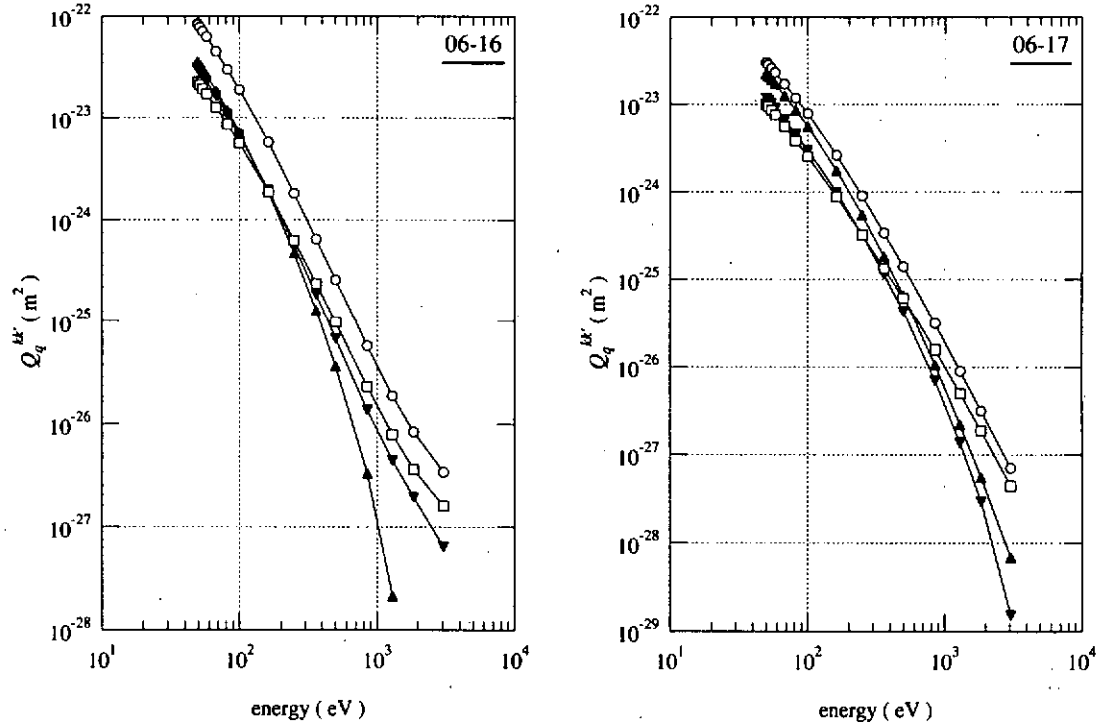

FIG. 23: Excitation cross sections from *6* to *16* and from *6* to *17*. Q_0^{00}: open circle, Q_0^{20}: triangle, Q_0^{02}: inverted triangle and Q_0^{22}: square. The filled marks show that cross sections take negative values.

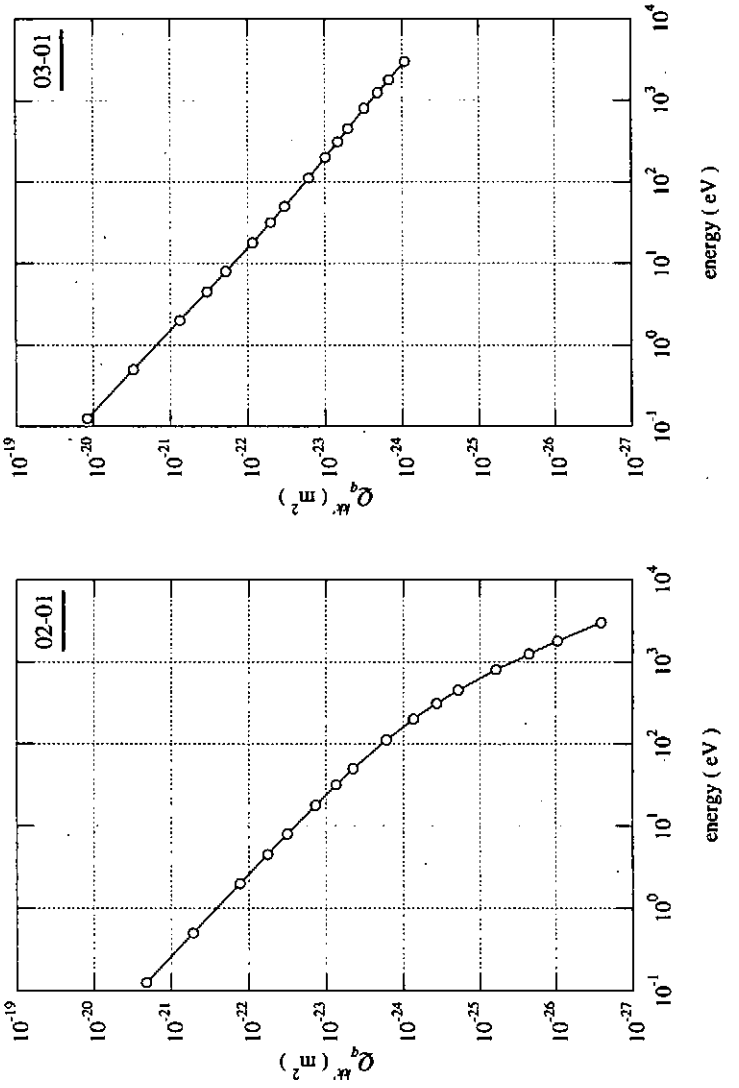

FIG. 24: Deexcitation cross sections from *2* to *1* and from *3* to *1*. Q_0^{00}: open circle.

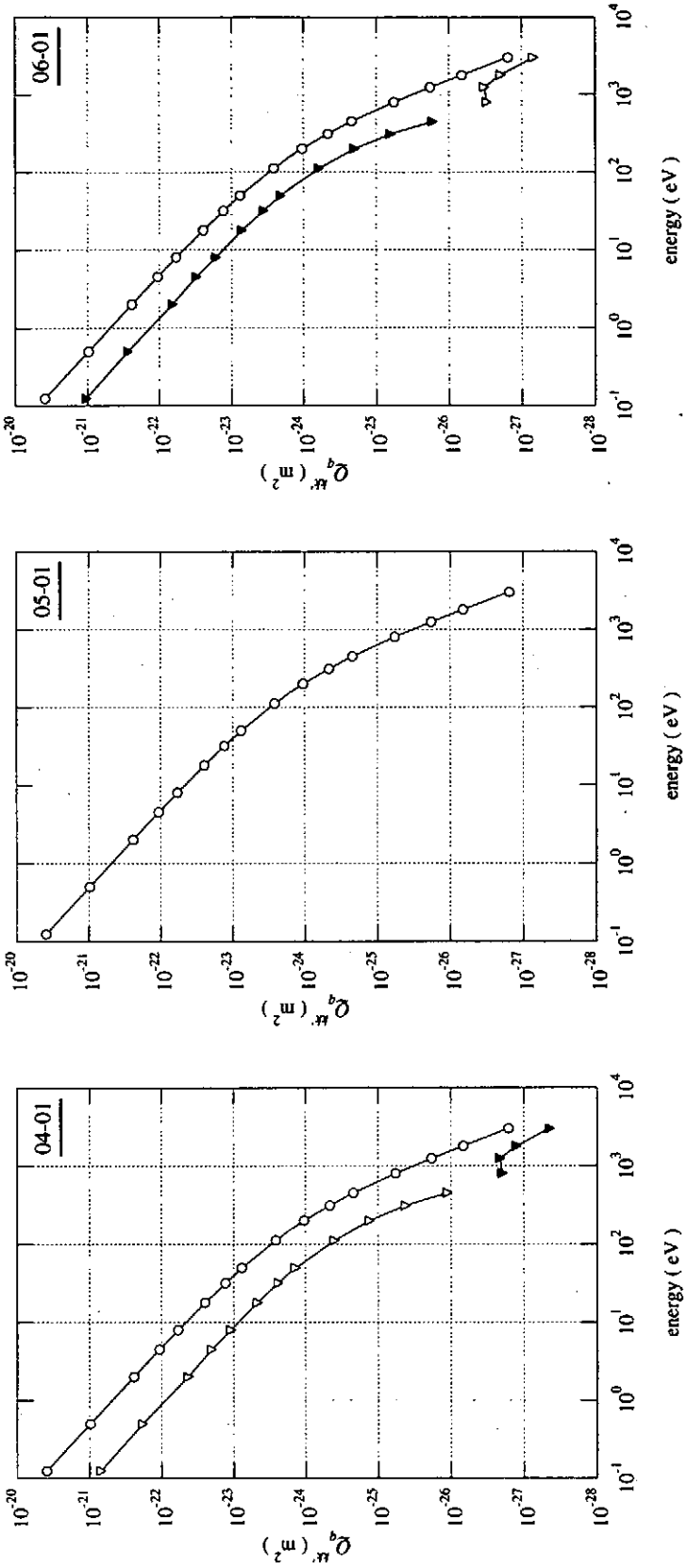

FIG. 25: Deexcitation cross sections from *4* to *1*, from *5* to *1* and from *6* to *1*.

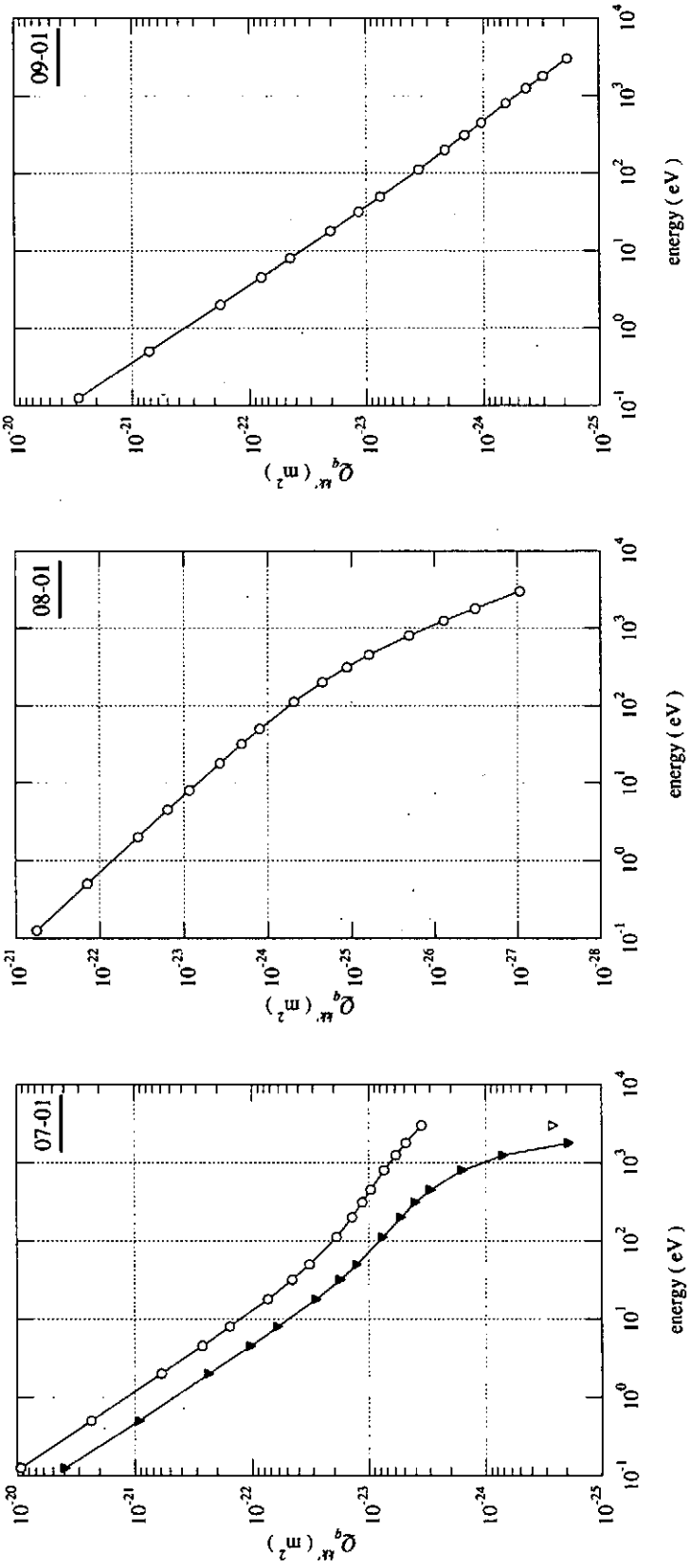

FIG. 26: Deexcitation cross sections Q_0^{00}:open circle and Q_0^{02}:cross from *7* to *1*, from *8* to *1* and from *9* to *1*.

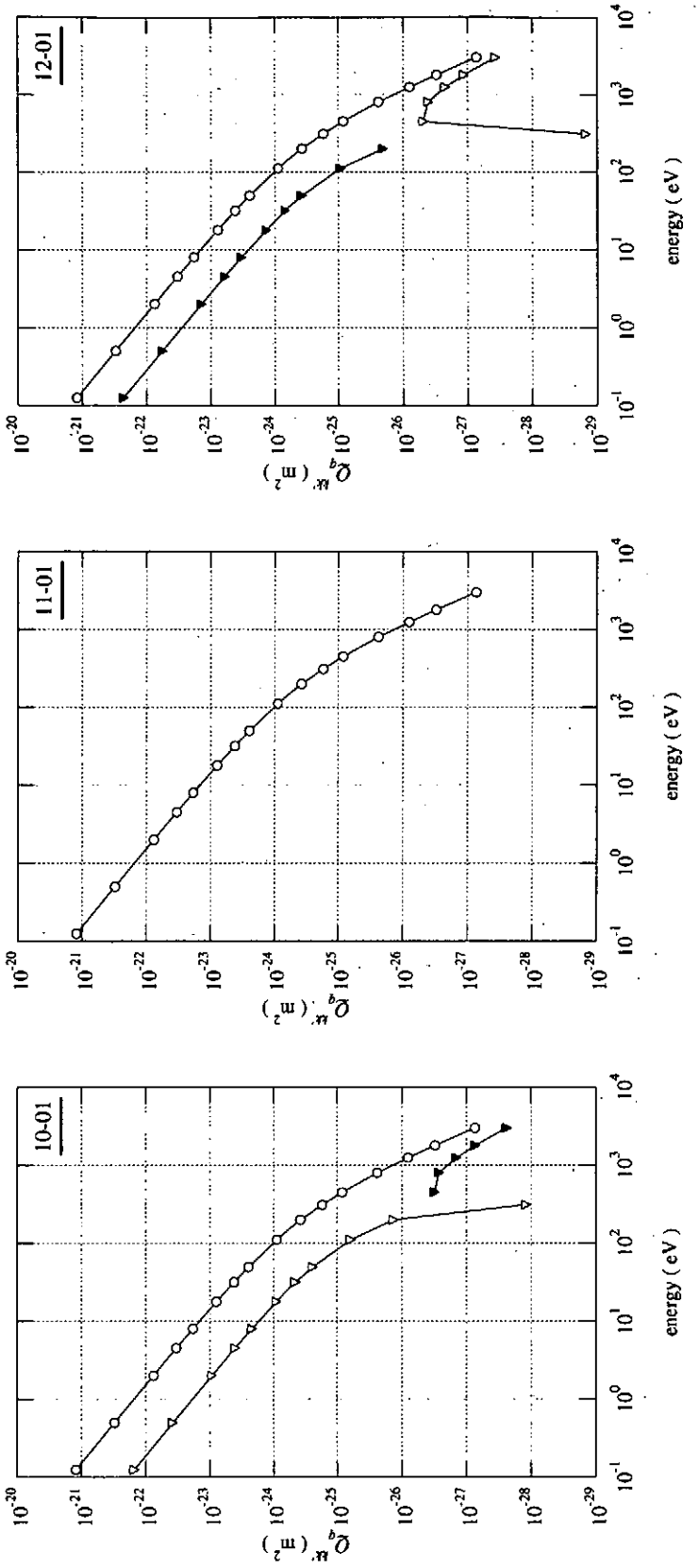

FIG. 27: Deexcitation cross sections Q_0^{00}:open circle and Q_0^{02}:cross from *10* to *1*, from *11* to *1* and from *12* to *1*.

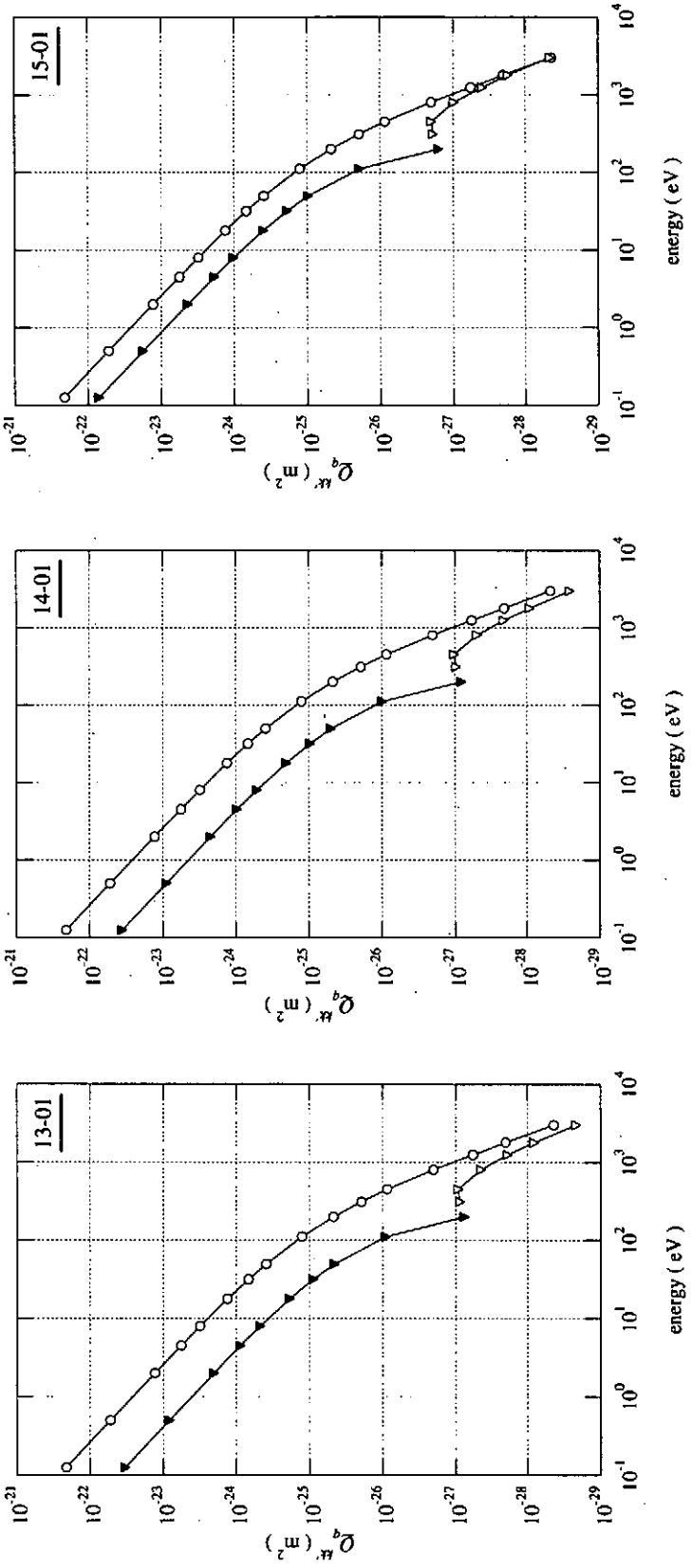

FIG. 28: Deexcitation cross sections Q_0^{00}:open circle and Q_0^{02}:cross from *13* to *1*, from *14* to *1* and from *15* to *1*.

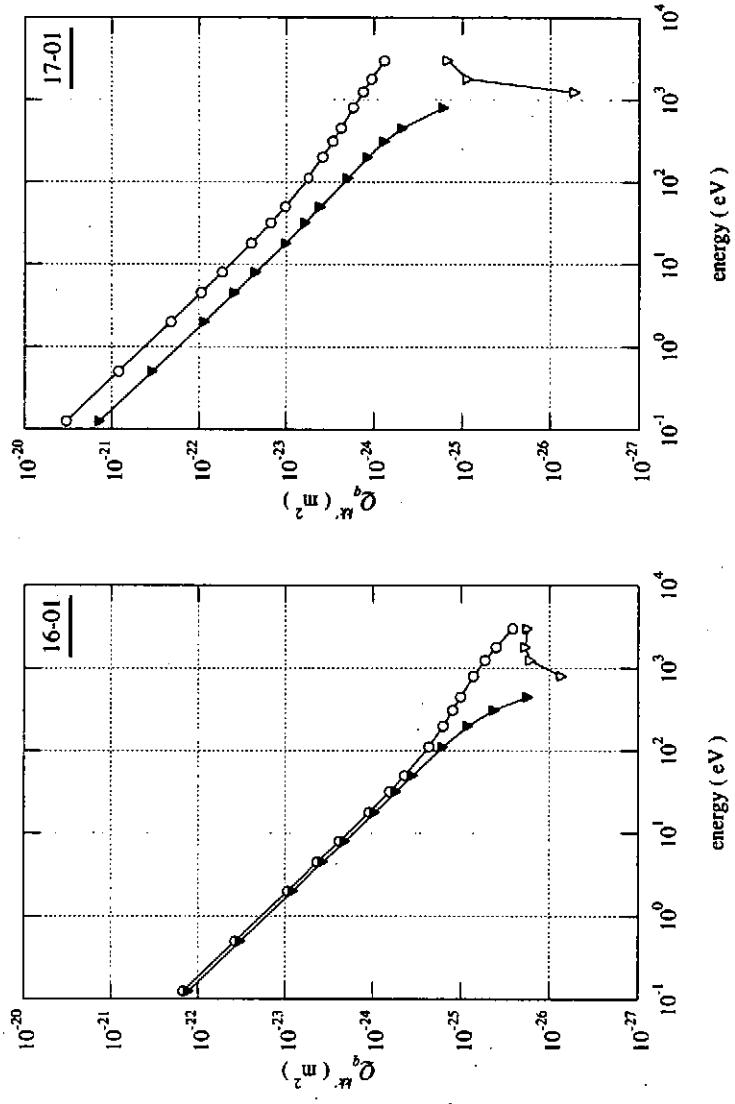

FIG. 29: Deexcitation cross sections Q_0^{00}:open circle and Q_0^{02}:cross from *16* to *1* and from *17* to *1*.

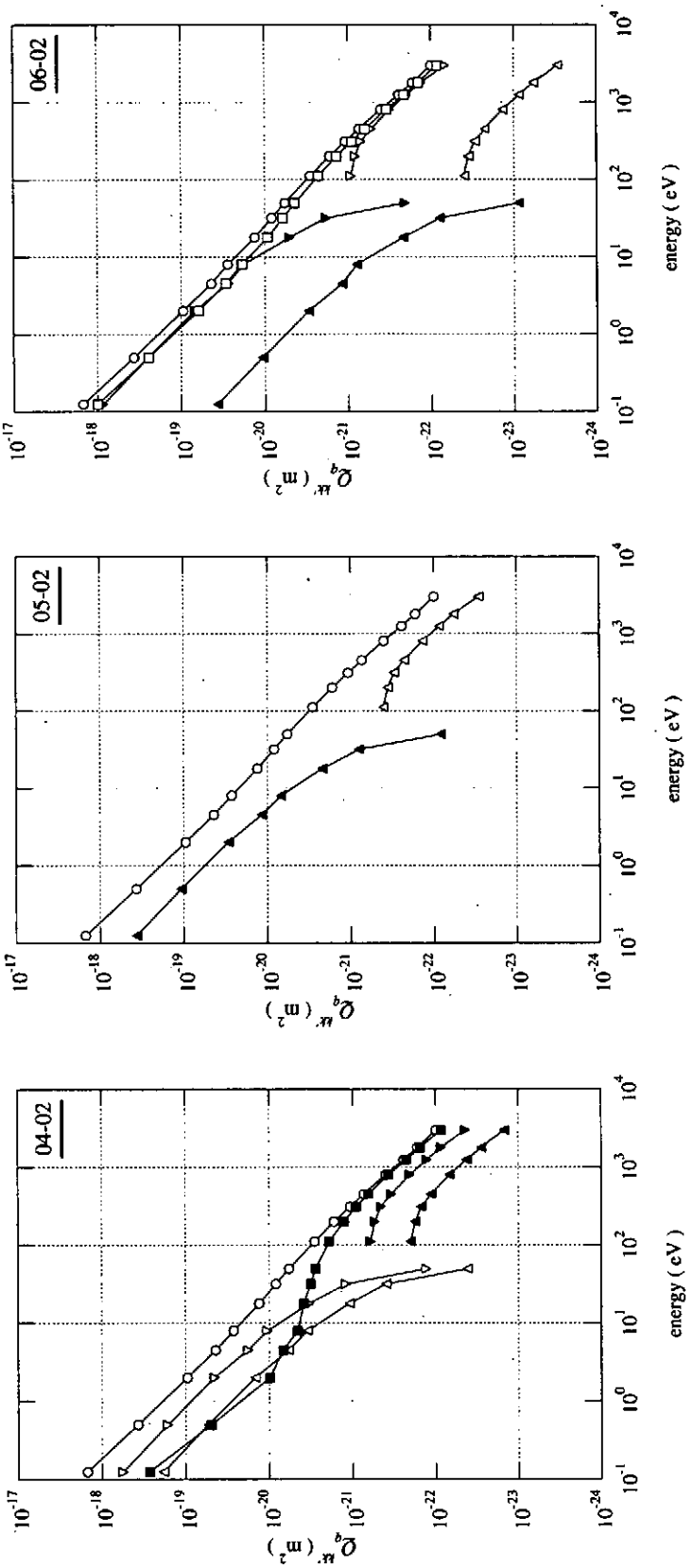

FIG. 30: Deexcitation cross sections Q_0^{00}:open circle, Q_0^{20}:filled circle, Q_0^{02}:cross and Q_0^{22}:plus from *4* to *2*, from *5* to *2* and from *6* to *2*.

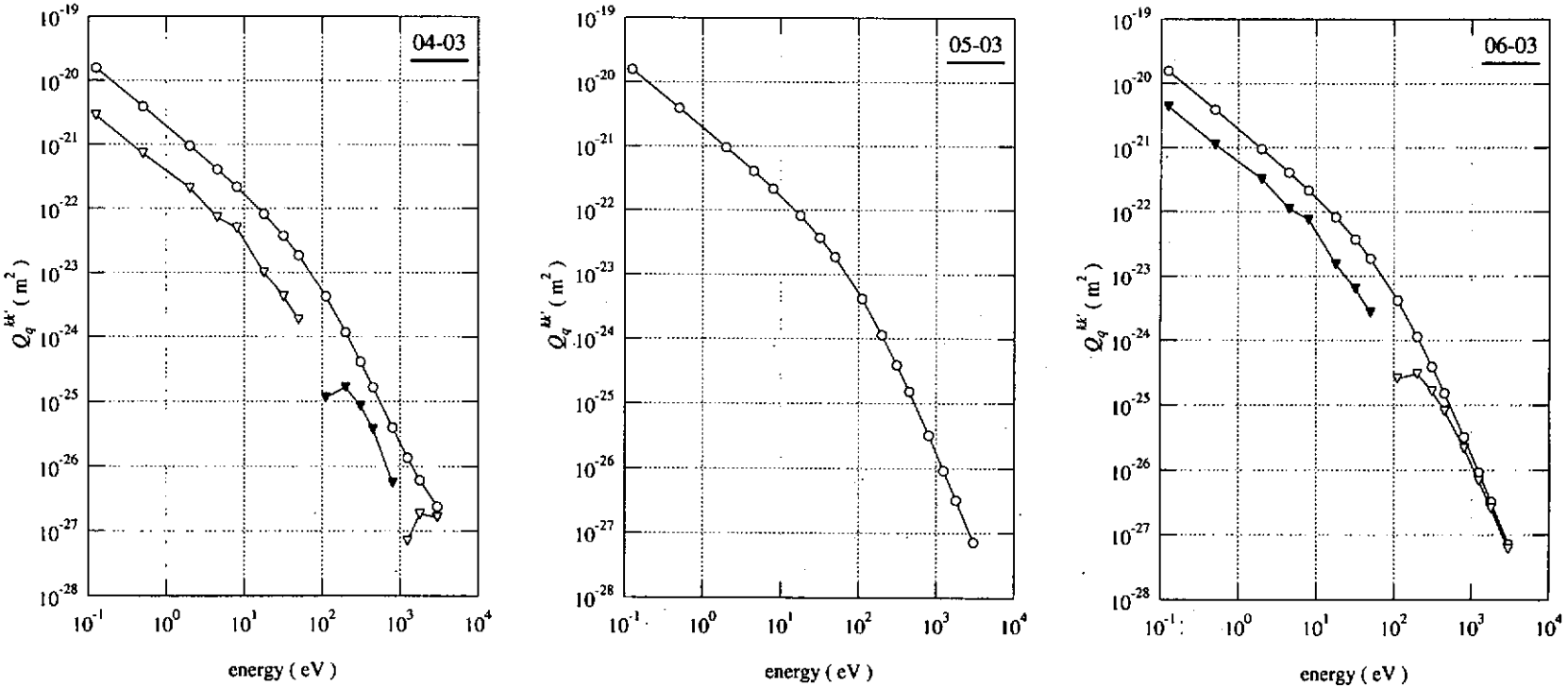

FIG. 31: Deexcitation cross sections Q_0^{00}:open circle and Q_0^{02}:cross from *4* to *2*, from *5* to *2* and from *6* to *2*.

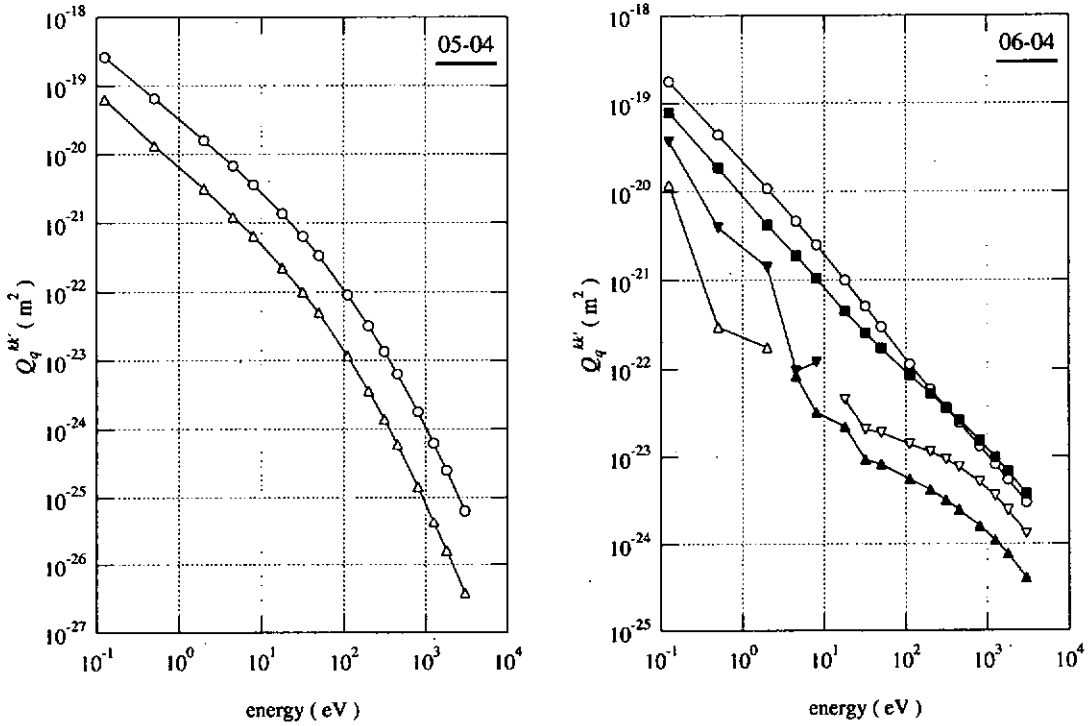

FIG. 32: Deexcitation cross sections Q_0^{00}:open circle, Q_0^{20}:filled circle, Q_0^{02}:cross and Q_0^{22}:plus from *5* to *4*, from *6* to *4* and from *6* to *5*.

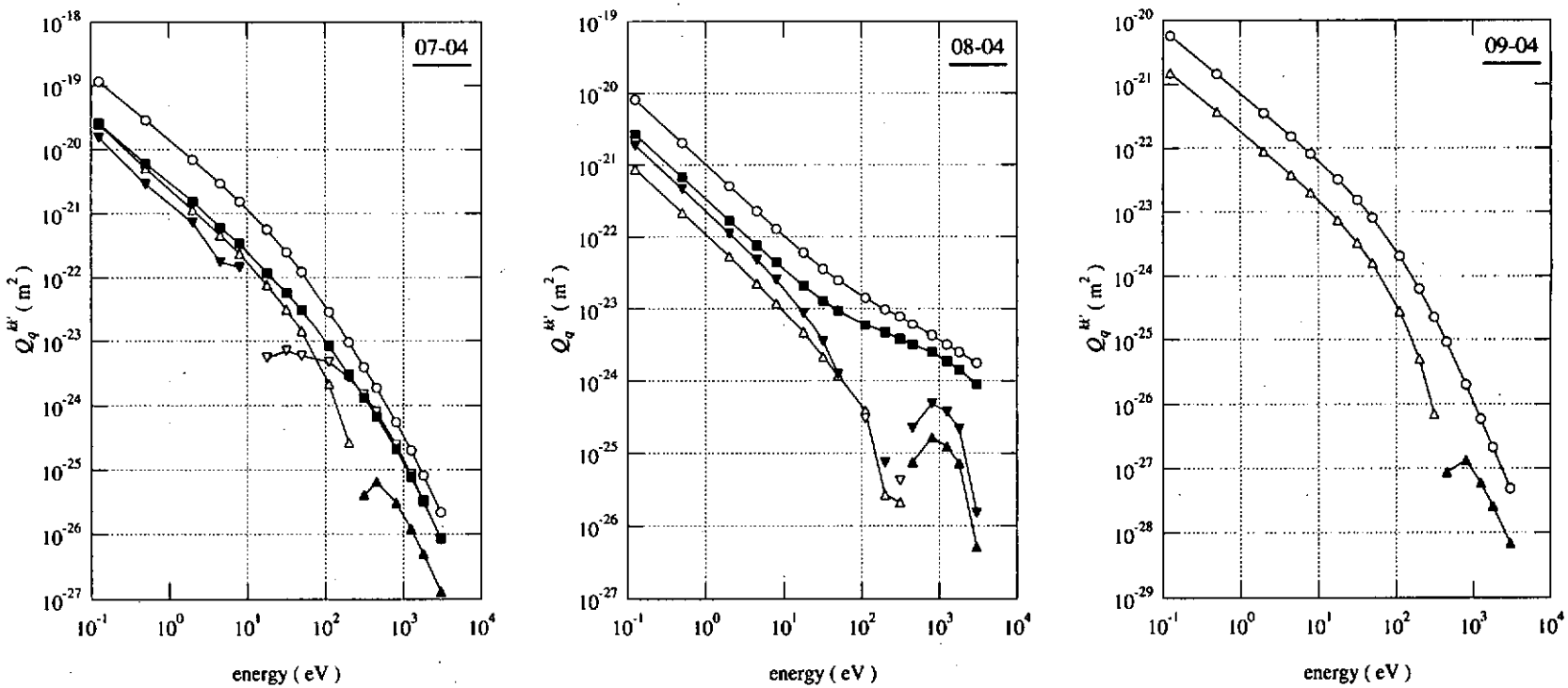

FIG. 33: Dexcitation cross sections from *7* to *4*, from *8* to *4* and from *9* to *4*. Q_0^{00}: open circle, Q_0^{20}: triangle, Q_0^{02}: inverted triangle and Q_0^{22}: square. The filled marks show that cross sections take negative values.

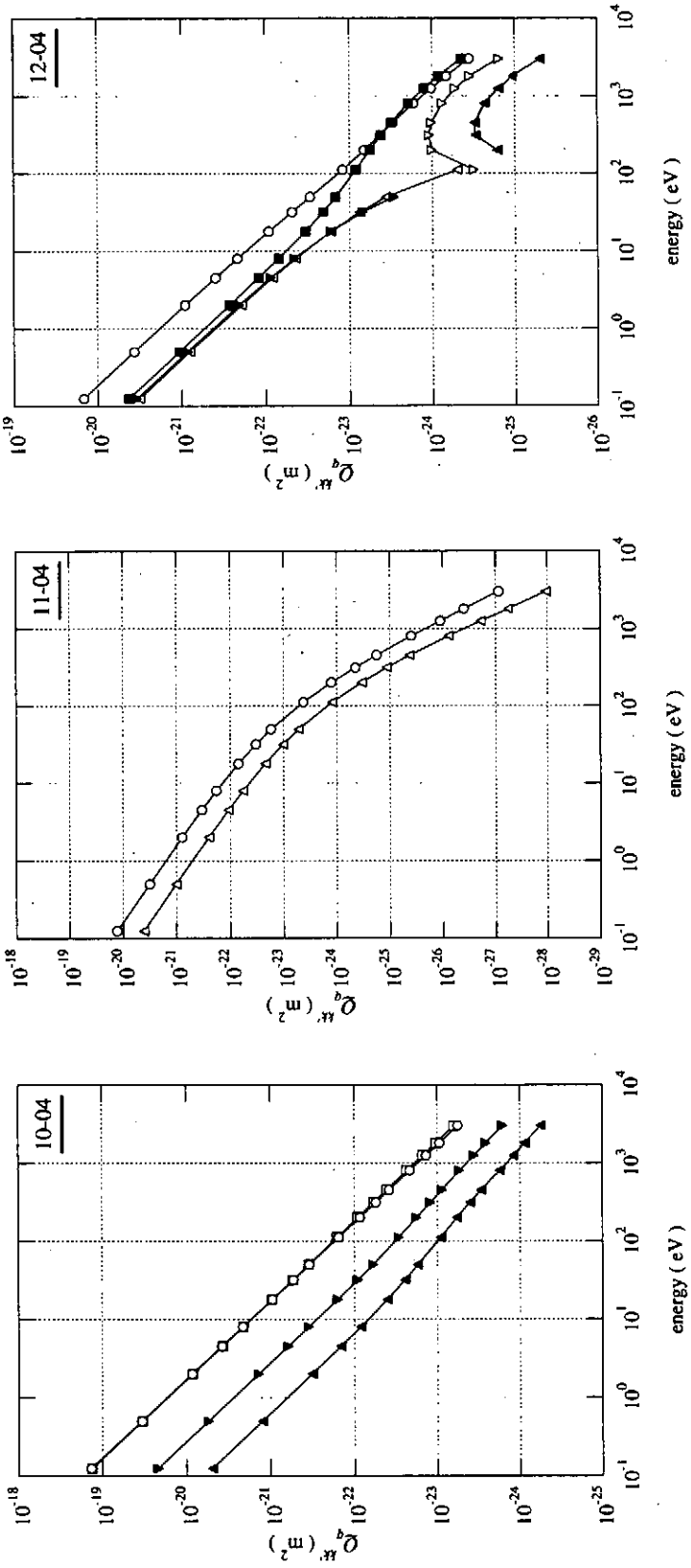

FIG. 34: Excitation cross sections from *10* to *4*, from *11* to *4* and from *12* to *4*. Q_0^{00}: open circle, Q_0^{20}: triangle, Q_0^{02}: inverted triangle and Q_0^{22}: square. The filled marks show that cross sections take negative values.

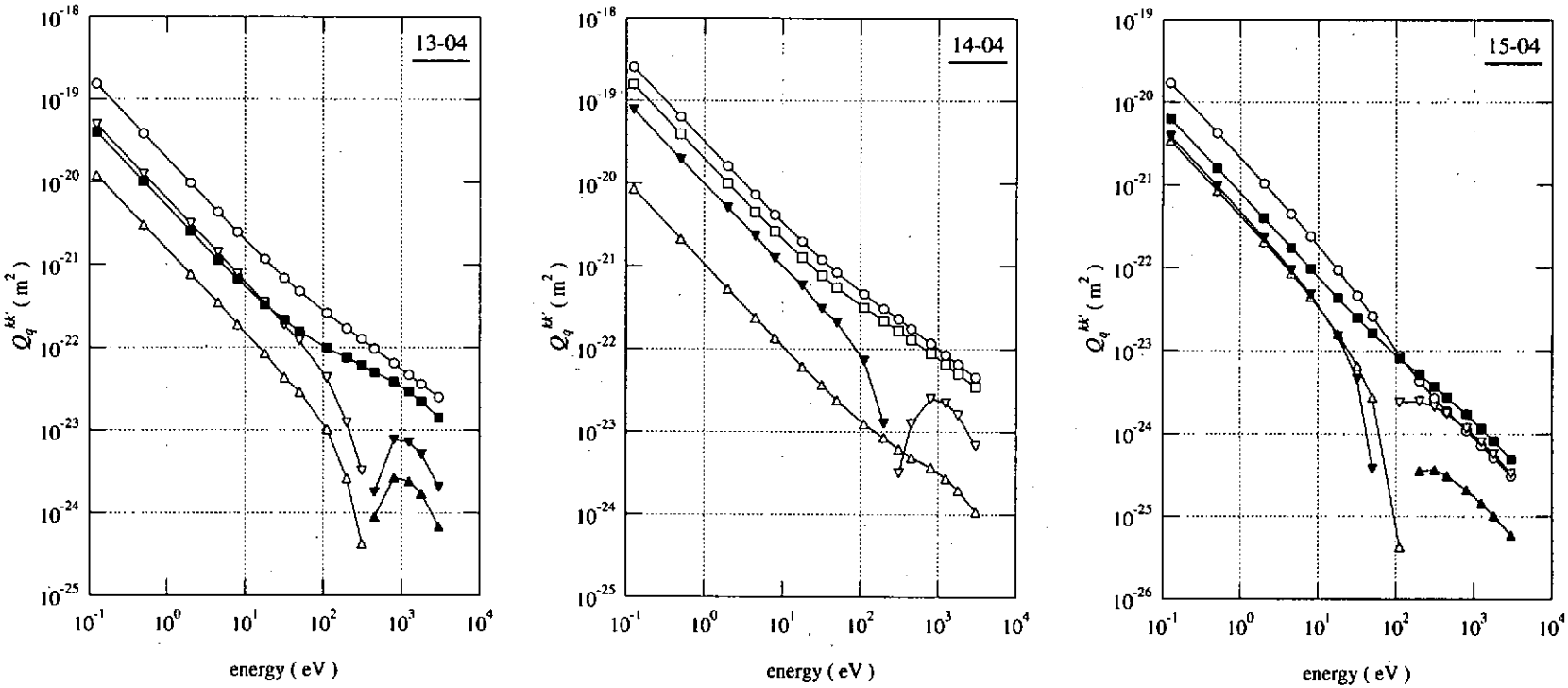

FIG. 35: Excitation cross sections from *13* to *4*, from *14* to *4* and from *15* to *4*. Q_0^{00}: open circle, Q_0^{20}: triangle, Q_0^{02}: inverted triangle and Q_0^{22}: square. The filled marks show that cross sections take negative values.

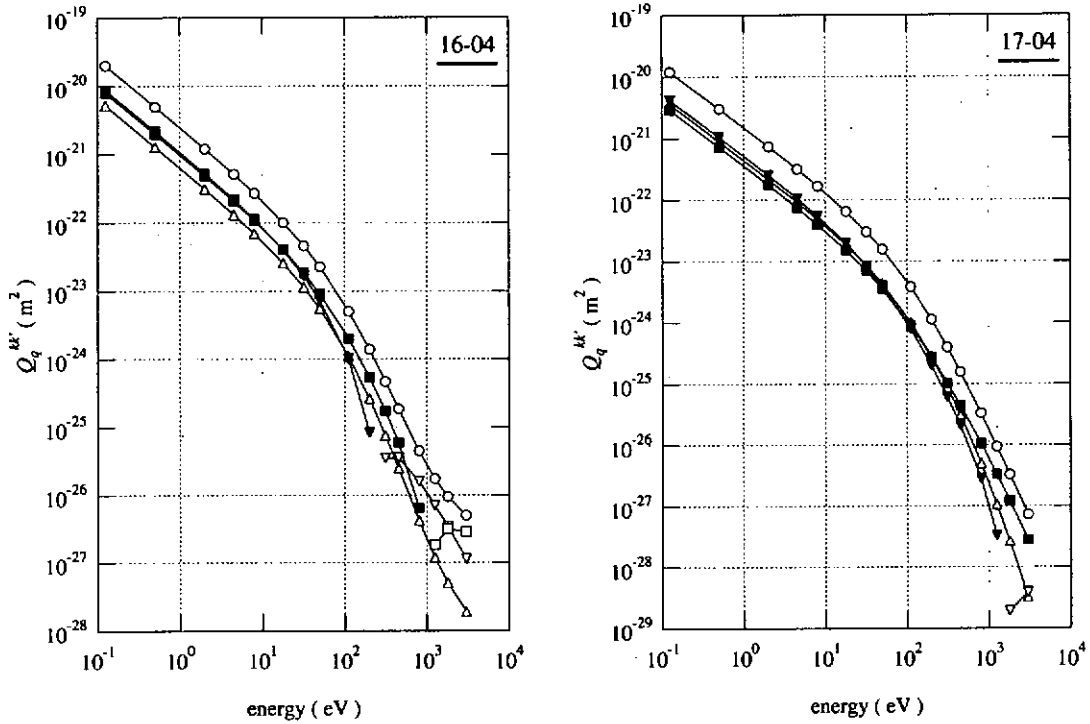

FIG. 36: Excitation cross sections from *16* to *4* and from *17* to *4*. Q_0^{00}: open circle, Q_0^{20}: triangle, Q_0^{02}: inverted triangle and Q_0^{22}: square. The filled marks show that cross sections take negative values.

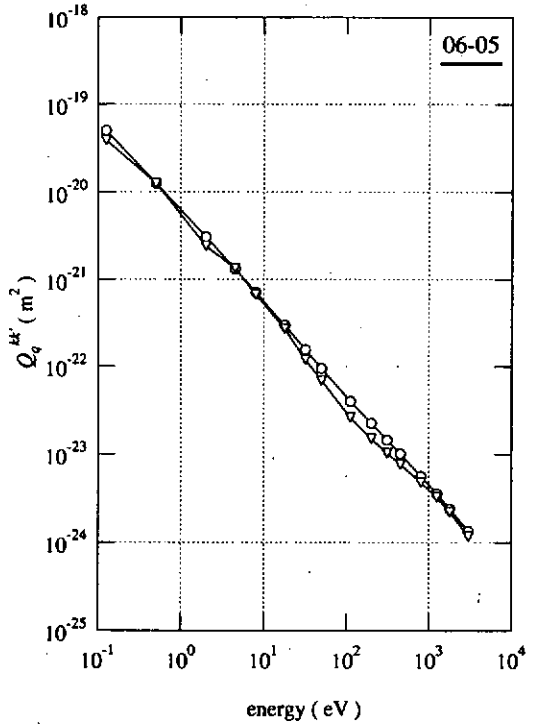

FIG. 37: Excitation cross sections from *6* to *5*. Q_0^{00}: open circle and Q_0^{20}: triangle. The filled triangles show that the Q_0^{20} take negative values.

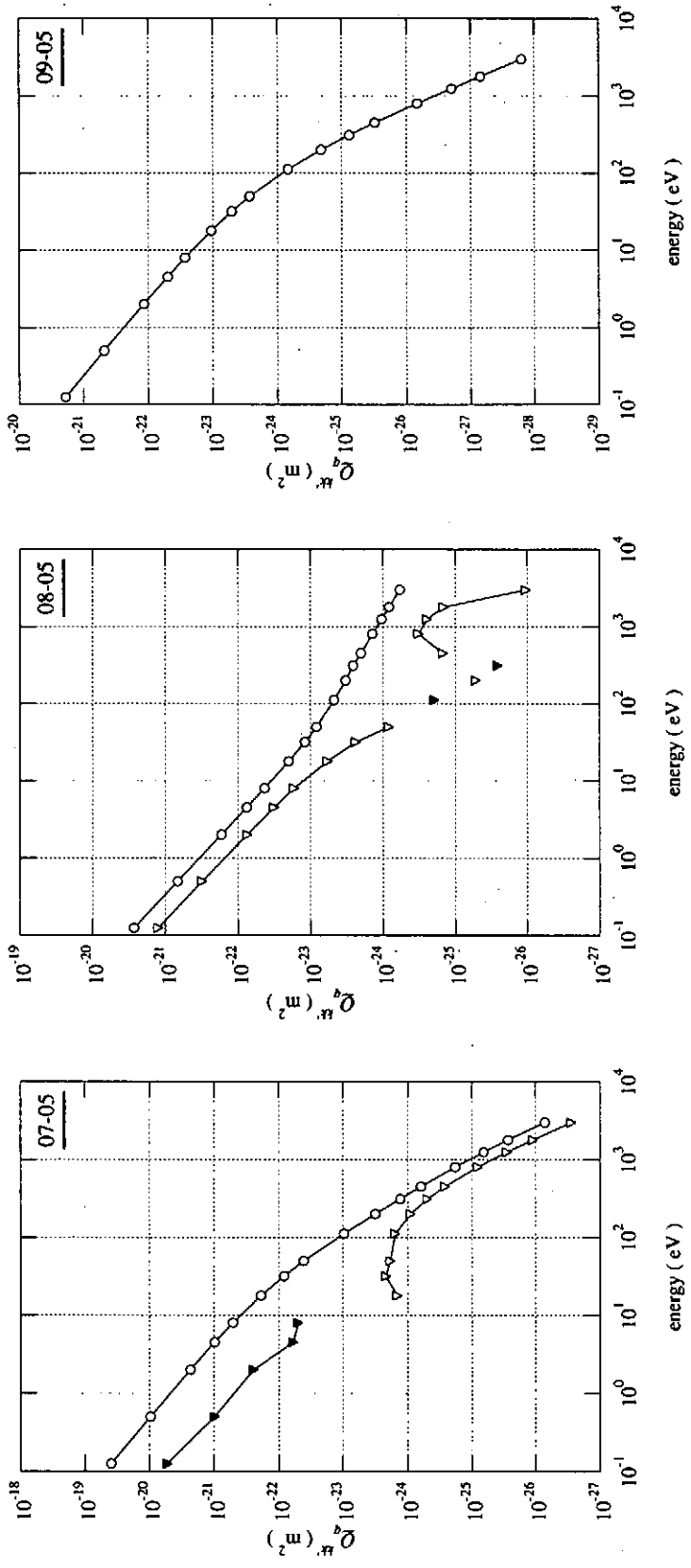

FIG. 38: Excitation cross sections from *7* to *5*, from *8* to *5* and from *9* to *5*.

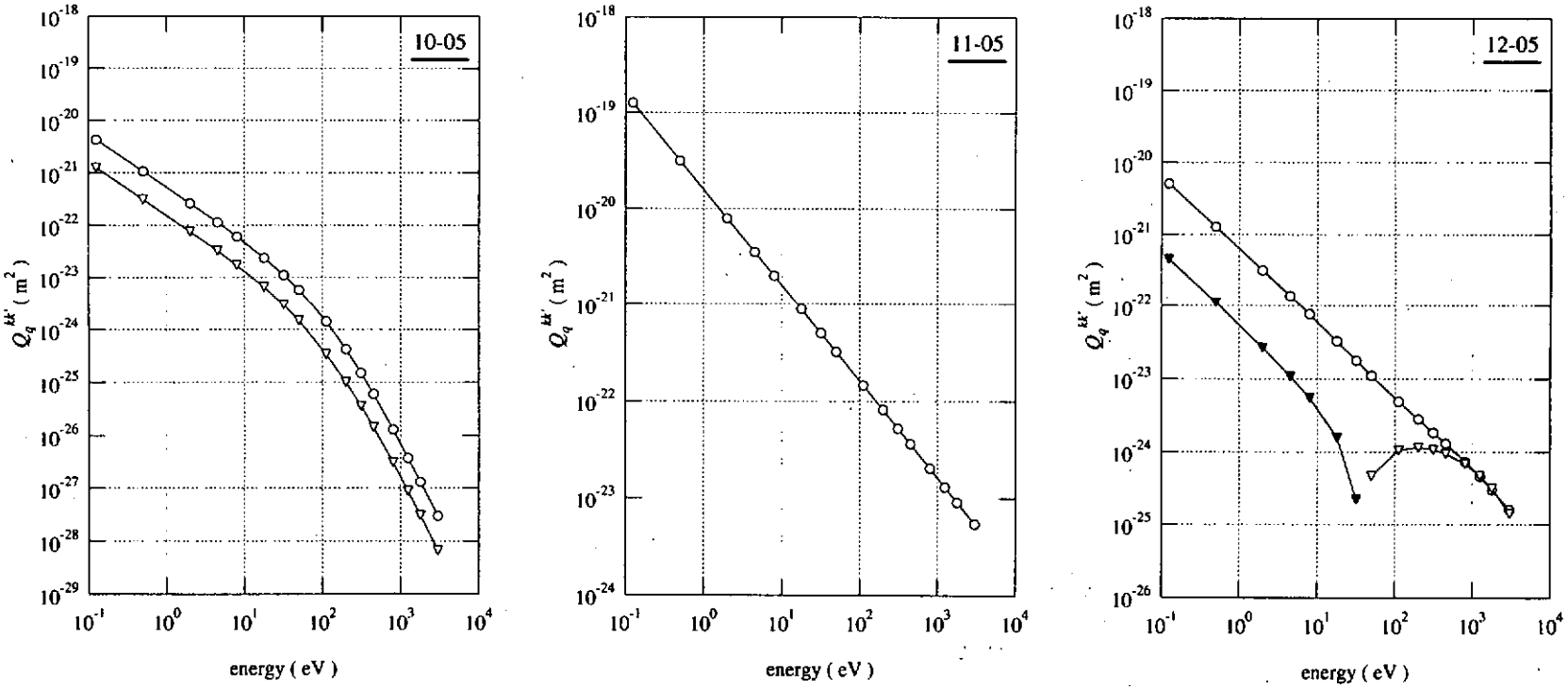

FIG. 39: Excitation cross sections from *10* to *5*, from *11* to *5* and from *12* to *5*. Q_0^{00}: open circle and Q_0^{20}: triangle. The filled triangles show that the Q_0^{20} take negative values.

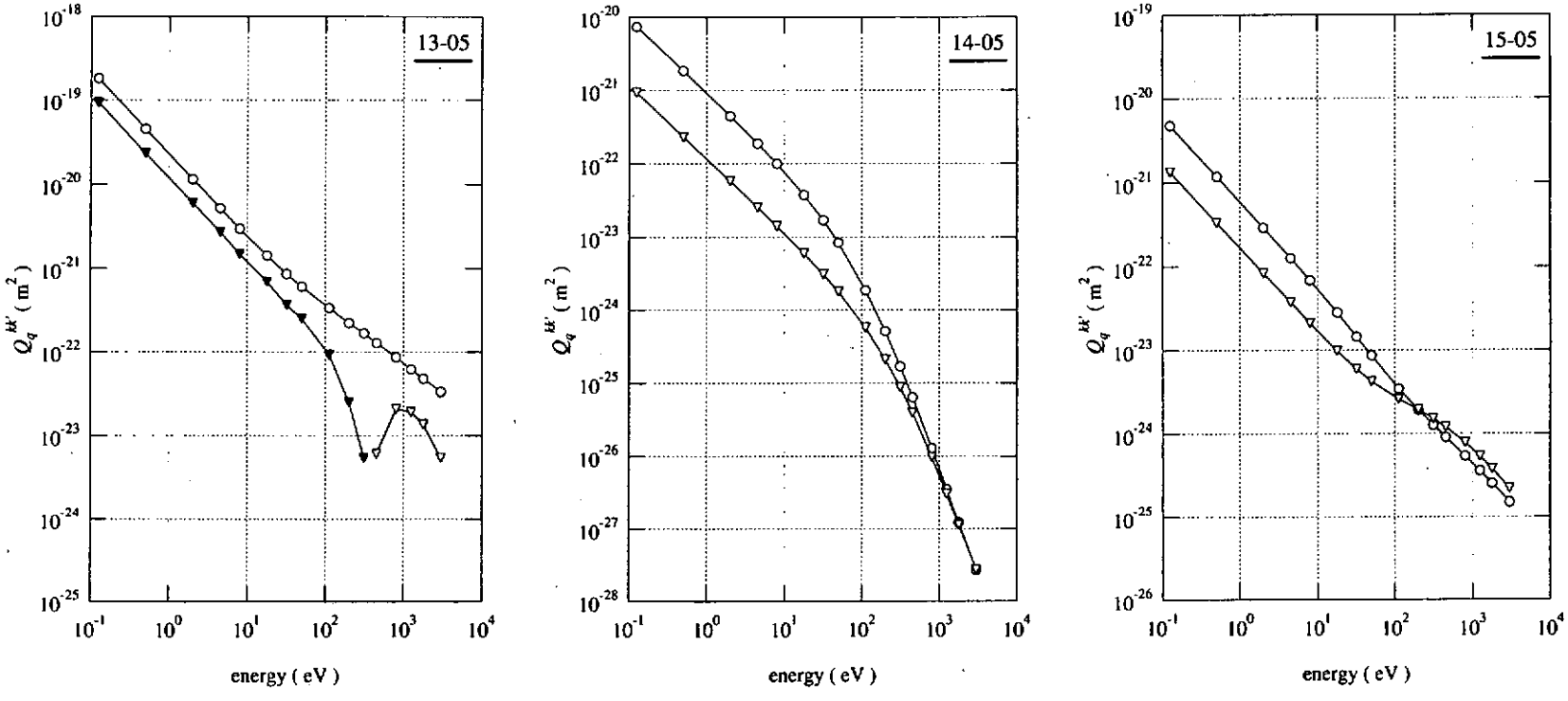

FIG. 40: Excitation cross sections from *13* to *5*, from *14* to *5* and from *15* to *5*. Q_0^{00}: open circle and Q_0^{02}: inverted triangle. The filled marks show that the Q_0^{20} take negative values.

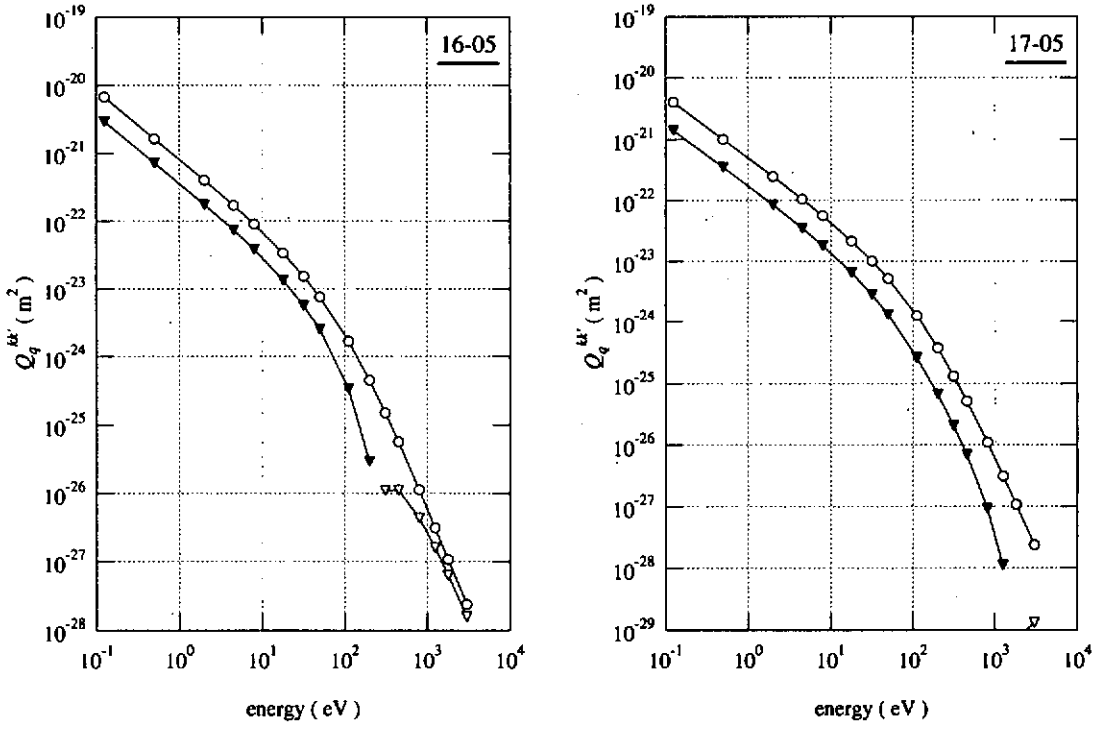

FIG. 41: Excitation cross sections from *16* to *5* and from *17* to *5*. Q_0^{00}: open circle and Q_0^{20}: triangle. The filled triangles show that the Q_0^{20} take negative values.

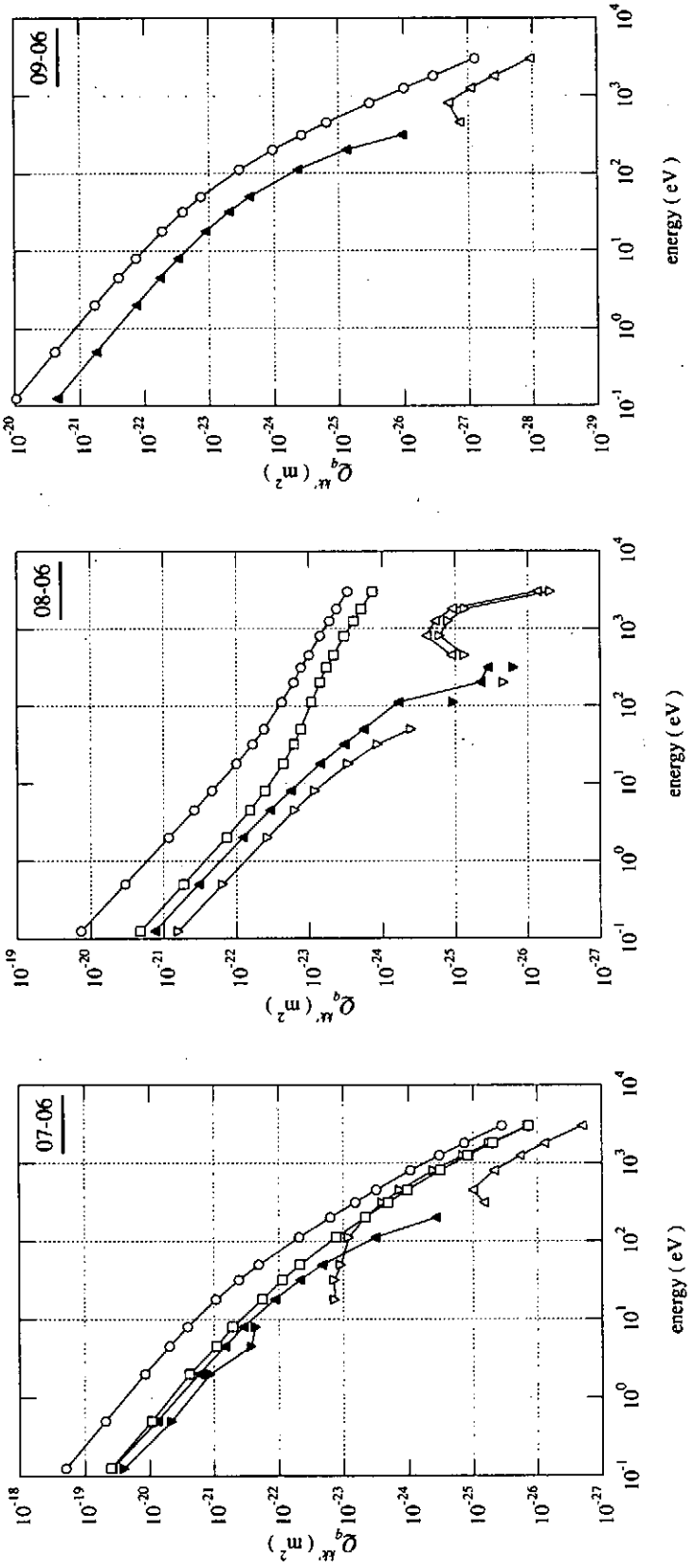

FIG. 42: Excitation cross sections from *7* to *6*, from *8* to *6* and from *9* to *6*. Q_0^{00}: open circle, Q_0^{20}: triangle, Q_0^{02}: inverted triangle and Q_0^{22}: square. The filled marks show that cross sections take negative values.

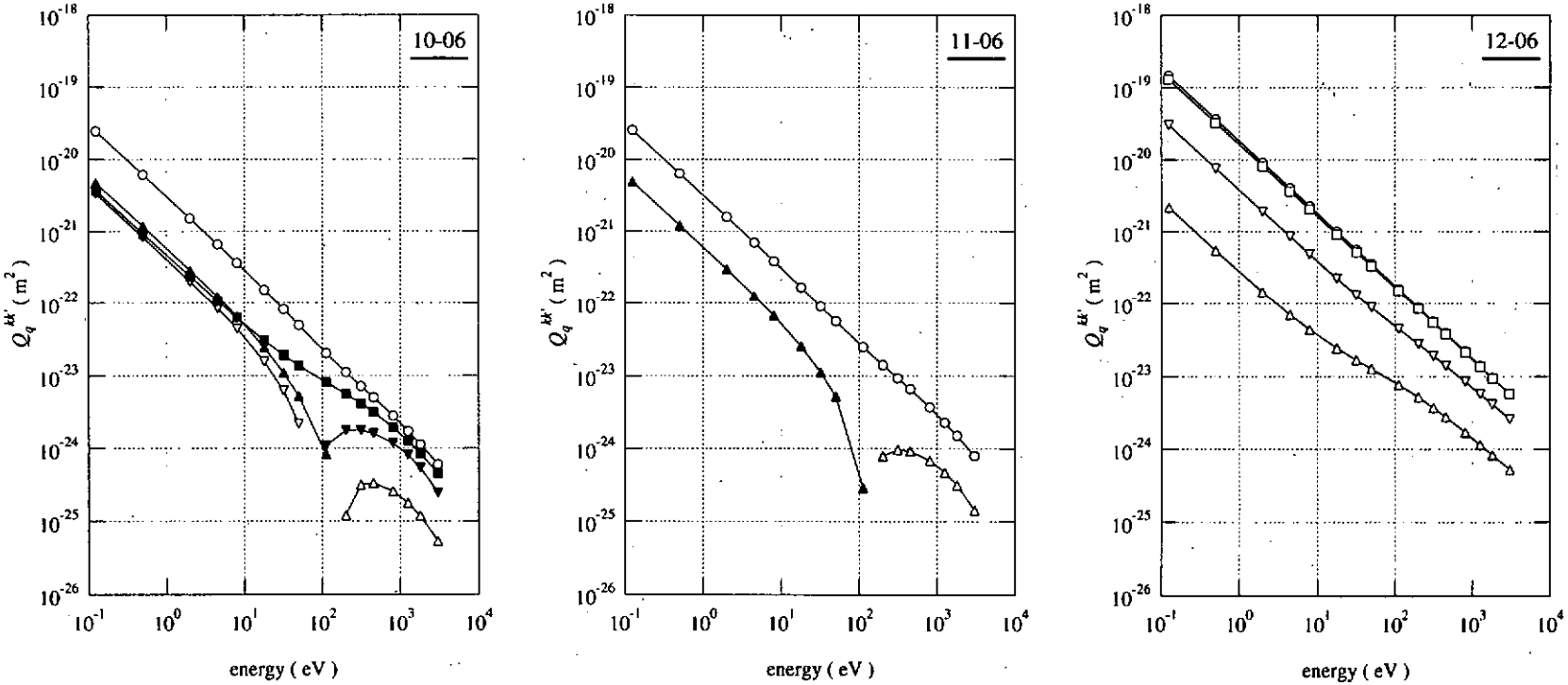

FIG. 43: Excitation cross sections from *10* to *6*, from *11* to *6* and from *12* to *6*. Q_0^{00}: open circle, Q_0^{20}: triangle, Q_0^{02}: inverted triangle and Q_0^{22}: square. The filled marks show that cross sections take negative values.

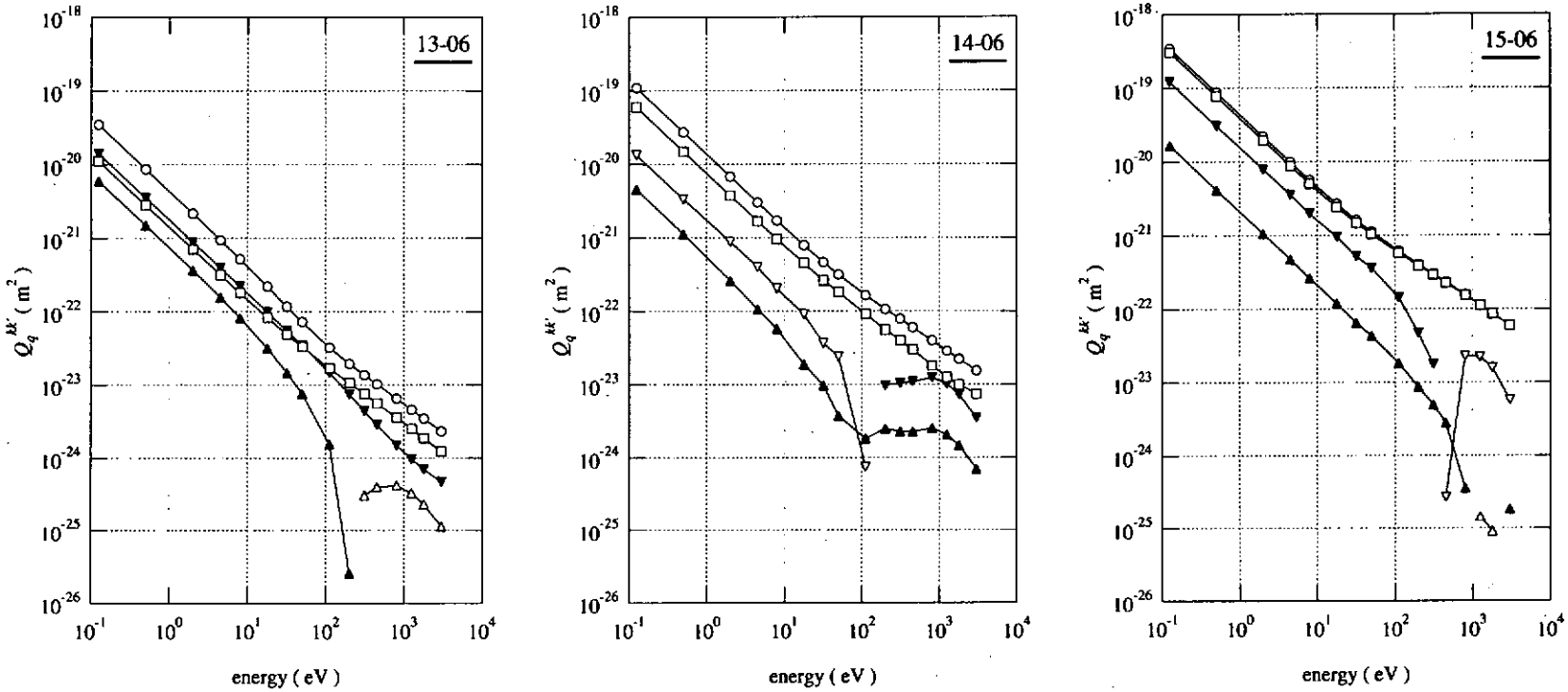

FIG. 44: Excitation cross sections from *13* to *6*, from *14* to *6* and from *14* to *6*. Q_0^{00}: open circle, Q_0^{20}: triangle, Q_0^{02}: inverted triangle and Q_0^{22}: square. The filled marks show that cross sections take negative values.

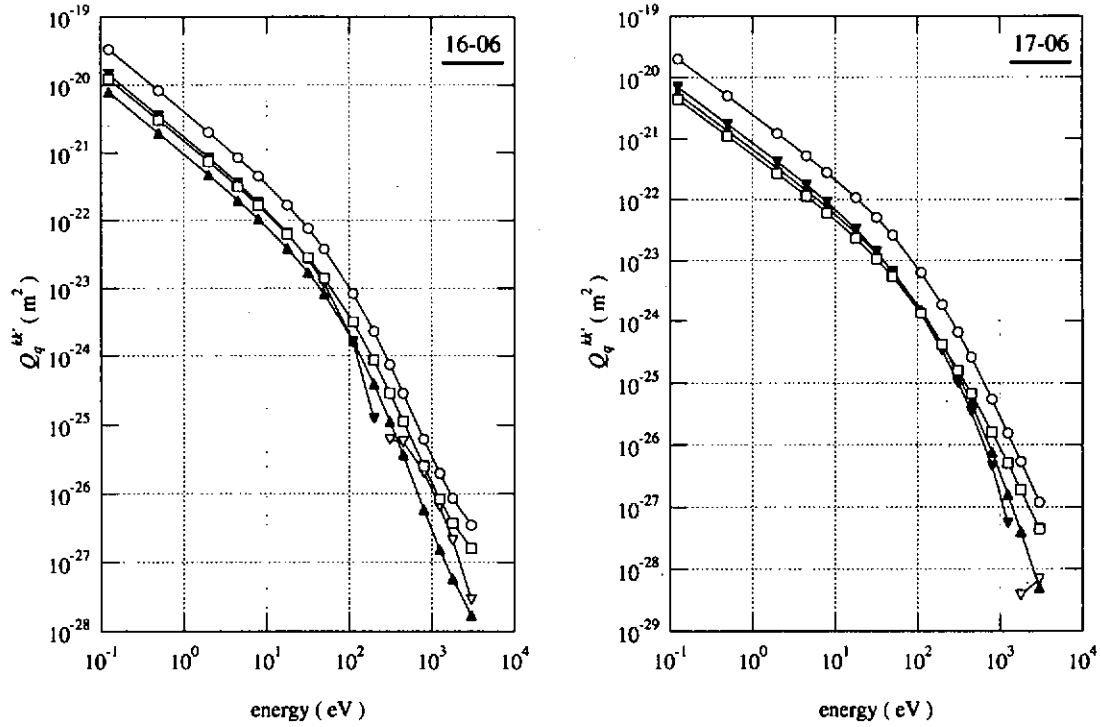

FIG. 45: Excitation cross sections from *16* to *6* and from *17* to *6*. Q_0^{00}: open circle, Q_0^{20}: triangle, Q_0^{02}: inverted triangle and Q_0^{22}: square. The filled marks show that cross sections take negative values.

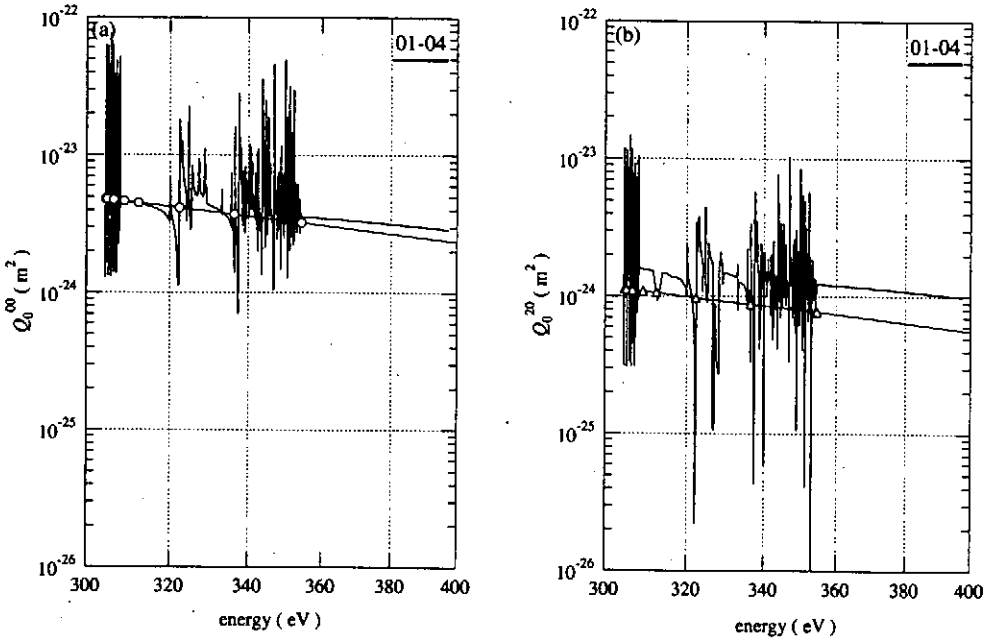

FIG. 46: Electron impact excitation cross sections with resonance structures (a) Q_0^{00} and (b) Q_0^{20} from level *1* to *4* calculated by R-matirix method plotted with lines. The cross sections plotted with circle and triangle marks are calculated by RDW approximation for comparison.

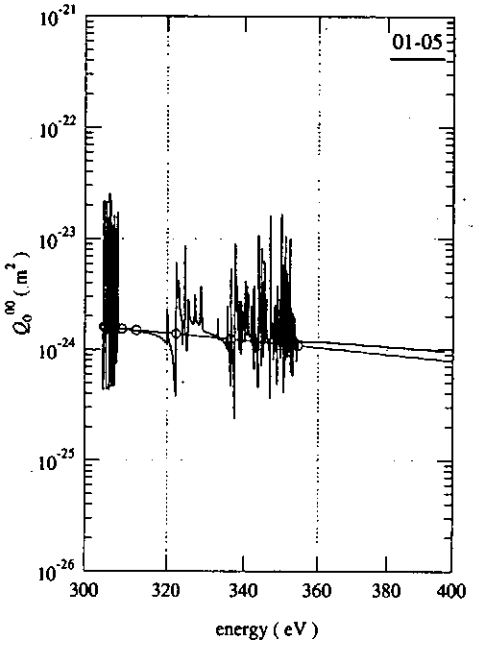

FIG. 47: Electron impact excitation cross section Q_0^{00} from *1* to *5* calculated by R-matirix method. The cross sections plotted with circle are calculated by RDW apprication for comparison.

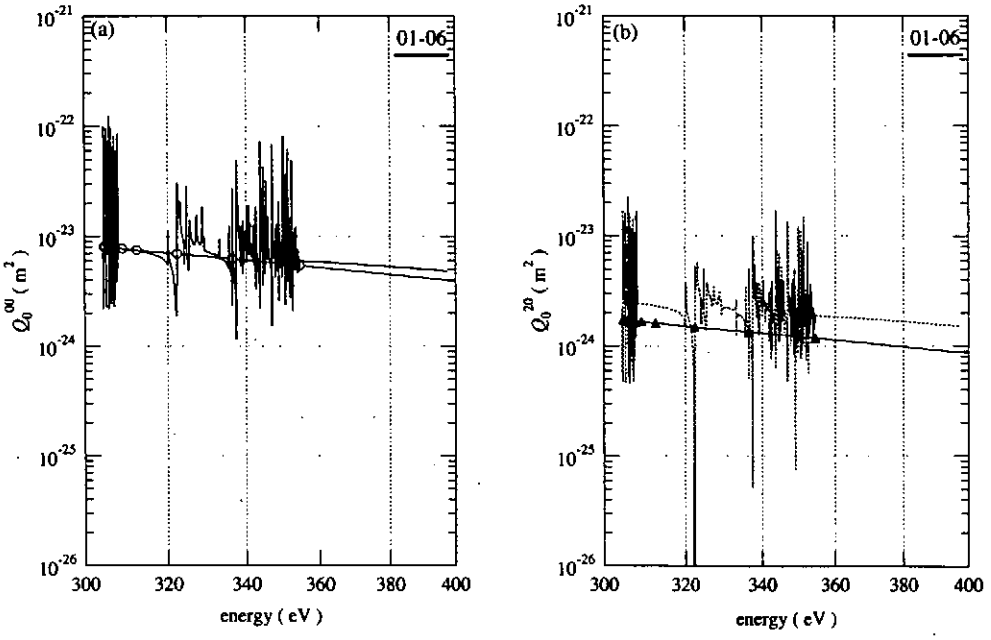

FIG. 48: Electron impact excitation cross sections (a) Q_0^{00} and (b) Q_0^{20} from *1* to *6* calculated by R-matirix method. Dotted-line shows negative values of the cross section of Q_0^{20}. The cross sections plotted with circle and triangle marks are calculated by RDW approximation for comparison.

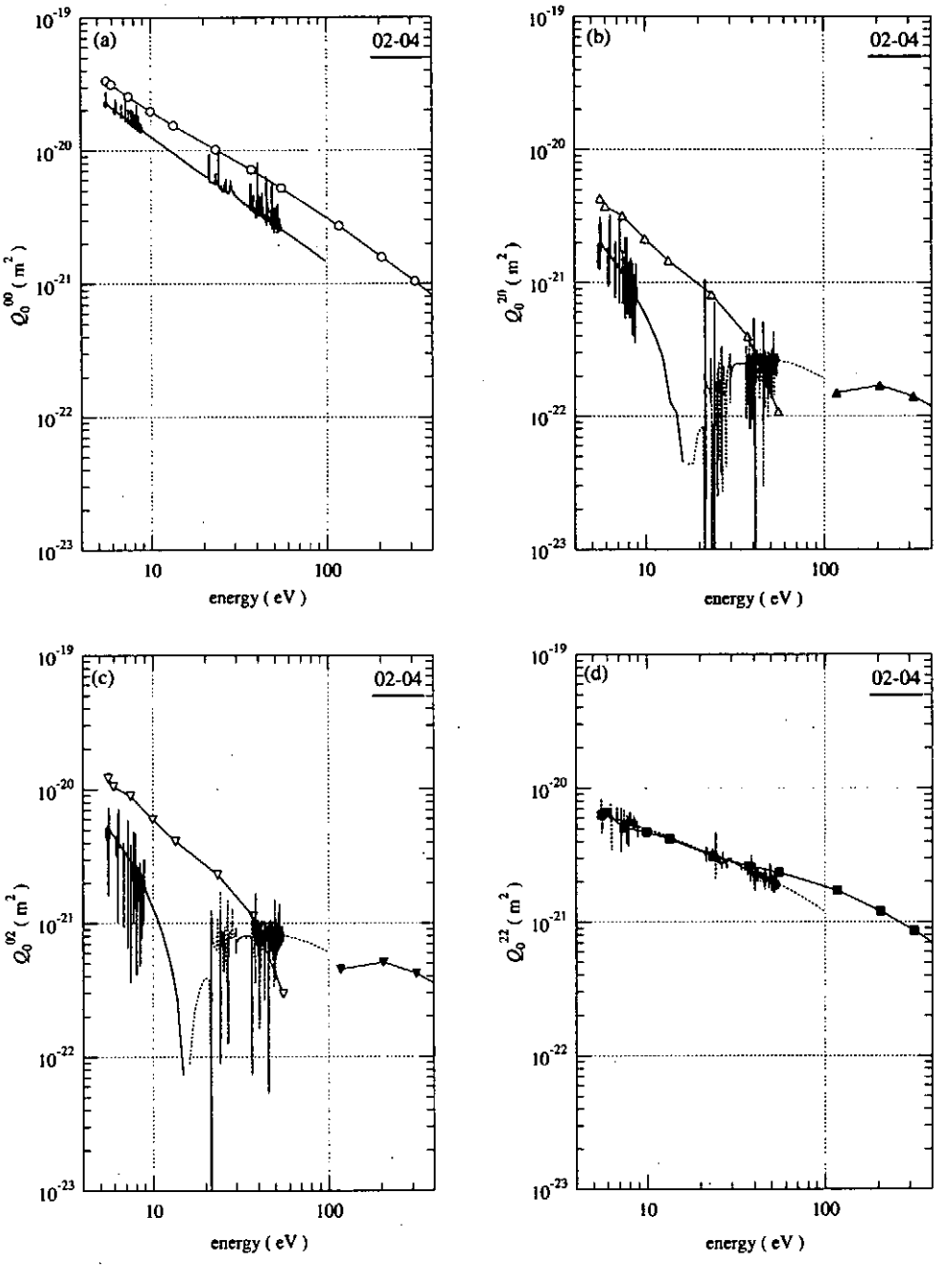

FIG. 49: Electron impact excitation cross sections (a) Q_0^{00}, (b) Q_0^{20}, (c) Q_0^{02} and (d) Q_0^{22}, from *2* to *4* calculated by R-matirix method. Dotted-line shows negative values for the cross sections of Q_0^{20}, Q_0^{02} and Q_0^{22}. The cross sections plotted with circles, triangles, inverted triangles and squares are calculated by RDW approximaiton for comparison.

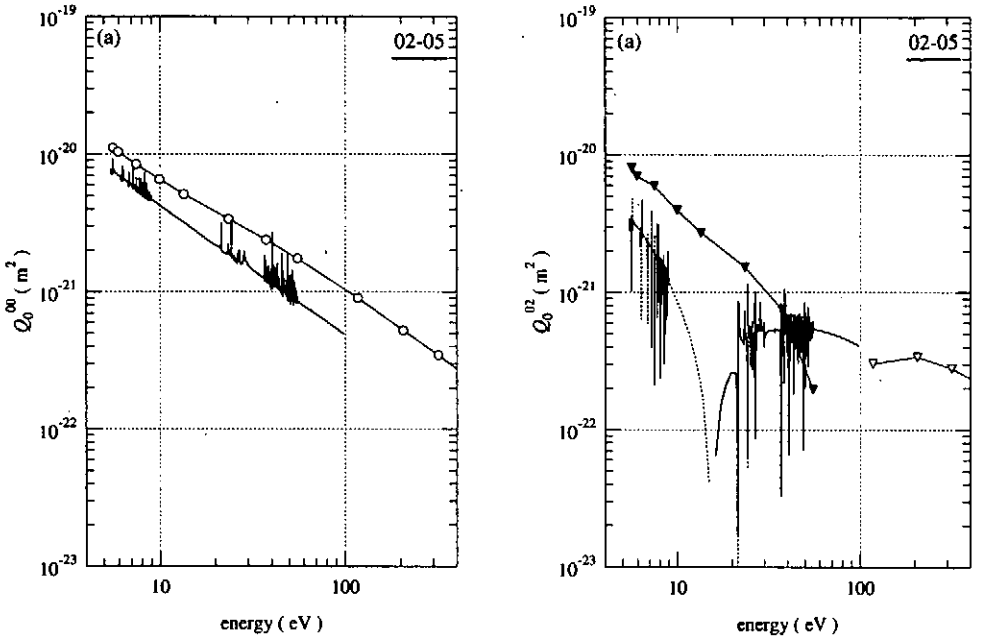

FIG. 50: Electron impact excitation cross sections (a) Q_0^{00} and (b) Q_0^{02} from *2* to *5* calculated by R-matirix method. Dotted-line shows negative values of the cross section Q_0^{02}. The cross sections plotted with circles and inverted triangles are calculated by RDW approximation for comparison.

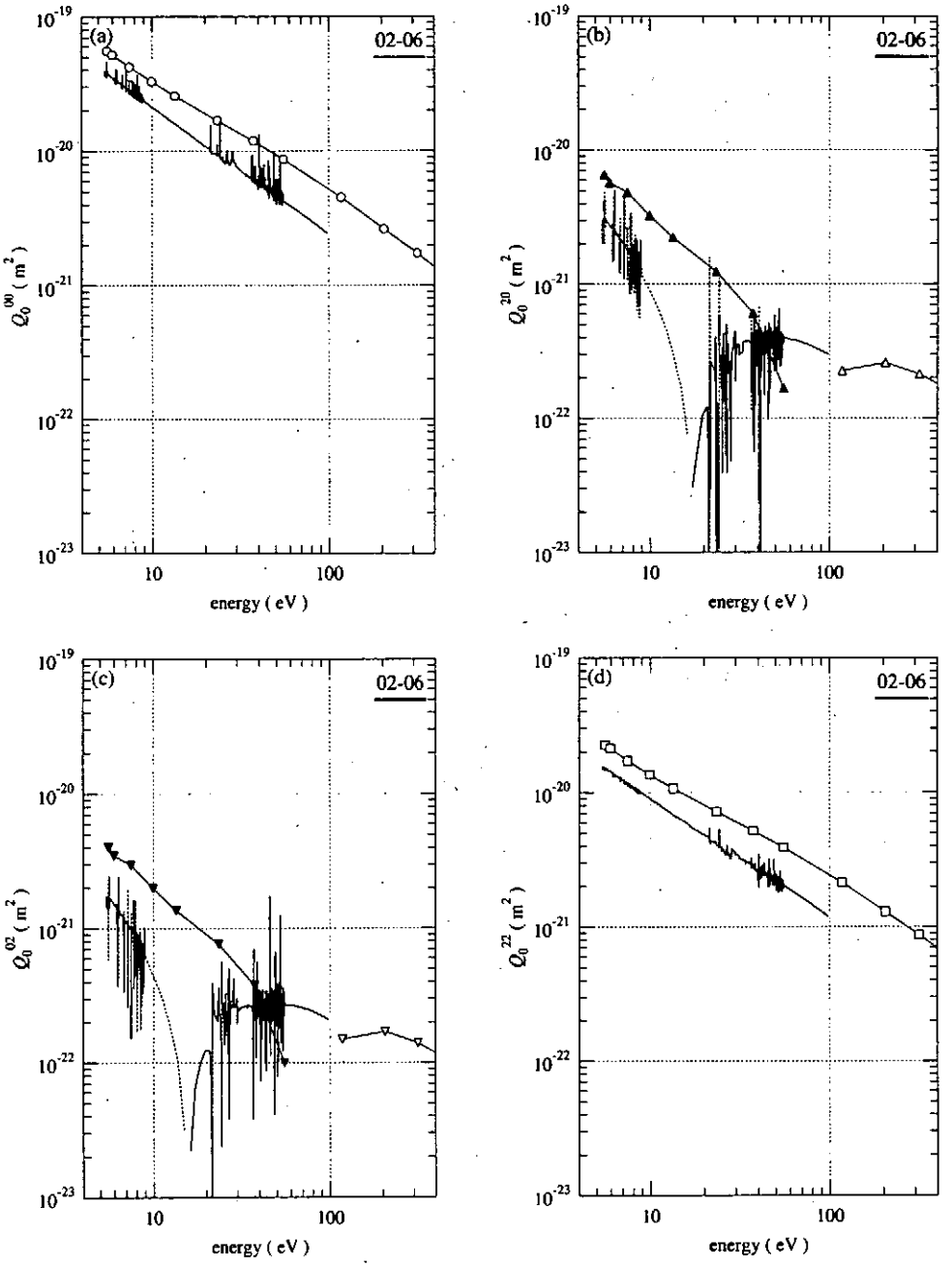

FIG. 51: Electron impact excitation cross sections (a) Q_0^{00}, (b) Q_0^{20}, (c) Q_0^{02} and (d) Q_0^{22} from *2* to *6* calculated by R-matirix method. Dotted-line shows negative values of the cross sections Q_0^{20}, Q_0^{02} and Q_0^{22}. The cross sections plotted with circles, triangles, inverted triangles and squares are calculated by RDW approximation for comparison.

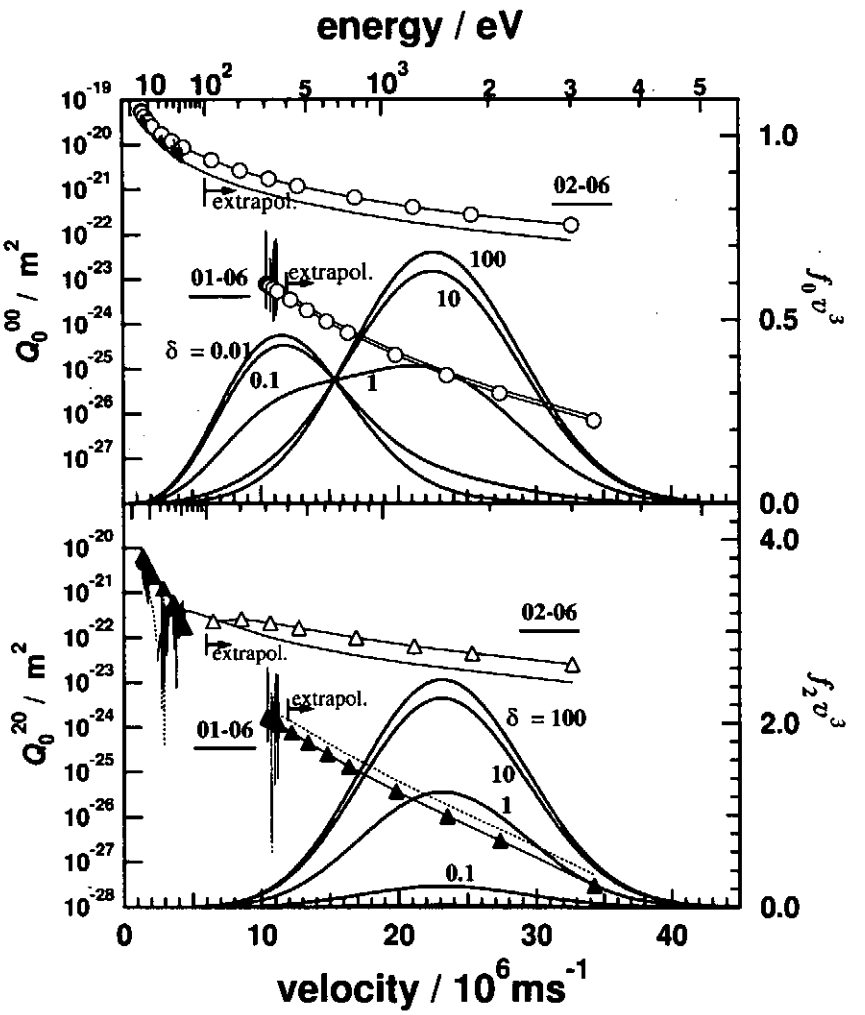

FIG. 52: Some examples of Q_0^{00} and Q_0^{20} cross sections; extrapolated R-matrix, thin curve, and RDW calculation, circles for Q_0^{00} and triangles for Q_0^{20}. For Q_0^{20} dotted curves and filled marks represent negative values. Extrapolation is performed above 400 eV for *1-4,5, 6* ; the ground state to $2^3P_{1,0,2}$ transition, and above 100 eV for*2-6*; $2^3S_1 - 2^3P_{1,0,2}$ transition. Legendre expansion coefficients of the electron velocity distributions multiplied v cubic, f_0v^3 and f_2v^3, are plotted for various δ. (see eq. (18) with the fixed parameter $V_z = 2.51 \times 10^7$m/s)

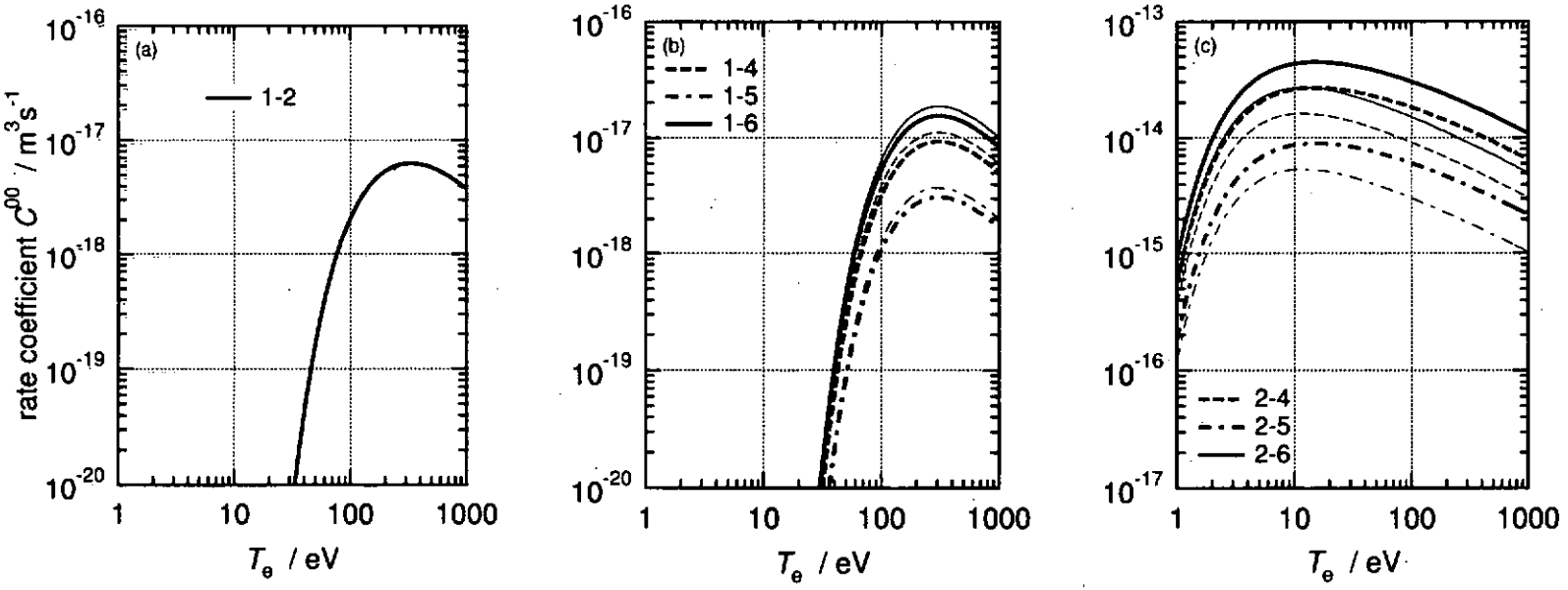

FIG. 53: Thick and thin curves represent the excitation rate coefficients $C^{00}(r,p)$ based on the RDW and R-matrix cross sections, respectively; (a) *1–2*; $1^1S_0 - 2^3S_0$, (b) *1–4,5,6*; $1^1S_0 - 2^3P_{1,0,2}$ and (c) *2–4,5,6*; $2^3S_0 - 2^3P_{1,0,2}$.

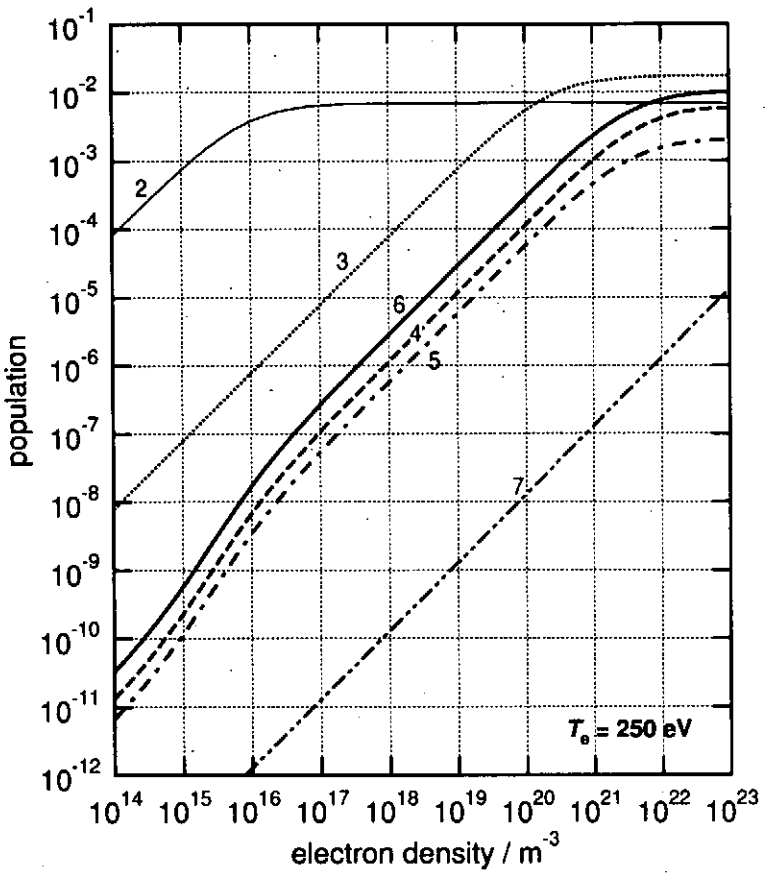

FIG. 54: The excited levels populations under the condition of $T_e = 250$ eV and $n(1^1S) = 1$ m^{-3}. *2*; 2^3S_1 thin solid line, *3*; 2^1S_0 dotted line, *4*; 2^3P_1 dashed line, *5*; 2^3P_0 dash-dotted line, *6*; 2^3P_2 thick solid line and *7*; 2^1P_0 dash-two-dotted line.

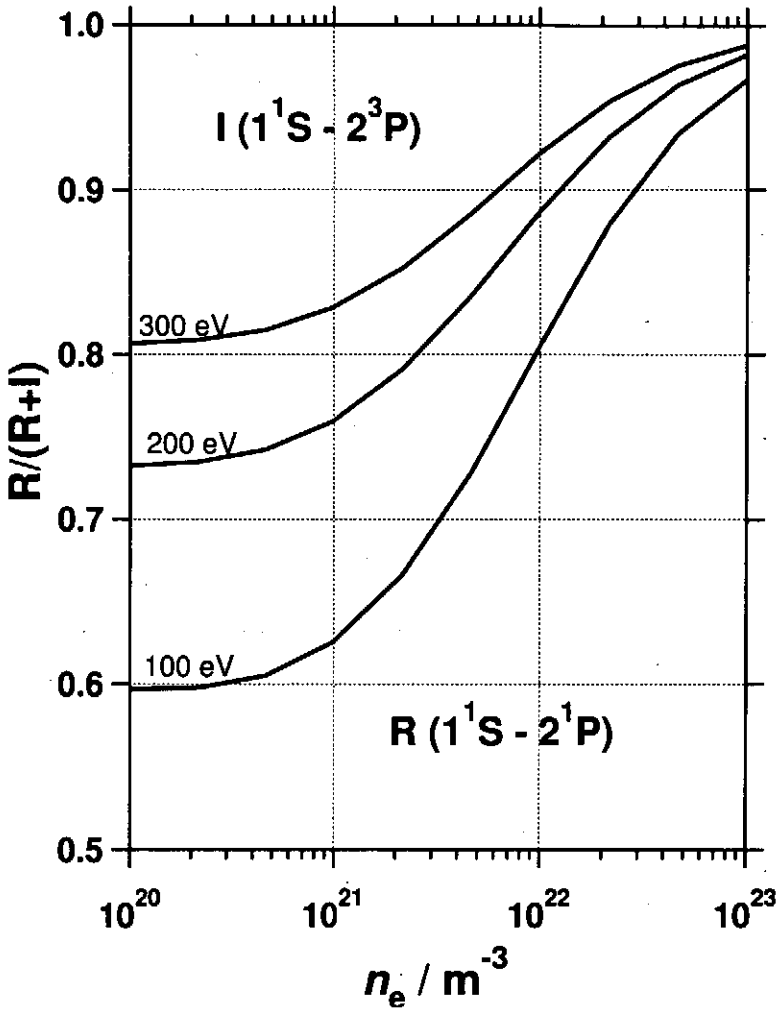

FIG. 55: The intensity ratio $R/(R+I)$ for CV.

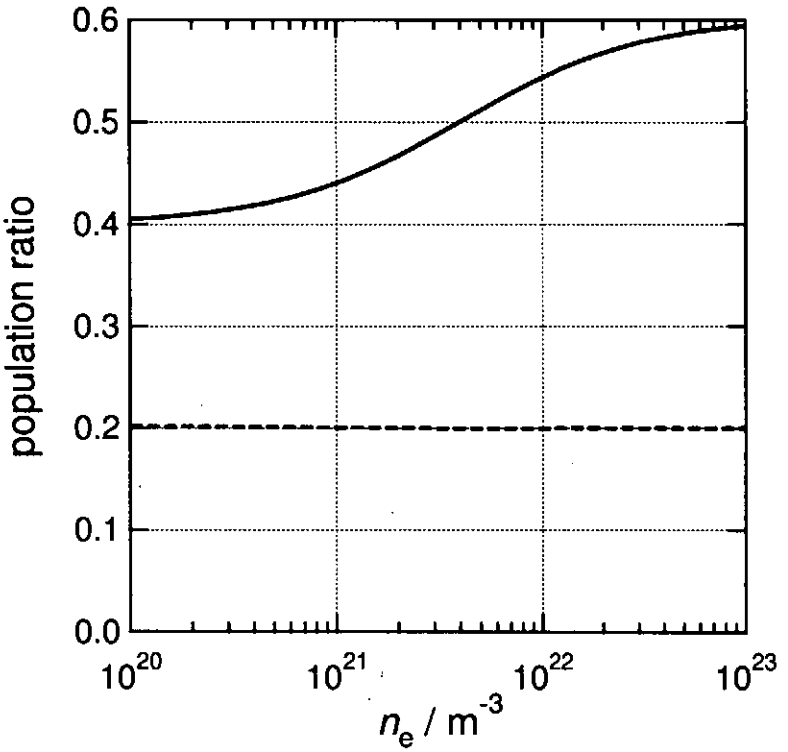

FIG. 56: The population ratio of the fine structure component of $2^3P_1/2^3P_2$ (solid line) and $2^3P_0/2^3P_2$ (dotted line) for $T_e = 200$ eV.

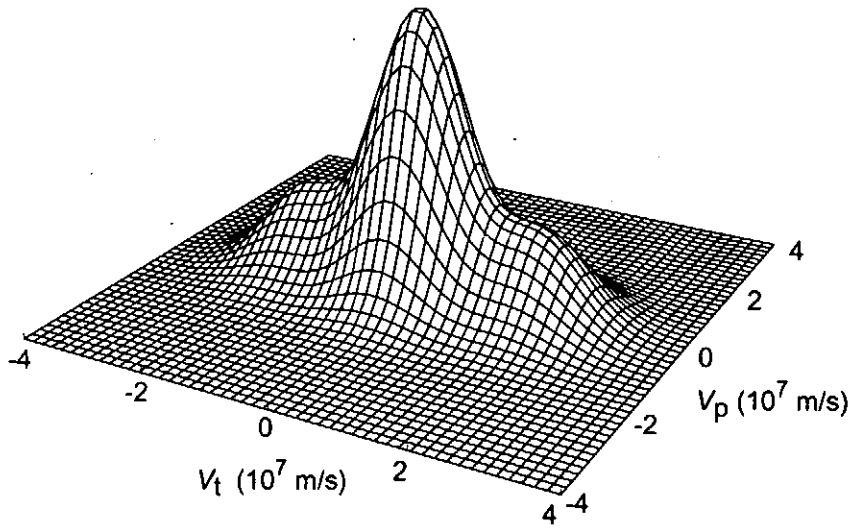

FIG. 57: Three dimensional plot of an electron velocity distribution with a thermal-bulk-with-beam distribution expressed by eq. 18. The parameters used to represent the 3D plot are $T_{\mathrm{eth}} = T_{\mathrm{eb}} = T_{\mathrm{e}}$ = 250 eV, $\delta = 0.3$ and $V_z = 1.87 \times 10^7\,\mathrm{m/s}\,(2 \times v_{\mathrm{th}}, 1000\,\mathrm{eV})$.

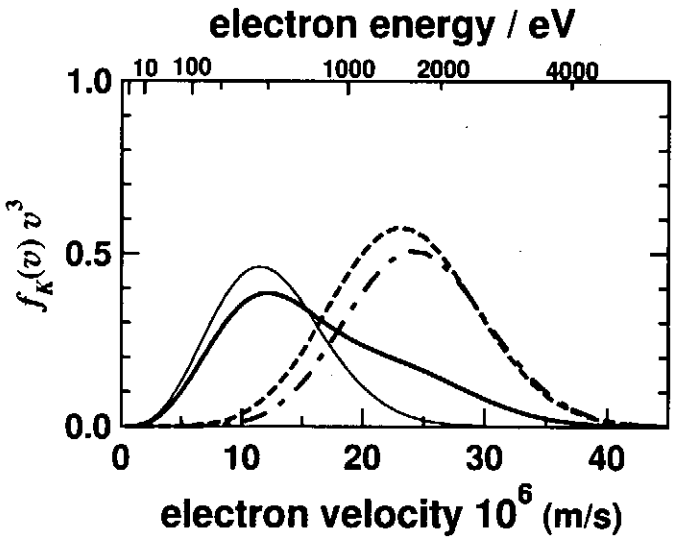

FIG. 58: The K = even moment-components $f_K(v)$ of the expansion coefficients of the velocity distribution multiplied by v^3 for the thermal-bulk-with-beam distribution shown above. Thick solid curve; $f_0(v)v^3$, dashed curve; $f_2(v)v^3$ and dash-dotted curve; $f_4(v)v^3$. The thin solid curve represents the isotropic Maxwellian distribution of electron temperature T_{e} = 250 eV

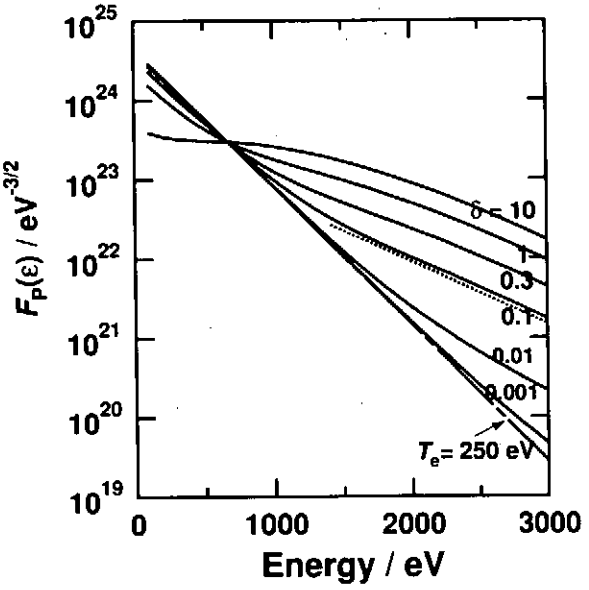

FIG. 59: The EEPF, $F_{\rm P}(\mathcal{E})$, of the thermal-bulk-with-beam Maxwellian represented by eq.(18) with the different beam-to-thermal ratio, δ, and the constant parameters; $T_{\rm eth} = T_{\rm eb}$= 250 eV and $V_z = 1.87 \times 10^7$ m/s. The dotted line shows the slope of $T_{\rm e} = 550$ eV.

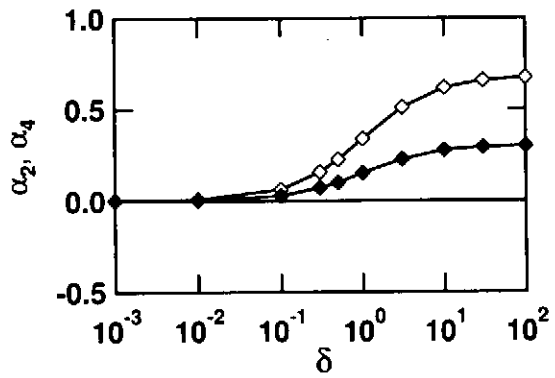

FIG. 60: The degree of anisotropy, α_K, for the thermal-bulk-with-beam Maxwellian represented by eq.(18) with the different beam-to-thermal ratio, δ, and the constant parameters; $T_{\rm eth} = T_{\rm eb}$= 250 eV and $V_z = 1.87 \times 10^7$ m/s. Open diamond; α_2 and filled diamonds; α_4

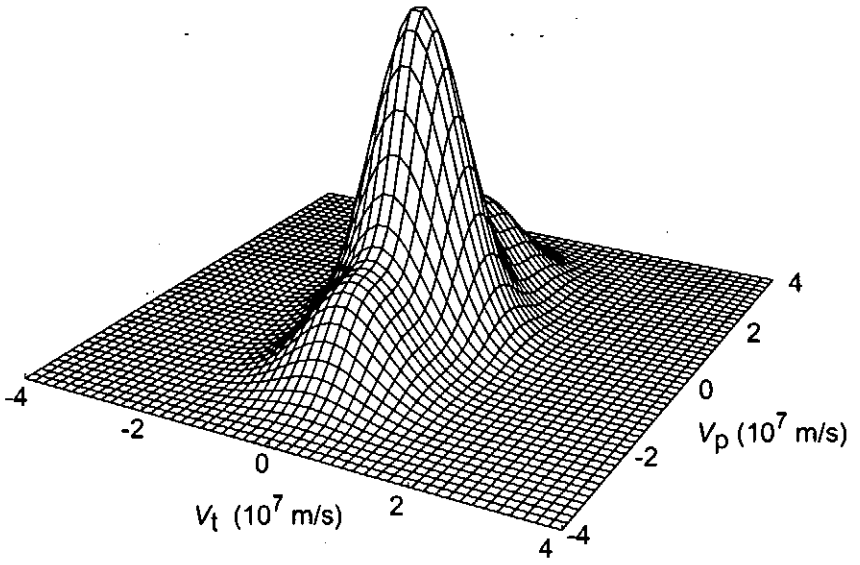

FIG. 61: Three dimensional plot of the "Saturn type" velocity distribution expressed by eq. 19. The parameters used to represent the 3D plot are $T_{eM} = T_{eR} = T_e = 250$eV, $\delta = 2$ and $V_R = 1.87 \times 10^7$m/s$(= 2 \times v_{th})$.

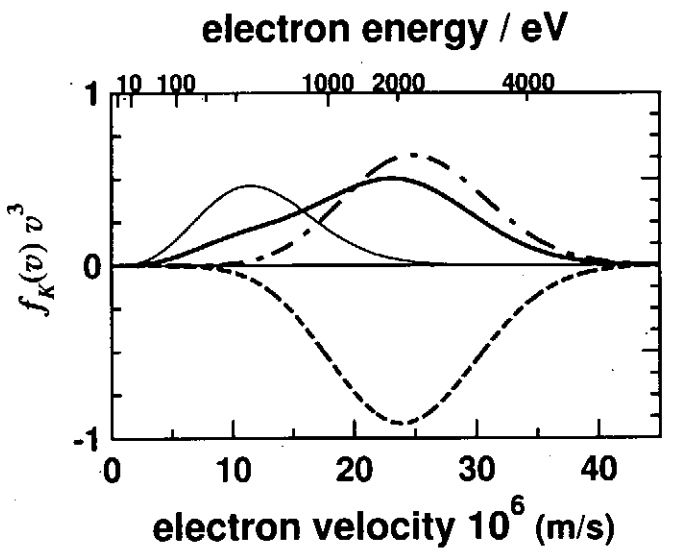

FIG. 62: K = even moment-components $f_K(v)$ of the expansion coefficients of the velocity distribution multiplied by v^3. Thick solid curve: $f_0(v)v^3$, dashed curve: $f_2(v)v^3$ and dash-dotted curve: $f_4(v)v^3$.

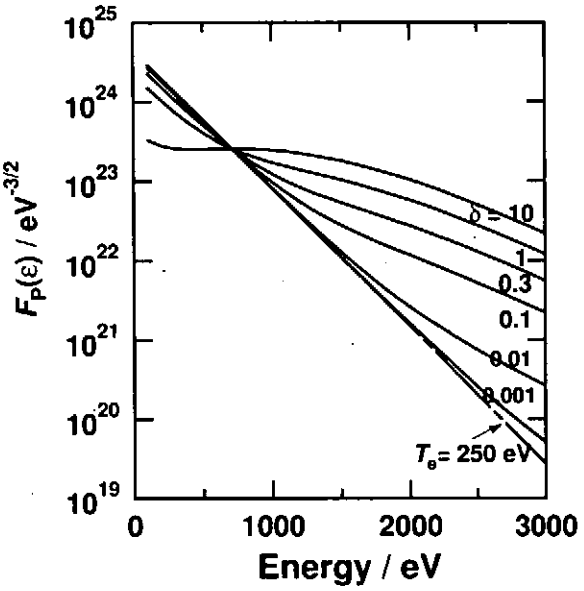

FIG. 63: The EEPF, $F_{\rm P}(\mathcal{E})$, of the Saturn-type Maxwellian represented by eq.(19) with the different ring component to thermal ratio, δ, and the constant parameters; $T_{\rm eth} = T_{\rm eb}$= 250 eV and V_z = 1.87×10^7 m/s.

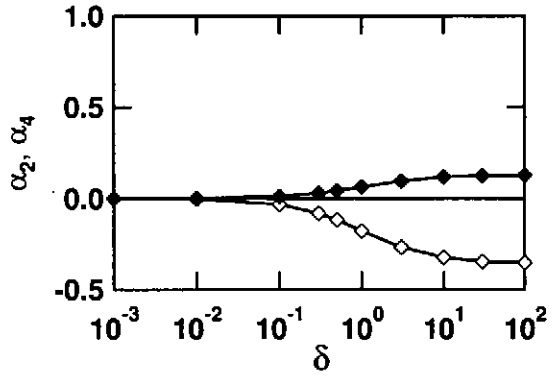

FIG. 64: The degree of anisotropy, α_K, for the Saturn-type represented by eq.(19) with the different ring component to thermal ratio, δ, and the constant parameters; $T_{\rm eth} = T_{\rm eb}$= 250 eV and V_z = 1.87×10^7 m/s. Open diamond; α_2 and filled diamonds; α_4. Thin solid curve represents isotropic Maxwellian distribution of electron temperature $T_{\rm e}$ = 250 eV.

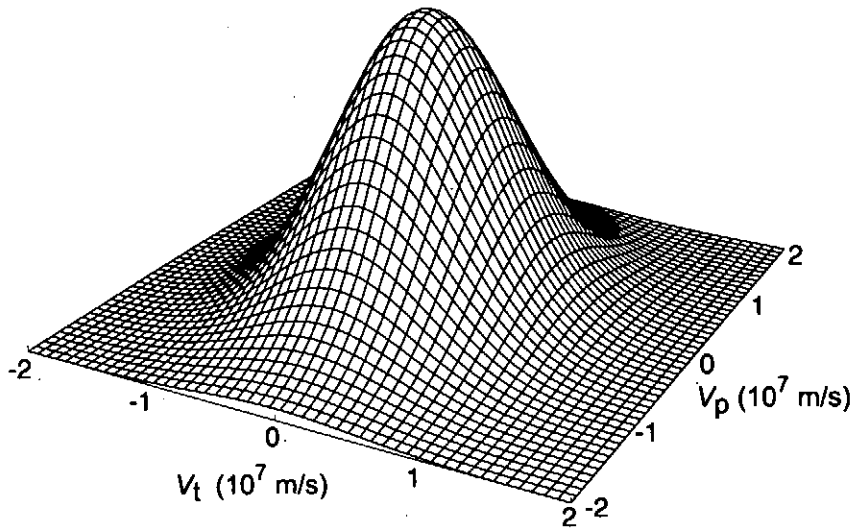

FIG. 65: Three dimensional plot of the two temperature velocity distribution expressed by eq. (21). The parameters used to represent the 3D plot are $V_z = 0$, $T_t = 200$ and $T_p = 350$eV

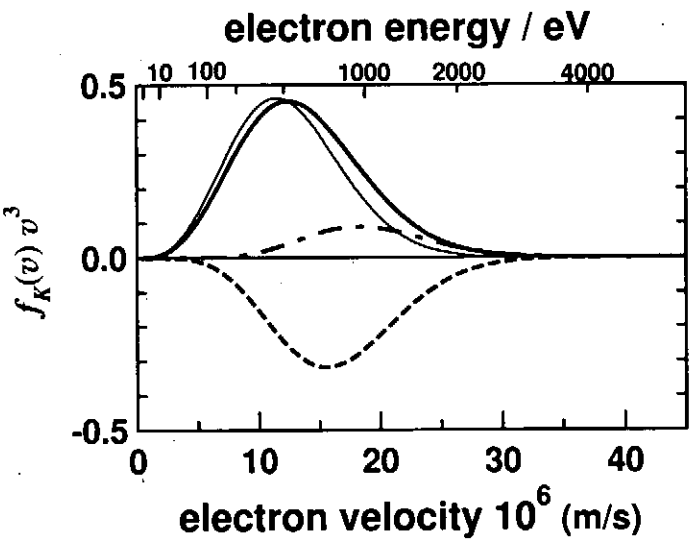

FIG. 66: The K = even moment-components $f_K(v)$ of the expansion coefficients of the velocity distribution multiplied by v^3 for the two temperature velocity distribution shown in Fig. 65. Thick solid curve; $f_0(v)v^3$, dashed curve; $f_2(v)v^3$ and dash-dotted curve; $f_4(v)v^3$. Thin solid curve represents isotropic Maxwellian distribution of electron temperature $T_e = 250$ eV

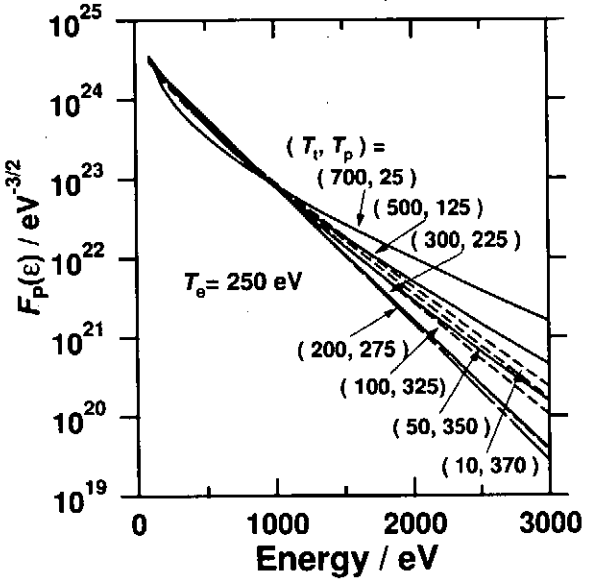

FIG. 67: The EEPF, $F_P(\mathcal{E})$, of the two temperature velocity distribution represented by eq.(21). Solid curves for the cigar-shapes; $T_t > T_p$, and dashed curve for pancake-shapes; $T_t < T_p$. The values of T_t and T_p, were selected to indicate the same mean squared value of the velocity, $\frac{1}{2}m < v^2 >= 250$ eV.

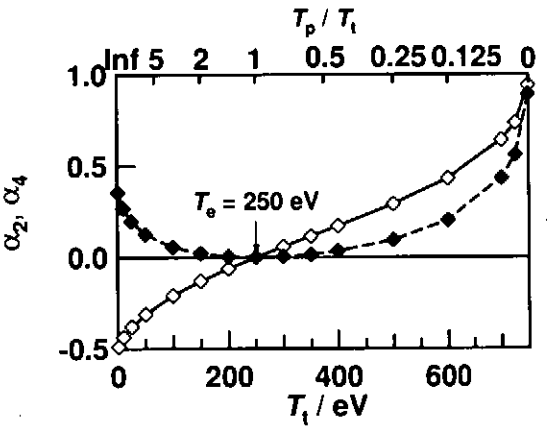

FIG. 68: The degree of anisotropy, α_K, for the two temperature EVDF represented by eq.(21). Open diamond; α_2 and filled diamonds; α_4. T_t and T_p, were selected to indicate the same mean squared value of v; $\frac{1}{2}m < v^2 >= 250$ eV

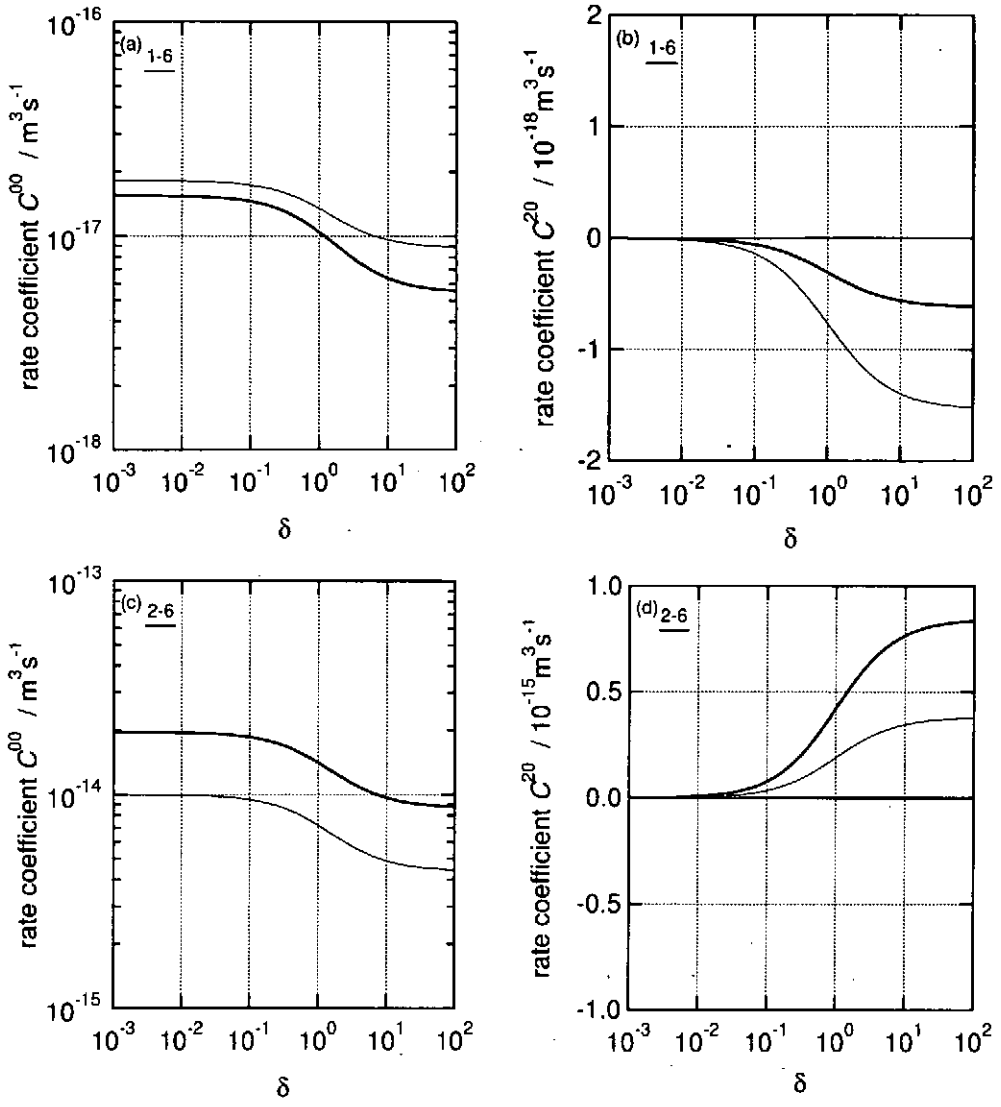

FIG. 69: Thick and thin curves represent the examples of excitation rate coefficients, C^{00} and C^{20}, based on the RDW (thick curves) and R-matrix cross sections (thin curves), respectively; plotted against δ of the bulk-with-beam type electron distribution function of fixed parameters; $T_{\rm eM} = T_{\rm eR} = T_{\rm e} = 250$eV and $V_z = 1.87 \times 10^7$m/s. (a) C^{00} $(1)1^1{\rm S}_0 - (6)2^3{\rm P}_2$, (b) C^{20} $(1)1^1{\rm S}_0 - (6)2^3{\rm P}_2$, (c) C^{00} $(2)2^3{\rm S}_1 - (6)2^3{\rm P}_2$ and (d) C^{20} $(2)2^3{\rm S}_1 - (6)2^3{\rm P}_2$,

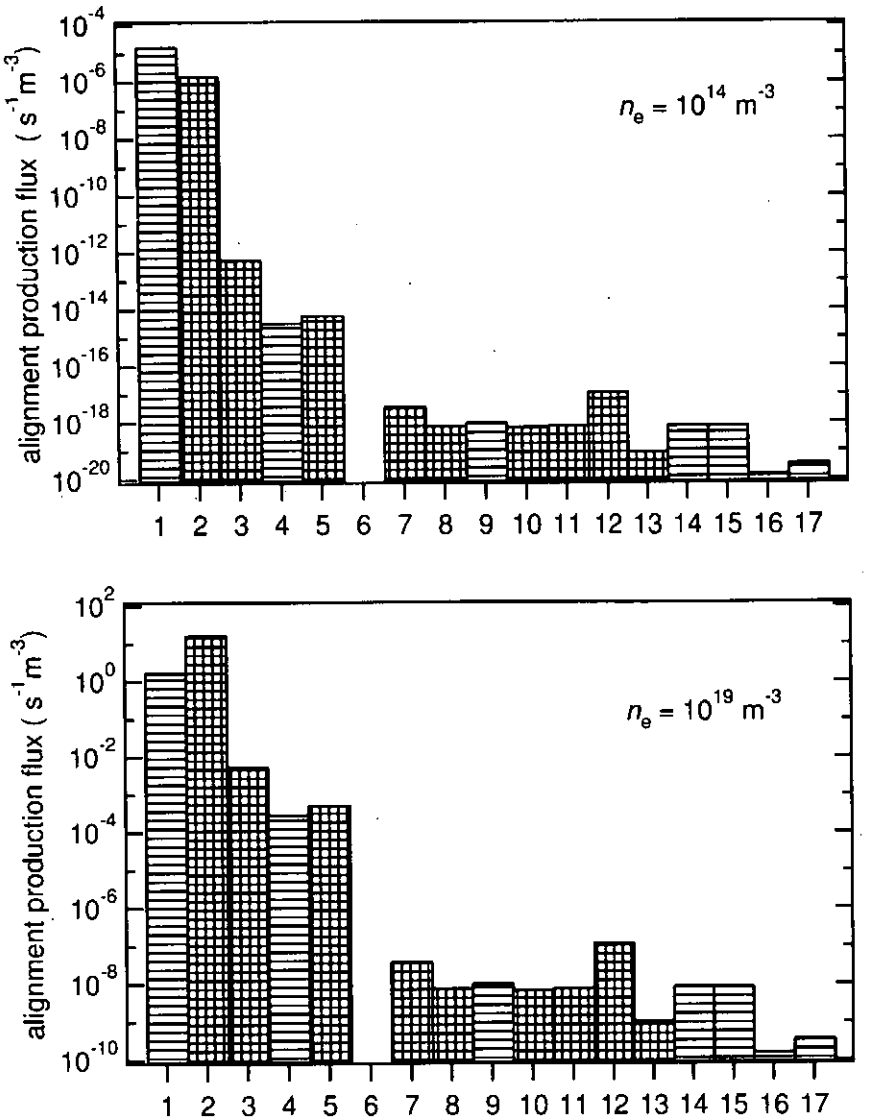

FIG. 70: Calculated alignment-production flux to level (6) from the other levels r for the thermal-bulk-with-beam velocity distribution with the parameters $\delta = 0.3$, $T_{\rm eth} = T_{\rm eb} = 250$ eV and $V_z = 1.87 \times 10^7$ m/s at $n_c = 10^{19}$ m^{-3} and $n_e = 10^{19}$ m^{-3}. The ground state density is normalized i.e, $n(1s^2\,{}^1{\rm S}_0) = 1$ m^{-3}. Positive flux; crossed hatching. Negative flux; slashed hatching.

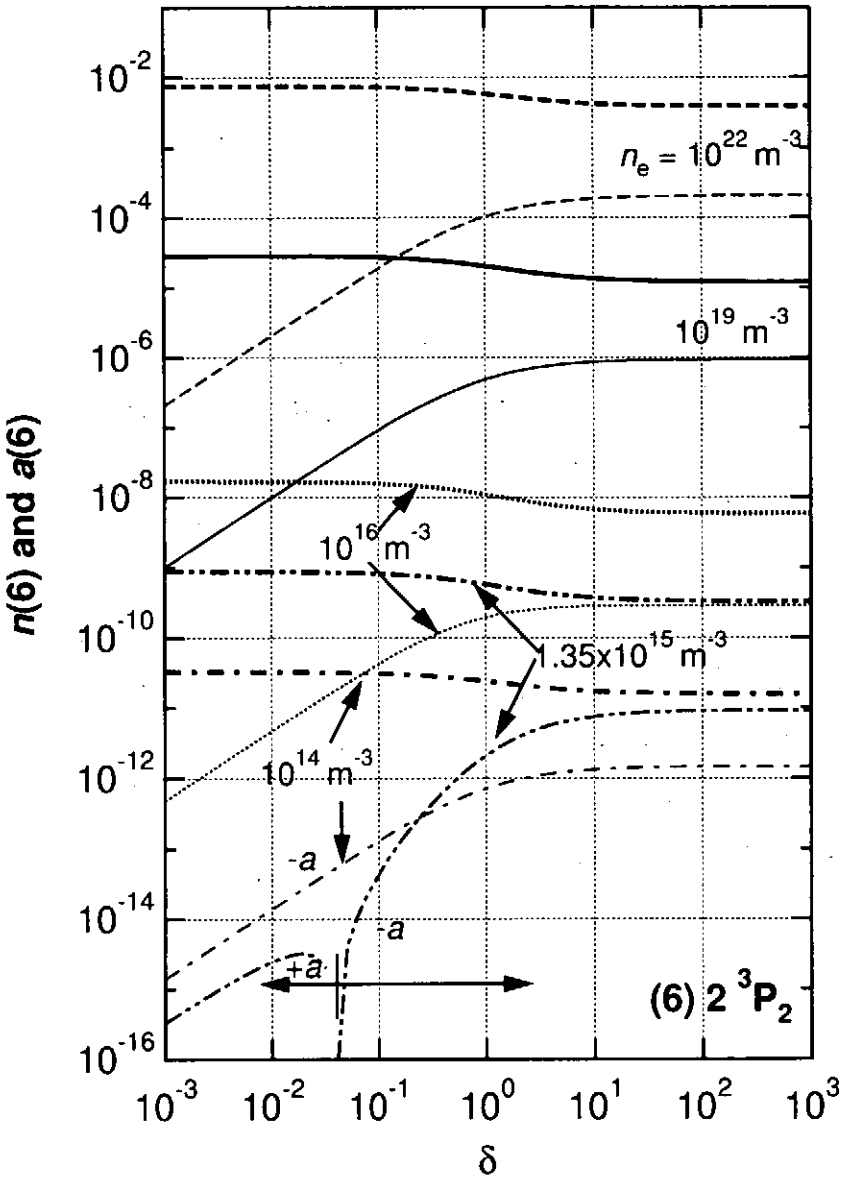

FIG. 71: The δ dependence of the population (thick curves) and alignment (thin curves) of the level (6) 2^3P_2, dashed curves for $n_e = 10^{22}$ m^{-3}, solid curves for $n_e = 10^{19}$ m^{-3}, dotted curves for $n_e = 10^{16}$ m^{-3}, double-dot-dashed curves for $n_e = 1.35 \times 10^{15}$ m^{-3}, single-dot-dashed curves for $n_e = 10^{14}$ m^{-3},

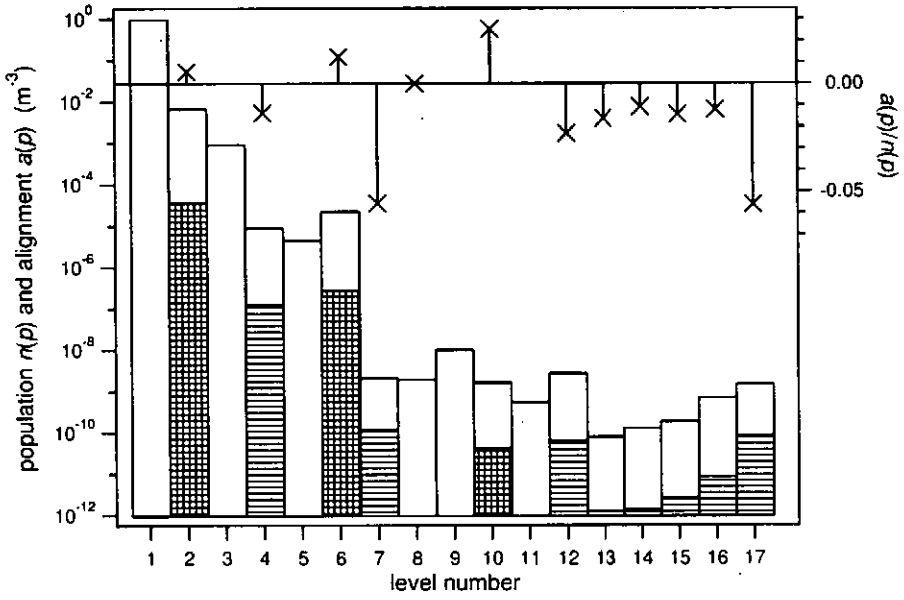

FIG. 72: Calculated population $n(p)$, alignment $a(p)$ shown with bars and their ratio $a(p)/n(p)$, crosses for the bulk-with-beam velocity distribution with the parameters $\delta = 0.3$, $T_{\rm eth} = T_{\rm eb} = 250$ eV and $V_z = 1.87 \times 10^7$ m/s for $n_{\rm e} = 10^{19}$ m^{-3} and $n(1s^2\,{}^1{\rm S}_0) = 1$ m^{-3}. The bar without filling shows the population of the levels. The crossed hatching shows the positive alignment and the slashed hatching shows the negative alignment. For the $J = 0$ levels, (1), (3), (5), (9) and (11), the alignment is undefined.

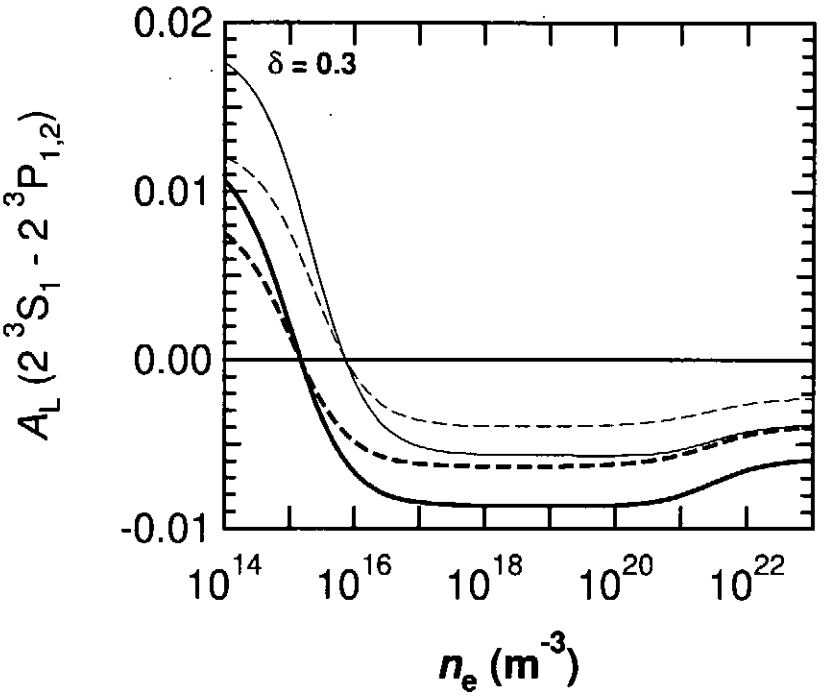

FIG. 73: The electron densities dependence of the longitudinal alignments of the emission line 2^3S_1-$2^3P_{1,2}$, thick and thin curves; RDW and R-matrix extrapolated, respectively, displayed with dashed line (J:1 $\leftarrow$ 1) and solid line (J:1 $\leftarrow$ 2). The thermal-bulk-with-beam type represented by eq. (18) with the fixed parameters $\delta = 0.3$, $T_{\rm eth} = T_{\rm eb} = 250$ eV and $V_z = 1.87 \times 10^7$ m/s.

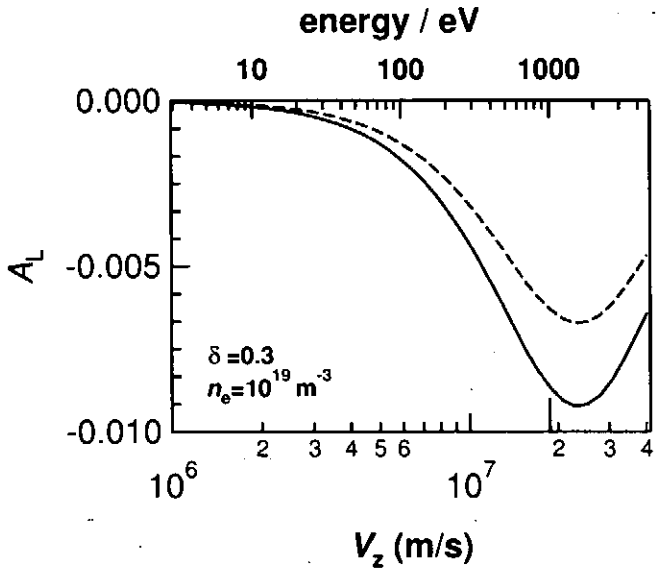

FIG. 74: The shifted velocity V_z dependence of the longitudinal alignment of the emission line 2^3S_1-$2^3P_{1,2}$ displayed with thick solid line ($J = 1 \leftarrow 2$) and thick dashed line $J = 1 \leftarrow 1$. The shifted velocity V_z dependence of the populations of $2^3P_{J=0,1,2}$ state. Thin solid line ($J = 2$), thin dashed line $J = 1$ and thin dash-dotted line $J = 0$. The bulk-with-beam type represented by eq. (18) with the fixed parameters $\delta = 0.3$, $T_{\rm eth} = T_{\rm eb} = 250$eV, $n_{\rm e} = 10^{19}$m^{-3} and $n(1^1S_0) = 1$m^{-3}.

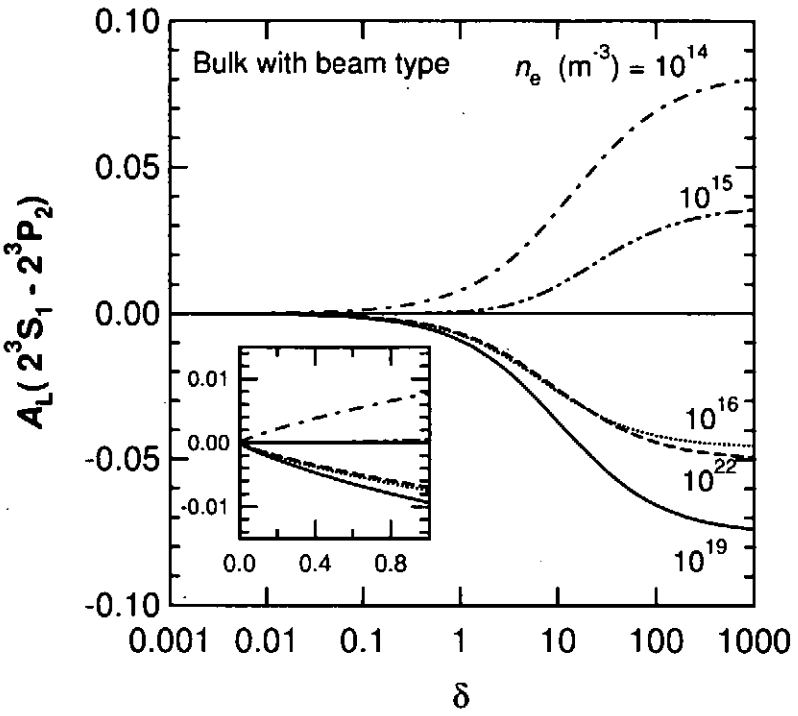

FIG. 75: For bulk with beam type EVDF, the δ dependence of the longitudinal alignment of the emission (2)-(6) 2^3S_1-2^3P_2 for different electron densities, dot-dashed curve: $n_e = 10^{14}m^{-3}$, double-dot-dashed: $n_e = 10^{15}m^{-3}$, dotted: $n_e = 10^{16}m^{-3}$, solid line is $n_e = 10^{19}m^{-3}$ and dashed: $n_e = 10^{22}m^{-3}$,

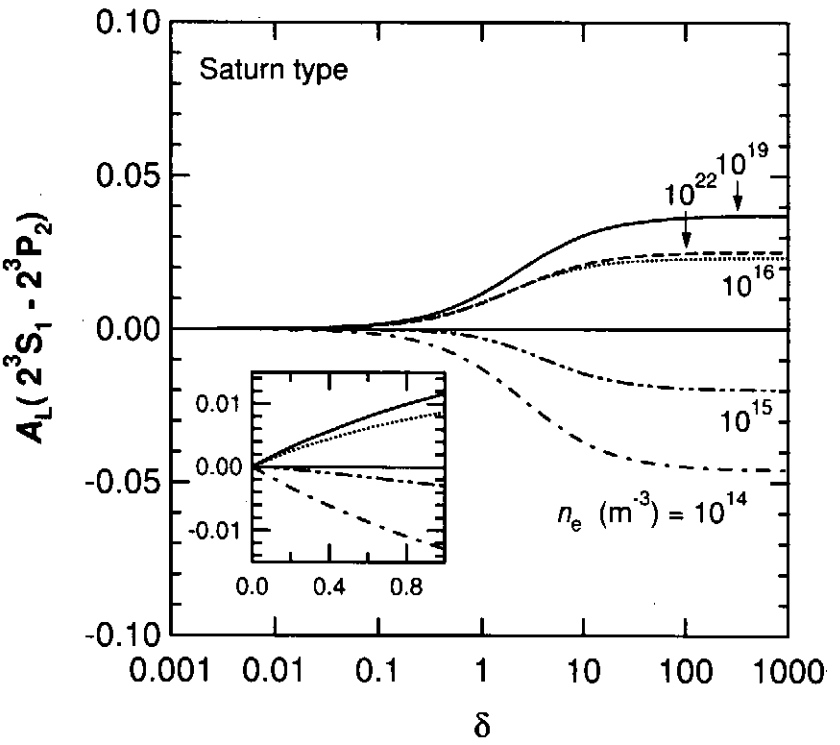

FIG. 76: For Saturn type EVDF, the δ dependence of the longitudinal alignment of the emission (2)-(6) 2^3S_1-2^3P_2 for different electron densities, dot-dashed curve: $n_e = 10^{14}\mathrm{m}^{-3}$, double-dot-dashed: $n_e = 10^{15}\mathrm{m}^{-3}$, dotted: $n_e = 10^{16}\mathrm{m}^{-3}$, solid line is $n_e = 10^{19}\mathrm{m}^{-3}$ and dashed: $n_e = 10^{22}\mathrm{m}^{-3}$,

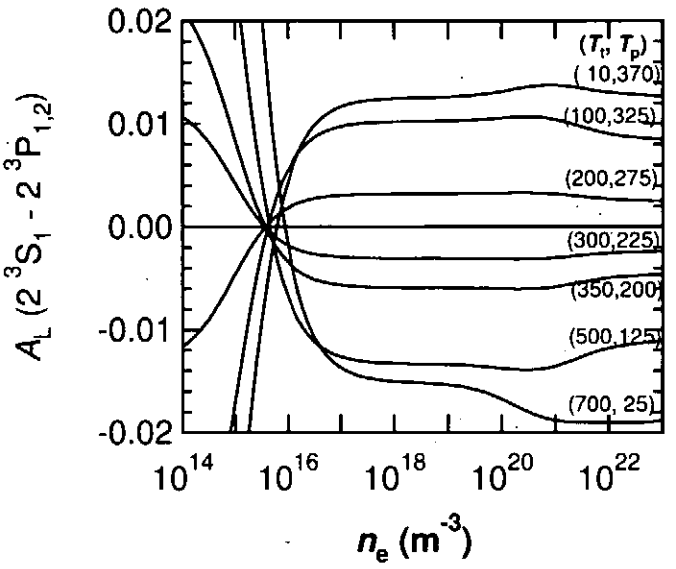

FIG. 77: Calculated longitudinal alignment, $A_{\rm L}$, for the emission (2)-(6) $2^3{\rm S}_1 \leftarrow 2^3{\rm P}_2$. Two temperature parameters EVDFs are assumed. $T_{\rm t}$ and $T_{\rm p}$, are selected to indicate the same mean squared value of v; $\frac{1}{2}m<v^2>=250$ eV.

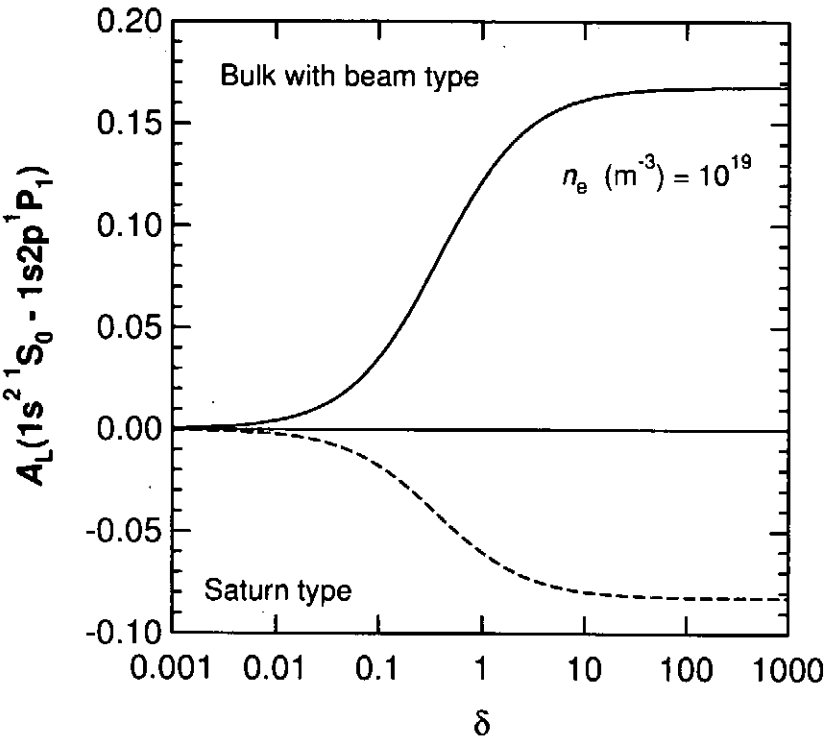

FIG. 78: Calculated longitudinal alignment, $A_{\rm L}$, for the emission (1)-(7) $1s^2\,{}^1{\rm S}_0 \leftarrow 1s2p\,{}^1{\rm P}_1$. Bulk with beam type and Saturn type EVDFs are assumed. $T_{\rm eth}$, $T_{\rm eb,er}$ and $V_{z,r}$ are fixed at 250 eV and 1.87×10^7m/s, respectively. The ratio δ is parameterized. The $A_{\rm L}(1s^2\,{}^1{\rm S}_0 \leftarrow 1s2p\,{}^1{\rm P}_1)$ is independent on the electron densities.

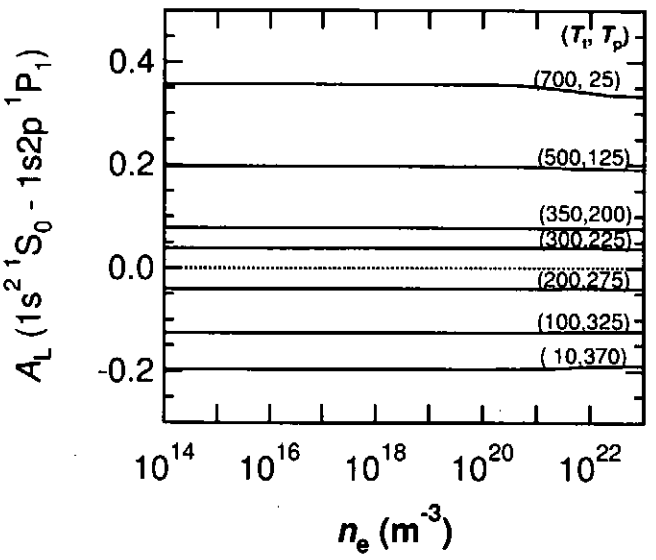

FIG. 79: Calculated longitudinal alignment, $A_{\rm L}$, for the emission (1)-(7) $1s^2\,{}^1{\rm S}_0 \leftarrow 1s2p\,{}^1{\rm P}_1$. Two temperature parameters EVDFs are assumed. $T_{\rm t}$ and $T_{\rm p}$, are selected to indicate the same mean squared value of v; $\frac{1}{2}m<v^2>=250$ eV.

Recent Issues of NIFS-DATA Series

NIFS-DATA-53 J.G. Wang, T. Kato and I. Murakami,
Dielectronic Recombination Rate Coefficients to Excited States of He from He^{+}: Apr. 1999

NIFS-DATA-54 T. Kato and E. Asano,
Comparison of Recombination Rate Coefficients Given by Empirical Formulas for Ions from Hydrogen through Nickel: June 1999

NIFS-DATA-55 H.P. Summers, H. Anderson, T. Kato and S. Murakami,
Hydrogen Beam Stopping and Beam Emission Data for LHD: Nov. 1999

NIFS-DATA-56 S. Born, N. Matsunami and H. Tawara,
A Simple Theoretical Approach to Determine Relative Ion Yield (RIY) in Glow Discharge Mass Spectrometry (GDMS): Jan. 2000

NIFS-DATA-57 T. Ono, T. Kawamura, T. Kenmotsu, Y. Yamamura,
Simulation Study on Retention and Reflection from Tungsten Carbide under High Fluence of Helium Ions: Aug. 2000

NIFS-DATA-58 J.G. Wang, M. Kato and T. Kato,
Spectra of Neutral Carbon for Plasma Diagnostics: Oct. 2000

NIFS-DATA-59 Yu. V. Ralchenko, R. K. Janev, T. Kato, D.V. Fursa, I. Bray and F.J. de Heer
Cross Section Database for Collision Processes of Helium Atom with Charged Particles.
I. Electron Impact Processes: Oct. 2000

NIFS-DATA-60 U.I. Safronova, C. Namba, W.R. Johnson, M.S. Safronova,
Relativistic Many-Body Calculations of Energies for n = 3 States in Aluminiumlike Ions: Jan. 2001

NIFS-DATA-61 U.I. Safronova, C. Namba, I. Murakami, W.R. Johnson and M.S. Safronova,
E1,E2, M1, and M2 Transitions in the Neon Isoelectronic Sequence: Jan. 2001

NIFS-DATA-62 R. K. Janev, Yu.V. Ralchenko, T. Kenmotsu,
Unified Analytic Formula for Physical Sputtering Yield at Normal Ion Incidence: Apr. 2001

NIFS-DATA-63 Y. Itikawa,
Bibliography on Electron Collisions with Molecules: Rotational and Vibrational Excitations, 1980-2000 Apr. 2001

NIFS-DATA-64 R.K. Janev, J.G. Wang and T.Kato,
Cross Sections and Rate Coefficients for Charge Exchange Reactions of Protons with Hydrocarbon Molecules: May 2001

NIFS-DATA-65 T. Kenmotsu, Y. Yamamura, T. Ono and T. Kawamura,
A New Formula of the Energy Spectrum of Sputtered Atoms from a Target Material Bombarded with Light Ions at Normal Incidence: May 2001

NIFS-DATA-66 I. Murakami, U. I. Safronova and T. Kato,
Dielectronic Recombination Rate Coefficients to Excited States of Be-like Oxygen: May 2001

NIFS-DATA-67 N. Matsunami, E. Hatanaka, J. Kondoh, H. Hosaka, K. Tsumori, H. Sakaue and H. Tawara,
Secondary Charged Particle Emission from Proton Conductive Oxides by Ion Impact: July 2001

NIFS-DATA-68 R.K. Janev, J.G. Wang, I. Murakami and T. Kato,
Cross Sections and Rate Coefficients for Electron-Impact Ionization of Hydrocarbon Molecules: Oct. 2001

NIFS-DATA-69 S. Zou, T. Kato, I. Murakami,
Charge Exchange Recombination Spectroscopy of Li III Ions for Fusion Plasma Diagnostics: Oct. 2001

NIFS-DATA-70 I. Murakami, T. Kato, A. Igarashi, M. Imai, Y. Itikawa, D. Kato, M. Kimura, T. Kusakabe, K. Moribayashi, T. Morishita, K. Motohashi, L. Pichl
AMDIS and CHART update (I): Oct. 2002

NIFS-DATA-71 S. Zou, L. Pichl, M. Kimura and T. Kato
Total, Partial and Differential Ionization Cross Sections in Proton-hydrogen Collisions at Low Energy: Jan. 2003

NIFS-DATA-72 M. Hayashi
Bibliography of Electron and Photon Cross Sections with Atoms and Molecules Published in the 20th Century – Argon –: Jan. 2003

NIFS-DATA-73 J. Horacek, K. Houfek, M. Cizek, I. Murakami and T. Kato
Rate Coefficients for Low-Energy Electron Dissociative Attachment to Molecular Hydrogen: Feb. 2003

NIFS-DATA-74 M. Hayashi
Bibliography of Electron and Photon Cross Sections with Atoms and Molecules Published in the 20th Century – Carbon Dioxide –: Apr. 2003

NIFS-DATA-75 X. Ma, H.P. Liu, Z.H. Yang, Y.D. Wang, X.M. Chen, Z.Y. Liu, I. Murakami and C. Namba
Cross-section Data Measured at Low Impact Energies for Ar^{q+} Ions on Argon and Neon Targets. Apr. 2003

NIFS-DATA-76 M. Hayashi
Bibliography of Electron and Photon Cross Sections with Atoms and Molecules Published in the 20th Century – Sulphur Hexafluoride –: May 2003

NIFS-DATA-77 M. Hayashi
Bibliography of Electron and Photon Cross Sections with Atoms and Molecules Published in the 20th Century – Nitrogen Molecule – : June 2003

NIFS-DATA-78 A. Iwamae, T. Fujimoto, H. Zhang, D. P. Kilcrease, G. Csanak and K.A. Berrington
Population Alignment Collisional Radiative Model for Helium-like Carbon:Polarization of Emission Lines and Anisotropy of the Electron Velocity Distribution Function in Plasmas: Aug. 2003